Dipartimento di Informatica, Bioingegneria,
Robotica ed Ingegneria dei Sistemi

---

# Intraoperative Navigation Systems for Image-Guided Surgery

by

Andrea Schiappacasse

Theses Series **DIBRIS-TH-2018-XXX**

---

DIBRIS, Università di Genova
Via Opera Pia, 13 16145 Genova, Italy http://www.dibris.unige.it/

**Università degli Studi di Genova**

**Dipartimento di Informatica, Bioingegneria,**

**Robotica ed Ingegneria dei Sistemi**

**Ph.D. Thesis in Computer Science and Systems Engineering**
**Computer Science Curriculum**

# Intraoperative Navigation Systems for Image-Guided Surgery

by

Andrea Schiappacasse

May, 2018

**Dottorato di Ricerca in Informatica ed Ingegneria dei Sistemi**
**Indirizzo Informatica**
**Dipartimento di Informatica, Bioingegneria, Robotica ed Ingegneria dei Sistemi**
**Università degli Studi di Genova**

DIBRIS, Univ. di Genova
Via Opera Pia, 13
I-16145 Genova, Italy
http://www.dibris.unige.it/

**Ph.D. Thesis in Computer Science and Systems Engineering**
**Computer Science Curriculum**
(S.S.D. INF/01)

Submitted by Andrea Schiappacasse
DIBRIS, Univ. di Genova
andrea.schiappacasse.ge@gmail.com

Date of submission: May 2018

Title: Intraoperative Navigation Systems for Image-Guided Surgery

Advisor: Alessandro Verri
Dipartimento di Informatica, Bioingegneria, Robotica ed Ingegneria dei Sistemi
Università di Genova
alessandro.verri@unige.it

## Abstract

Recent technological advancements in medical imaging equipment have resulted in a dramatic improvement of image accuracy, now capable of providing useful information previously not available to clinicians. In the surgical context, intraoperative imaging provides a crucial value for the success of the operation.

Many nontrivial scientific and technical problems need to be addressed in order to efficiently exploit the different information sources nowadays available in advanced operating rooms. In particular, it is necessary to provide: (i) accurate tracking of surgical instruments, (ii) real-time matching of images from different modalities, and (iii) reliable guidance toward the surgical target. Satisfying all of these requisites is needed to realize effective intraoperative navigation systems for image-guided surgery.

Various solutions have been proposed and successfully tested in the field of image navigation systems in the last ten years; nevertheless several problems still arise in most of the applications regarding precision, usability and capabilities of the existing systems. Identifying and solving these issues represents an urgent scientific challenge.

This thesis investigates the current state of the art in the field of intraoperative navigation systems, focusing in particular on the challenges related to efficient and effective usage of ultrasound imaging during surgery.

The main contribution of this thesis to the state of the art are related to:

- Techniques for automatic motion compensation and therapy monitoring applied to a novel ultrasound-guided surgical robotic platform in the context of abdominal tumor thermoablation.
- Novel image-fusion based navigation systems for ultrasound-guided neurosurgery in the context of brain tumor resection, highlighting their applicability as off-line surgical training instruments.

The proposed systems, which were designed and developed in the framework of two international research projects, have been tested in real or simulated surgical scenarios, showing promising results toward their application in clinical practice.

# Acknowledgements

I want to thank Prof. Verri, Prof. Barla and the whole Slipguru group within the University of Genoa for their support, encouragement and suggestions during the development of this work.

I am grateful to Prof. Menciassi, Dr. Diodato, Dr. Cafarelli, Dr. Tognarelli, the whole team of The Biorobotics Institute at Scuola Superiore Sant'Anna and all the other members of the FUTURA project consortium for their invaluable collaboration in the development of the work described in Chapter 3.

I would also like to express my gratitude to Prof. DiMeco, Dr. Perin, Dr. Prada, Dr. Mattei, the whole team of Fondazione IRCCS Istituto Neurologico Carlo Besta, Eng. De Beni from ESAOTE S.p.A. and all the other members of the TheraGlio project consortium for their fundamental contribution in obtaining the results described in Chapter 4.

Special thanks to Dr. Santoro, Dr. Basso, Dr. Mosci, Dr. Esposito, Dr. Moraldo and the whole team of Camelot Biomedical Systems S.r.l. for giving me the opportunity to pursue my research goals during the last four years.

Part of the research leading to the results described in this work has received funding from the European Union's Seventh Framework Programme (FP7/2007–2013) under Grant Agreement 611963 (FUTURA Project) and Grant Agreement 602923 (TheraGlio Project).

# Contents

# List of Figures

# List of Abbreviations

| | |
|---|---|
| AHRS | Attitude and Heading Reference System 72 |
| API | Application Programming Interface 35, 37, 72, 83, 90, 101 |
| BM | Block Matching 87 |
| CBCT | Cone Beam Computed Tomography 13 |
| CC | Cross-correlation Coefficient 22 |
| CEUS | Contrast Enahnced Ultrasound 63, 78 |
| CT | Computed Tomography 3, 4, 7, 9–13, 21–23, 61, 64 |
| ELAS | Efficient Large Scale Stereo 88, 98 |
| EM | Electromagnetic 19, 81, 90–95, 98 |
| EMTS | Electromagnetic Tracking Systems 19–21, 67, 68, 71, 76, 81, 90, 92–94, 98, 100, 101, 103, 104 |
| EUS | Endoscopic Ultrasound 18 |
| FLANN | Fast Library for Approximate Nearest Neighbors 75 |
| FUTURA | Focused Ultrasound Therapy Using Robotic Approaches 3, 32–34, 42, 45, 47, 49, 58 |
| GP | Gaussian Process 50 |
| GT | Ground Truth 98, 99 |
| HIFU | High Intensity Focused Ultrasound 3, 5, 18, 26–34, 37–45, 50–58, 106 |
| HMI | Human Machine Interface 34, 47 |
| ICP | Iterative Closest Point 98 |
| iCT | Interventional Computed Tomography 12, 13, 62, 63 |

| | |
|---|---|
| IGS | Image-Guided Surgery 2, 5–8, 10, 11, 17, 20, 35, 60, 105, 106 |
| iMRI | Interventional Magnetic Resonance Imaging 14, 62 |
| iUS | Intraoperative Ultrasound 5, 17, 24, 60, 62–67, 69, 74–76, 78–81, 90, 96, 103, 104, 106 |
| IVUS | Intravascular Ultrasound 18 |
| LED | Light Emitting Diode 19 |
| MI | Mutual Information 22 |
| MPR | Multiplanar Reconstruction 39 |
| MRE | Magnetic Resonance Elastography 30, 31 |
| MRgHIFU | Magnetic Resonance-guided High Intensity Focused Ultrasound 27, 28, 30, 31 |
| MRI | Magnetic Resonance Imaging 3, 4, 7, 9, 10, 13–15, 21–24, 27, 29, 30, 37, 61, 63, 64, 66, 67, 71, 76, 78–80, 90, 101–103, 106 |
| MWA | Microwave Ablation 26 |
| NCC | Normalized Cross-correlation Coefficient 48, 87, 98 |
| OR | Operating Room 3, 7, 8, 10, 12, 14, 17, 19–21, 39, 60, 62, 64, 79, 81, 92, 100 |
| OTS | Optical Tracking Systems 18, 19, 21, 24, 104 |
| PCL | Point Cloud Library 89 |
| PET | Positron Emission Tomography 21, 22 |
| PLUS | Public software Library for US imaging research 34, 46 |
| PMC | Pivot Motion Compensation 42, 43, 53–58 |
| RF | Radio Frequency 13, 33 |
| RFA | Radiofrequency Ablation 26 |
| ROI | Region of Interest 45, 47, 48, 50 |
| ROS | Robot Operating System 34, 36–38, 49 |

| | |
|---|---|
| SAD | Sum of Absolute Differences 87, 98 |
| SSD | Squared Sum of Intensity Differences 22 |
| TEE | Transesophageal Echocardiography 18 |
| TheraGlio | Microbubble driven multimodal imaging and Theranostics for Gliomas 3, 90, 101 |
| TLD | Tracking-Learning-Detection 47–49, 58 |
| TRUS | Transrectal Ultrasound 18 |
| US | Ultrasound 2–5, 7, 11, 15–18, 21–24, 26, 27, 29, 30, 32, 34–39, 41, 45–47, 49–53, 58, 64–69, 71–74, 76–80, 90, 92, 96, 100–103, 106 |
| USE | Ultrasound Elastography 30, 31 |
| USgHIFU | Ultrasound-guided High Intensity Focused Ultrasound 27, 28, 30–32, 40, 58, 106 |
| VTK | Visualization ToolKit 38, 89, 90 |

# 1 Introduction

## 1.1 Motivations

Modern operating rooms are significantly different from what they looked like ten years ago: technology is revolutionizing the way surgery is carried on.

Clinical practice is drastically changing and surgeons need to adapt and renew their skills more often than before. Managing all of the different sources of information that are becoming available during any surgical operation is a complex task, and technology should help clinicians in exploiting their skills and knowledge at the best of their potential.

Advancements in the way critical surgical tasks are carried out are fundamental in order to improve the overall surgical outcome while reducing intervention time and enabling novel less invasive procedures.

Technology can help surgery in a number of different ways, from the realization of better simulating environments for surgeons' training, to comprehensive robotic approaches that need less and less human intervention to be carried on.

In this wide range of applications medical imaging always plays a key role, but its management and comprehension during surgery isn't always trivial. Intraoperative navigation systems have the problematic task of providing guidance during surgical procedures by efficiently and effectively exploiting the available imaging sources, often combining them with information coming from other devices located in the operating room.

Modern intraoperative navigation systems should make use of advanced computer science techniques related to the fields of image processing, computer vision and machine learning in order to provide the best possible guidance toward the surgical target.

Just as recent advancements in those technologies are helping the automotive sector in making autonomous vehicles happen, realization of autonomous surgical procedures may represent a grand challenge for the scientific community in the years to come.

In order to make the vision of self-guided procedures reality, advancements with respect to the current state of the art are much-needed, and gradual but constant changes to clinical practice should be introduced in order to help surgeons gain acquaintance with newer technology without posing risks to patients' health.

## 1.2 Context

This thesis aims at advancing the current state of the art in the field of intraoperative navigation systems in Image-Guided Surgery (IGS) by focusing on two different surgical scenarios that share the need for effective and efficient surgical guidance based on Ultrasound (US) imaging.

The first analyzed surgical scenario is the one of US-guided abdominal tumor thermoablation. In these kinds of minimally invasive procedures, which are described in details in Chapter 3, a tumor is treated by heating the malign tissue from outside the body without the need of using ionizing radiations. A robotic approach can be of great aid in these procedures by automatically delivering the therapy while ultrasound-based monitoring is employed to keep the patient safe. The final goal is to increase the treatment accuracy, minimizing side-effects and risks of relapses for the patients.

An effective intraoperative navigation system, in this context, should enable automatic guidance for the robotic platform toward the tumor, thanks to the information that is acquired from the US images (a robotic platform for tumor thermoablation is shown in Figure 1.1).

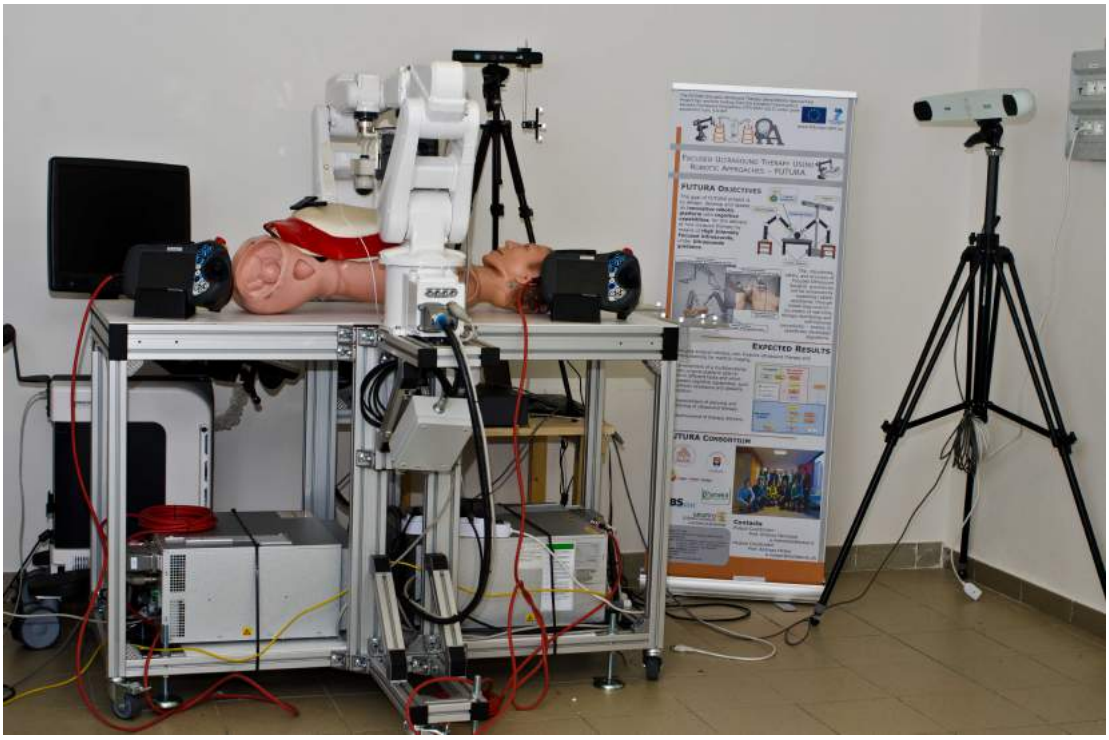


Figure 1.1: Setup for a robotic-assisted minimally invasive procedure. A surgical robotic platform, on the left, is used in conjunction with optical tracking systems, on the right and in the background.

The second analyzed surgical scenario is the one of US-guided neurosurgical tumor resection.

In these types of procedures, which are described in details in Chapter 4, a tumor is manually removed by a neurosurgeon after opening the patient skull. Intraoperative navigation systems are used in this context in order to verify resection completion with respect to preoperative data, usually Magnetic Resonance Imaging (MRI) and Computed Tomography (CT). The accuracy of these systems is usually limited by the changes occurring in patient anatomy during the procedure and by the lack of other effective intraoperative imaging sources.

By using US intraoperatively, surgeons can monitor the area of interest in real time. In order to use US efficiently and effectively surgeons may need help, which can be provided by image navigation systems via integration and fusion of US images with other information sources available in the Operating Room (OR) (an advanced neurosurgical operating room is presented in Figure 1.2).

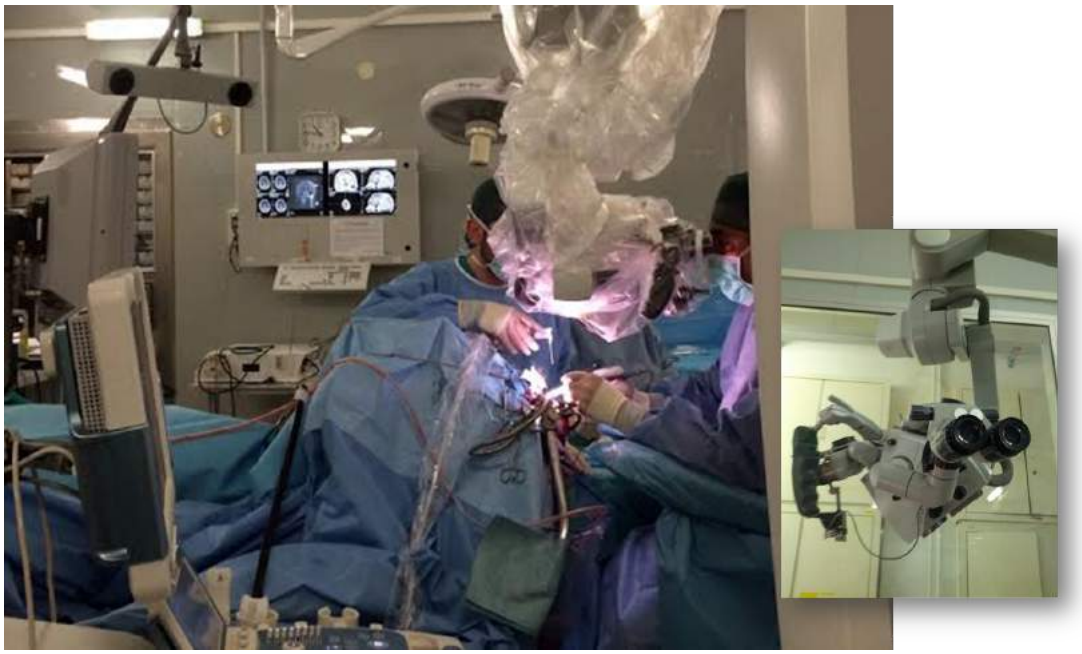

Figure 1.2: Example of an advanced neurosurgical operating room setup, the surgical microscope is highlighted on the right.

The work described in the following chapters of this thesis has been carried out in close collaboration with Camelot Biomedical Systems [1] and was partially supported by two European FP7 projects in which the author was involved:

- FUTURA [2], Focused Ultrasound Therapy Using Robotic Approaches (grant agreement n°611963), focusing on the development of a novel robotic platform for High Intensity Focused Ultrasound (HIFU) treatment.

[1] https://www.camelotbio.com
[2] http://www.futuraproject.eu

- TheraGlio [3], Microbubble driven multimodal imaging and Theranostics for Gliomas (grant agreement n°602923), focusing on the development of novel techniques for glioma surgery, including advanced image guided neurosurgical platforms.

Thanks to the collaboration with several clinical partners that were involved in the aforementioned research projects the developed techniques and systems have been tested on hardware and data coming from real surgical scenarios.

Similarities and differences of the selected surgical settings are highlighted in Table 1.1. While the outcome of effective image navigation is sensibly different, the instruments that are used in both of them are mostly in common, and require similar approaches to be integrated correctly.

| | Abdominal Thermoablation | Neurosurgical Resection |
|---|---|---|
| Preoperative Imaging | CT<br>MRI | CT<br>MRI |
| Intraoperative Imaging | 2D US<br>3D US | 2D US<br>3D US<br>Surgical Microscope |
| Tracking Devices | Electromagnetic Systems<br>Optical Systems<br>Robotic Arms | Electromagnetic Systems<br>Optical Systems |
| Goals | Robot Control<br>Treatment Monitoring | Advanced Image Fusion<br>Surgical Training |

Table 1.1: Comparison of the two selected clinical scenarios.

The key similarity of the selected clinical scenarios is the need to correctly understand US during the procedure. This observation was the main driver of most of this work, defining the main objective of providing surgeons - or robots - with powerful instruments supporting them in the non-trivial task of interpreting US information.

[3] http://www.theraglio.eu

The developed systems and techniques were designed in order to solve open problems arising in the context of image-guided (and specifically, US-guided) procedures, trying to bridge the gap between technological availability and clinical practice.

## 1.3 Thesis Structure

The thesis is organized as follows:

- Chapter 2 - **Background** - presents the main concepts related to the field of IGS. Emphasis is given to the current state of the art of image navigation systems and on the different elements that comes into play into their realization. The aim of the chapter is to clarify which instruments and techniques are currently employed in this field and which problems are there to be solved.

- Chapter 3 - **Ultrasound-Guided Minimally Invasive Surgery** - describes the design, development and testing of a navigation system which is applied to a novel robotic platform for abdominal tumor thermoablation using HIFU. The general principle and the main applications of the HIFU technology are presented, together with the most relevant approaches for guiding the procedure. The task of motion compensation during HIFU therapy is especially detailed and a novel US-based approach is presented together with experimental results related to ex-vivo experiments.

  Part of the work described in this chapter has been published by the author in [CMD+15], [DSC+17] and [DCS+17].

- Chapter 4 - **Ultrasound-Guided Neurosurgery** - describes the design, development and testing of techniques based on image navigation and fusion tailored to the surgical scenario of neurosurgical tumor resection. The basic principles of tumor resection in neurosurgery are presented, with a focus on the usage of Intraoperative Ultrasound (iUS) and other intro-operative imaging sources. The developed applications aim at aiding the task of target identification in iUS during neurosurgical procedures through a) effective training through simulation and case rehearsal and b) intraoperative fusion with surgical microscopy data. Experimental results are presented for both of the applications, and their potential integration in a unique framework is discussed.

  Part of the work described in this chapter has been published by the author in [PPM+17].

- Chapter 5 - **Conclusions** - summarizes the main results of this work, highlighting the novel contributions that were provided with respect to the current state of the art. Open problems are presented together with future research opportunities in this field.

# 2 Background

This chapter will present the fundamental concepts related to IGS. The main instruments and techniques that have been used in this field will be presented, with a particular focus on the ones that are related to the clinical scenarios which are the object of this thesis.

After two preliminary sections about the history of IGS and the definition of intraoperative navigation systems, this chapter will describe a) the basics of the most relevant imaging modalities that come into play in IGS, b) the different kinds of tracking devices that are usually found in modern operating rooms and c) the main intraoperative image fusion techniques that are employed in this field.

## 2.1 Image-Guided Surgery

Image-Guided Surgery (IGS) can be defined as any surgical operation in which the surgeon employs tracked instruments together with preoperative and intraoperative imaging in order to guide the procedure.

The combined hardware and software system used to guide the procedure is called intraoperative navigation system [MJB13]. The general scheme of an IGS application that exploits an intraoperative navigation system is presented in Figure 2.1.

IGS is employed in a number of different clinical scenarios, whenever the surgeon needs additional information and guidance in order to complete complex procedures in which accuracy is critical.

Preoperative and intraoperative imaging, and more often a combination of the two, may be necessary in several cases to improve the outcome of the procedures. Examples include:

- When patient-specific preoperative plans have to be applied with great accuracy in the operating room;
- When the preoperative plans have to be be adapted to physical changes in patient anatomy during the procedure;
- When visual and/or tactile information do not suffice for accurate tissue differentiation during surgery;
- When surgical targets are not directly accessible to clinicians during the procedure;

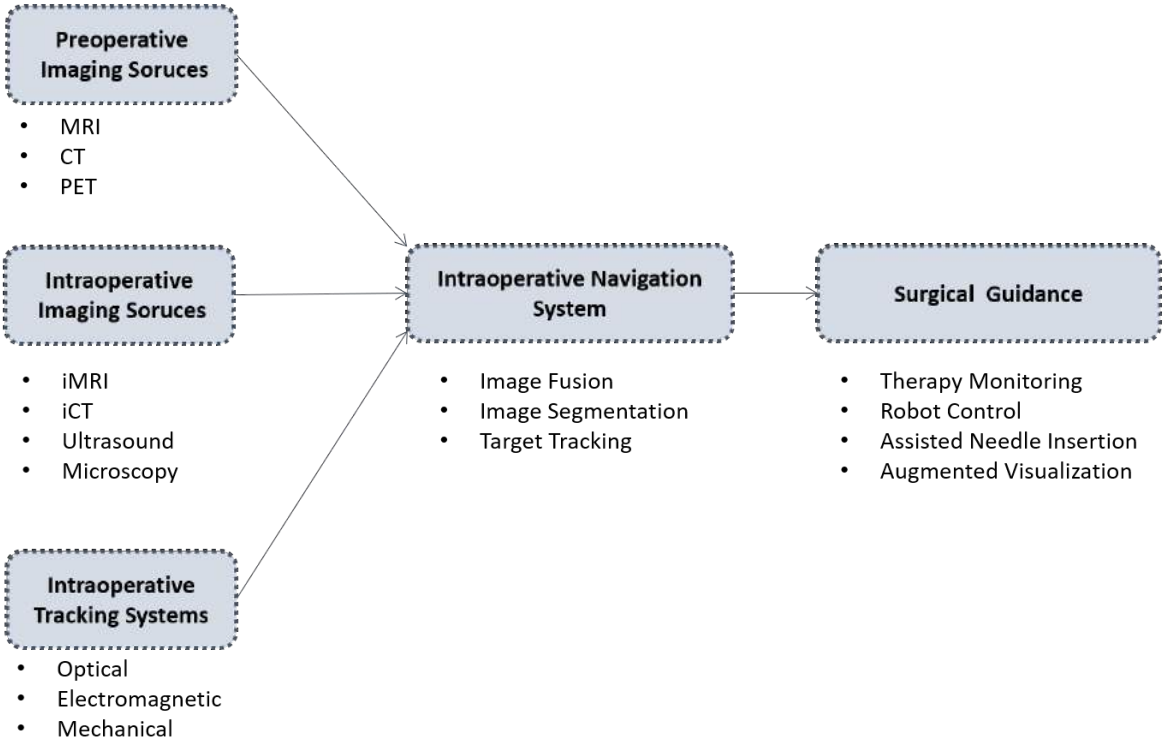


Figure 2.1: Scheme of a generic IGS application.

Two already mentioned examples of clinical scenarios that require IGS for different reasons are neurosurgical tumor resection and minimally invasive tumor ablation. In the former, a combination of preoperative CT, MRI and intraoperative US can significantly help the surgeon in the discrimination between tumor mass and healthy tissue, in the latter, usage of intraoperative imaging data is the only way to guide the procedure since no incision is done and there is no direct access to the area to treat.

Modern IGS had its origin in the 1980s when enough computing power became available for advanced medical applications based on volumetric images. [ADB+15]. One of the first application of IGS was presented in the context of neurosurgery in [JSM+80] in which a rudimental micromanipulator was employed to target lesions identified on 3D reconstrucions of tumor volumes.

Three major milestones are represented by

- [RSH+86], in which the first example of registration based on fiducial markers was presented, together with a system that exploited microphones to track the position of a microscope in the OR.

- [HMW+92], in which a computer vision system was presented exploiting video cameras to track objects in the OR.
- [WWM+87], in which the position of a surgical probe in the OR was tracked by means of a mechanical arm.

The integration of these works by the neurosurgeon Rich Bucholz resulted in a patented system for brain surgery [Buc95] that after a number of refinements became the first complete IGS system in the market, namely, the Medtronic[1] Stealthstation (Figure 2.2).

Figure 2.2: The latest version of Stealthstation by Medtronic, which uses infrared optical tracking technologies to perform patient registration and image navigation.

Around the same time, image guidance started to be used in minimally invasive surgery. Radiosurgery, in particular, saw the growth of stereotactic radiation therapy [ADB+15], the efforts of several groups resulted in a system patented by John Adler in the 1990s [Adl93], which later became the Accuracy[2] CyberKnife, one of the first modern robotic approaches for minimally invasive IGS.

[1] www.medtronic.com
[2] www.accuracy.com


Figure 2.3: The Accuracy Cyberknife, a FDA approved robotic radiosurgery approach employed in the treatment of tumors.

From these pioneering works, a number of different approaches were developed and deployed in different surgical fields, including interstitial therapy, orthopedic and spinal surgery, endoscopy, and many others [ADB+15].

The main functionalities of typical image guidance systems can be split into: a) image acquisition, b) planning, c) registration, d) instrument tracking e) visualization. [ADB+15]

- Image acquisition is the process of obtaining preoperative images, usually high definition CT or MRI, that will be later used by the navigation software.
- Planning refers to the task of accurately defining how the intervention will be performed, for example by defining trajectories, entry points, or by segmenting area of interest in the pre-operative images.
- Registration is a process in which the reference frame of the preoperative images is linked to the real space of the operating room, for example by exploiting tracking technologies to outline on the patients well-known reference points already selected in the images.

- Instrument tracking refers to the continuous and real-time identification of the relevant surgical instruments position and orientation in the operating room space, by exploiting tracking technologies.
- Visualization is the key step that lets the surgeon exploit all of the information that is generated by the system, usually in high-definition monitors positioned inside the operating room.

In addition to these steps, when intraoperative imaging sources are employed, guidance should be provided by the system via the processing of the available intraoperative images, possibly in real-time, in order to provide updates with respect to the original surgical plan and, when applicable, automate the procedure as much as possible.

## 2.2 Intraoperative Navigation Systems

The key component of any IGS procedure is represented by the intraoperative navigation system [MJB13].

The main tasks of any intraoperative navigation system can be summarized as a) the continuous localization in the OR space of all of the different elements that come into play into any surgical theater, including the patient and the employed surgical instruments, and b) the management and elaboration of different pre-operative and intraoperative imaging sources with the final goal to provide useful functionality to guide the procedure.

The first task is crucial in order to update in real time the relative position of surgical instruments, which can be manually operated or robotized, with respect to the patient, which sometimes is asleep and immobilized, but may as well be awake or just partially anesthetized.

This result is usually obtained with the help of optical or electromagnetic tracking systems, which are further described in Section 2.4.

Regardless of the type of technology that is used, tracking is usually obtained by exploiting particular markers or sensors that can be placed on the patient and/or on the surgical instruments in order to localize their relative positions in the OR.

When the position of the patient in the operating room space is known, it is possible to map pre-operative imaging data, like CT or MRI, to the patient on the operating table. This result is usually obtained by selecting anatomical features (i.e. landmarks) in the images and in the patient (e.g. with a tracked pointer).

In this way specific annotations (e.g. tumor segmentations, surgical paths, key anatomical structures) that were added to preoperative data before surgery can be exploited during the procedure by means of the navigation system in a process called image navigation.

Whenever new imaging data is acquired during surgery (e.g. as in the case of US and surgical microscopes) and the source of the new data (e.g. the US probe or the microscope head) is tracked by the navigation system, it is possible to display intraoperative images together with pre-operative images to enhance their informative content.

This process is called image fusion (see Section 2.5 for additional details). Depending on the type of the imaging data that has been acquired, different steps may be needed in order to correctly display the pre-operative and/or intraoperative images in order for the fusion to be correct and informative.

Modern intraoperative navigation system can incorporate several advanced features, examples include automatic compensation of non-rigid deformations in the patients anatomy [RLR+07] (e.g. due to changes in patient conditions with respect to the the original plan), segmentation of areas of interest [WNB+00] (e.g. tumors or vessels), or detection and tracking of specific features of interest in the images [DLBK+15] (e.g. to compensate organ motion due to breathing).

These functionalities can be critical in order to adapt the surgery with respect to the changes in the anatomy of the patient during the procedure or to react to unexpected deviations with respect to the original surgical plan.

Each surgical scenario (e.g. neurosurgery, abdominal surgery, orthopedic surgery) has very different requirements with respect to image navigation, and requires different solutions.

In the following sections, the main elements that are exploited by common intraoperative navigation systems are briefly presented.

## 2.3 Relevant Imaging Modalities

In this section the main imaging modalities that are integrated in intraoperative navigation systems will be briefly described.

The basic principles that are exploited in order to provide relevant imaging of the human body will be briefly presented, and their main intraoperative usage in IGS procedures will be highlighted.

A more detailed description of the usage of intraoperative imaging modalities in the context of the specific surgical settings which are the main object of this work is deferred to Chapter 3 and Chapter 4.

### 2.3.1 Computed Tomography

Computed Tomography (CT) is an imaging technique based on the well-known principle that the electron density and the atomic composition of a tissue influence the attenuation of an X-ray beam

passing through it. Since the resulting X-ray attenuation can be measured by suitable detectors, it is possible to obtain 2D projections of 3D structures. [Weh15]. By acquiring multiple 2D projections (e.g. using an X-ray tube which rotates around the body of the patient and measuring the radiation attenuation thanks to detectors located around the patient) a volumetric image can be computed by exploiting the concept that the internal density of any object can be reconstructed from several X-ray projections acquired from different point of views [LTK16].

Depending on the type of CT system in use, the shape of the X-ray beam (e.g. fan shaped, cone shaped), the number and position of the detectors, and the relative movements between the tube and the detector may change [Gol07].

#### 2.3.1.1 Interventional CT

Traditionally used just as a diagnostic tool and as a preoperative tool for surgery planning, CT has also been used, both historically and in recent times, to provide guidance in different kind of procedures. The main advantage of CT in this context is its capability of generating high-quality and accurate tomographic images, which are suitable for intraoperative navigation.

Compared to other commonly used intraoperative imaging modalities, CT has two main disadvantages: a) it is based on ionizing radiation, which may cause risks in both the patients and the physician, b) it is only sensitive to electron density, thus not providing the variety of information that other imaging systems may provide, especially when there is the need to discriminate between different soft tissue types or when other parameters (e.g. temperature) have to be monitored.

Historically, Interventional Computed Tomography (iCT) procedures has been applied to diagnostic biopsy procedures on a variety of anatomical districts (including, head, live, kidney, and bones) and to other percutaneous procedures including denervations and fluid collection [MB88] [C$^+$96]


Figure 2.4: The Medtronic OArm system for portable iCT.

Early approach to iCT in the OR presented nevertheless major difficulties due to iCT scanners

bulkness, incompatibility with other surgical tools and inferior image quality with respect to standard non-portable CT scanners. Operating directly in the radiology room, on the other hand, suffers from the disadvantage of the lack of access to full surgical equipment in case of need [SSP14].

Newer generation of portable Cone Beam Computed Tomography (CBCT) scanners, designed for intraoperative use, as in the case of Medtronic O-arm depicted in Figure 2.4 are helping in spreading the usage of iCT, thanks to the compatibility with standard surgical tables, higher image quality and shorter scan times[CTB+11] (i.e. a standard 3D volumetric scan takes 21 seconds, and has a 0.415 mm x 0.415 mm x 0.833 mm resolution for a 20 cm field of view[KKKH12]), and built-in registration and navigation features [SSP14].

### 2.3.2 Magnetic Resonance Imaging

Magnetic Resonance Imaging (MRI) is a non-invasive imaging technology based on the principle that a magnetic field and a Radio Frequency (RF) pulse can be applied to hydrogen atoms in the body in order to measure their response, which is linked to properties of the surrounding tissue. MRI doesn't use ionizing radiations, therefore it is considered safe for the patient (differently from CT).

A simplified MRI system is composed by a magnet, a transmitter RF coil and a receiver RF coil [WR11]. The magnet is exploited to align the spin direction of hydrogen atoms in the body. The spin direction is then modified by applying an RF pulse at the resonance frequency (i.e. also called Larmor frequency, the frequency at which the RF pulse energy can be absorbed by the hydrogen atoms) produced through the transmitting coil.

Hydrogen atoms return to equilibrium in a process called relaxation and the energy released during this process, in the form of RF signals, is measured by the receiving coil. This measurement can be spatial encoded thanks to a gradient magnetic field which is superimposed to the main field via specialized gradient electric coils which make the resonance frequency of hydrogen atoms vary with their position.

Since relaxation rate varies depending on the atom position and on the surrounding tissue properties, and can be altered by applying different RF pulses and magnetic gradients, MRI can produce images that measure different properties of the volume of interest.

Two main kind of relaxations are exploited by MRI systems: longitudinal and transverse relaxations, also called T1 and T2, respectively. [WR11] [GTC+15].

- T1, also known as spin-lattice relaxation, is a measure of the time taken for the spin of hydrogen atoms to realign with the MRI magnetic field. During T1, the energy is dissipated into the surrounding lattice and the longitudinal components of the magnetization decay

[WR11] [GTC+15].

- T2, also known as spin-spin relaxation, is a measure of the time taken for the spin of hydrogen atoms to lose phase coherence among themselves. During T2 the energy is redistributed among the atoms and the transverse components of the magnetization decay [WR11] [GTC+15].

A combination of a number of RF pulses and gradients at different times (i.e. an MRI sequence) can interfere with these two processes, thus modifying the received RF response and generating images with different appearances which can highlight a particular tissue of interest (Figure 2.5).

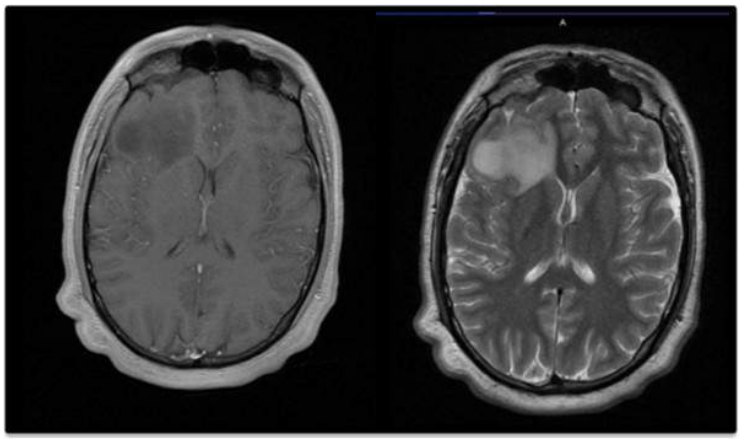

Figure 2.5: Example of brain slices acquired with different sequences. On the left a sequence highlighting T1 relaxation time, on the right a sequence highlighting T2 relaxation time. From [TBV+12]

.

As its costs decreases and its availability improves, the use of MRI is spreading in clinical practice [GTC+15] [ND14], and its usage is becoming relevant also during surgical procedures.

#### 2.3.2.1 Interventional MRI

Interventional Magnetic Resonance Imaging (iMRI) is employed in procedures in which MRI system can be moved into ORs when needed, providing up-to-date images during surgery. These images can be integrated into an intraoperative navigation system in order for them to be efficiently and effectively used by surgeons. iMRI is currently employed in different kinds of therapies, including tumor resections, epilepsy surgery, surgery for Parkinson's disease and spinal surgery [KtMS+11] [ASB04] [OZG+16], [FZB09].

Two main types of iMRI procedures can be identified [Ged00]:

- In the first type, the procedure takes place next to the MRI scanner. When needed, the patient is moved into the magnet, when the required images are acquired, the patient is taken out of the MRI and the surgical instruments are repositioned. In advanced solutions, like the IMRIS[3] system, a dedicated high-field MRI magnet can be moved inside and outside of the OR at need, thus reducing the need of moving the patient.
- In the second type, the procedure takes place inside the MRI scanner and MRI is used for continuous and online image-guidance. An open MRI scanner has to be employed in these procedures, that allows direct access to the patient for the operating team, typically at the price of lower image quality. Recent advancements are enabling the production of higher fileds open MRI (like the Hitachi[4] Oasis 1.2T, which is depicted in Figure 2.6) thus increasing the image quality of these kind of systems.

One of the main limitation of both of the approaches is related to the fact that the MRI scanner requires additional specialized equipment, like non magnetic surgical instruments, and MRI-compatible electronic devices (that do not interfere with the imaging process, and are not affected by the presence of the magnetic field).

In general all the tools that are brought into or near an MRI have to be properly assessed or shielded, further increasing the general cost of the setup for MRI guided surgical procedures.


Figure 2.6: The Hitachi Oasis 1.2T, an high-field open MRI scanner, which can be employed for interventional procedures.

Compared to other intraoperative modalities, some disadvantages are: a) longer scan times (i.e. depending on the sequence, usually 10 to 20 minutes [RPBJH+11] [SSMN14], while iCT scan

[3] www.imris.com
[4] www.hitachimed.com

takes usually less than a minute [CTB+11]) that make iMRI more sensitive to patient movements, more expensive in terms of OR usage time, and less suitable to be used in emergency situations; b) lower signal to noise ratio when higher spatial resolution is needed (e.g. typical reported slice thickness over 2 mm [ZDLRB+16] [HWB+11] [CPS+16] compared to under 1 mm thickness for portable iCT scanners [CTB+11]), a problem which is especially highlighted in the case of low field magnets, and can be mitigated through advanced iMRI scanners with higher field magnets.

### 2.3.3 Ultrasound

Ultrasound (US) is an imaging technique based on the principle that high-frequency sound waves can be applied to the body in order to record their echoed reflections, getting information about the internal body structures in the process. The acoustic waves are created by a transducer composed of a number of piezoelectric crystals capable of converting electrical energy into mechanical energy by oscillating.

The waves are generated while keeping the transducer in contact with a media (usually a gel with an acoustic impedance which is close to the one of water) that provides acoustic coupling between the transducer and the skin of the patient. While they propagate through the body, they are partially or totally reflected as they cross tissues of different impedance. Their echoes are captured by the transducer crystals, which convert them back into an electrical impulse.

The generated impulses can be used to reconstruct images of the tissue underneath the probe. Depending on when the echo was received the depth of an interface between tissues can be estimated. The intensity of an echo gives information about the impedance of the tissues forming that interface. If the difference is too high (e.g. when a bone is encountered), then the waves are completely reflected, resulting in strong echoes on the interface and no information coming from deeper areas. On the other hand, water and other homogeneous fluids do not produce echoes.

Since 1D transducer are usually employed, which exploits a number of elements disposed either in a linear or curvilinear shape, multiple echoes are simultaneously received from a section of the body, forming a cross-sectional representation. When Brightness Mode (B-mode) is employed, each echo is converted to a pixel in an image, its brightness being dependent on the amplitude of the echo, and its position in the image being dependent on the time taken by the echo to be received. Such an image represents the slice of body underneath the transducer (the transducer being at the top of the image), and highlights the interfaces between different tissues.

Compared to other imaging systems, US has several peculiarities: a) it provides continuously updated images with high frame rate, b) it is small and portable, c) it is relatively cheap, and d) it does not use ionizing radiations, thus being safe for the patient.

On the other hand, US has a limited field of view, it needs a clear acoustic window (i.e. the structure to be imaged should not be occluded by bones or air bubbles, that may completely

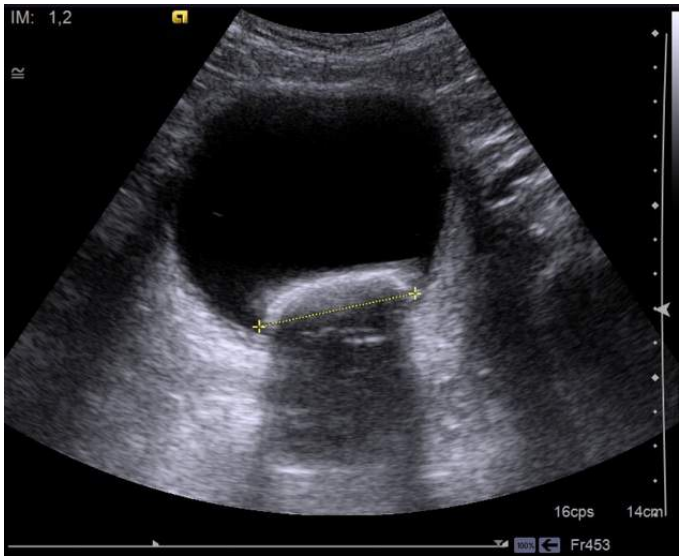


Figure 2.7: An example of B-mode US image, a bladder calculus is highlighted by the shadow artifact that corrupts the image underneath it.

reflects the ultrasound waves) and it is strongly operator dependent. Moreover, several sources of artifacts can corrupt the images which can be correctly identified only by experienced users.

Another typical limitation is related to the 2D nature of typical US acquisitions, but several approaches exist in order to overcome this issue, thus obtaining 3D US volumes.

The problem of obtaning 3D US volumes can be tackled with different technologies, each one with a specific tradeoff regarding image quality, 3D reconstruction accuracy, acquisition speed and costs. Real-time 3D US data acquisition techniques can be divided in: 2D array transducers, mechanical probes, mechanical localizers, and freehand scanners [HZ17]

- 2D array transducers, that replicate the acquisition process of 1D transducer exploiting 2D patterns. The elements of a 2D array transducer generate a diverging beam and the received echoes are processed to generate 3D US images [HZ17]. Several technical difficulties have to be faced in the realization of 2D array transducers, including challenges for impedance matching of the elements of the transducer, cross-talk between the elements, and small field of view. [HZ17] Despite these difficulties, 2D array transducers are the only 3D US technique that in theory guarantees a volume update rate (up to 60 volumes per second [HZ17]) which is suitable for real time applications (e.g. organs tracking in 3D).
- Mechanical Probes, that exploit a classic linear array transducer, which is rotated, tilted or translated automatically by a motor in order to sequentially acquire multiple US slices, which are interpolated to compose a 3D volume [HZ17]. While simple to realize, the main downside of this approach relies in the relatively long time needed for completing

the acquisition (i.e. usually 15-20 frames per second can be acquired and added to a volume, which depending on the required resolution can take several seconds to be updated completely [HZ17]), which can cause artifacts due to motion, making them not suitable for real-time applications.

- Mechanical Localizers, which consist of external instruments holding a traditional US probe. The localizer is moved automatically following a pre-defined pattern, to acquire a sequence of 2D images which can be interpolated into a single volume. While their compatibility with any commercial probe is a plus, the mechanical localizers are usually bulk and they share the same downsides of the mechanical probes regarding speed [HZ17].

- Freehand scanners, which exploit an external tracking system (usually already employed in the tracking of other devices in the OR) to record the position and orientation of the US probe. These information can be elaborated in order to reconstruct a 3D volume. Some important advantages are related to their flexibility and easy integration with other existing applications (e.g. for multimodal image fusion purposes). On the other hand, 3D scanning speed is further reduced (i.e. around 10/15 frames per second are used to update a volume [HZ17]) and image quality is more dependent on the operator, who has to be capable of acquiring enough images of the area of interest without creating artifacts when moving the US probe.

#### 2.3.3.1 Intraoperative US

Being portable, cheap and real time US is suitable for intraoperative applications.

As often in IGS, it is the neurosurgical community that first experimented with Intraoperative Ultrasound (iUS) in surgical guidance [DNMDM+10] [LTR+06], usually in combination with optical tracking systems. US is particularly valuable in neurosurgery because it could provide a reliable solution for the brain shift compensation problem [LWVN05] [RDSC07]. More details about US in neurosurgery are provided in Chapter 4.

Due to its real-time nature, US imaging have also gained popularity for motion compensation purposes. This can be particularly useful in minimal invasive interventions, as in the case of HIFU therapy, which is described in details in Chapter 3.

US based motion compensation for needle insertions operations has been especially relevant in cardiosurgery [LMWP10], in which the motion of an instrument had to be synchronized with the cardiac motion. This approach could be useful when deploying robotic approaches [VMMB07][YVPH13] [NNB11].

Other fields also benefited from the advancements in US technology, and especially from the miniaturization of US probes [HGHS98] [SRB+05] [IMLB03] allowing for integration of US into different surgical devices.

This is the case of endoscopes and catheters, as in Endoscopic Ultrasound (EUS) [WSA+99] [DJK+15] and Intravascular Ultrasound (IVUS) [NKT+02], which are exploited for surgeries in which no direct access to the surgical target is available and intraoperative imaging is particularly needed. Transesophageal Echocardiography (TEE) is also used in clinical practice during surgery in aortic and mitral valve repair and replacement procedures [GMF+09], while Transrectal Ultrasound (TRUS) is routinely employed in prostate biopsies since its early days [CLHM93].

## 2.4 Intraoperative Tracking Systems

As mentioned in Section 2.2, intraoperative tracking systems are a fundamental element of intraoperative navigation systems. Accurate and real time tracking of surgical instruments, imaging sources and patient position is a necessity to realize efficient and effective surgical guidance.

Currently available commercial tracking systems can be divided into optical and electromagnetic systems, based on the employed technology. Both kind of systems have advantages and disadvantages, and can be suitable for different kind of procedures. Their basic principles are briefly presented in the following subsections.

### 2.4.1 Optical Tracking Systems

Most of the commercially available Optical Tracking Systems (OTS) share the usage of two or more cameras to detect the spatial position of suitable markers.

The first generations of OTSs exploited known pattern of Light Emitting Diodes (LEDs) fixed to surgical instruments or ultrasound probes. Multiple cameras located above the OR were used to triangulate the position and orientation of the LEDs, thus tracking the tool they were attached to [ADB+15]. These kind of systems are classified as "active" OTSs, since the markers actively emit light in order to be detected, and they have to be connected to an energy source to work.

Modern OTSs exploit infrared cameras and reflective spheres instead of LEDs (a commercial OTS, the NDI[5] Polaris, is shown in Figure 2.8). These kind of systems are classified as "passive" OTSs, since the markers only reflect light passively, thus removing the need for additional wires to be attached to the tracked tools.

Despite many successful documented applications [ADB+15], some drawbacks affect OTSs. The most evident limit of this technology is the need for a constant “line-of-sight”, which means that the optical markers have to be visible to the camera the whole time, with no obstructions, in order for navigation to continue [ADB+15]. In addition, this kind of technology is useless in

[5] www.ndigital.com


Figure 2.8: The NDI Polaris, an OTS which uses infrared tracking and is employed by several medical devices.

laparoscopic surgery (in which flexible instruments are inserted through small incisions in the abdominal wall to carry out an operation, and therefore being impossible to track via optical methods) an approach that is gaining increasing popularity and in which intraoperative navigation systems are especially useful.

### 2.4.2 Electromagnetic Tracking Systems

The mentioned limitations of OTSs are partially overcome by Electromagnetic Tracking Systems (EMTS). The main element of any EMTS is a magnetic field generator, which has to be placed near the surgical target, usually next to or under the patient .

Small Electromagnetic (EM) sensors are placed onto the surgical tools to be tracked. Currents are induced in the sensors by the EM field. The particular configuration of the sensor makes it possible to compute its distance and orientation with respect to the field generator by measuring the induced current [ADB+15] (a commercial EMTS, the NDI[6] Aurora, is shown in Figure 2.9).

Figure 2.9: The NDI Aurora, an EMTS commonly used for medical tracking applications.

EMTSs have the significant advantage of not needing a line of sight, thus being applicable in crowded surgical theaters or in surgical procedures in which flexible instruments have to be

[6] www.ndigital.com

tracked inside the body of a patient, as in endoscopic procedures, at the price of having additional wires attached to the objects to track.

One of the major drawbacks of EMTSs is related to noise produced by conductive materials, which can distort the sensor readings, and by ferromagnetic materials, which can distort the magnetic field.

In order to tackle this problem field distortions detection techniques have been proposed [PC08], but available commercial systems still require other instruments and devices used in the OR to be designed for compatibility with EMTSs in order to guarantee accurate tracking.

## 2.5 Multimodal Image Fusion

One of the key components of an effective navigation system for IGS is the capability of performing accurate medical image fusion, which is the task of displaying in a unique view multiple images from single or multiple imaging modalities in order to increase their clinical applicability for diagnosis, treatment and assessment of medical problems [NM14] [JD14].

Focusing on the development of techniques for automated medical fusion during intraoperative navigation, two main problems come into play:

- Accurate registration of the patient within the operating room space and accurate tracking of the intraoperative imaging sources;
- Motion compensation and deformation correction of intraoperative images with respect to pre-operative data,

The first problem is usually approached using OTSs and EMTSs [MYN13] for detecting the 3D position and orientation of markers placed on the patient. By manually or automatically selecting the same landmarks in pre-operative and intra-operative imaging datasets it is possible to obtain a transformation (usually rigid) that links the relative position and orientation of pre-operative and intraoperative images with respect to the OR.

These methods can be sufficient to obtain a good matching between the structures depicted in different imaging modalities, but this is often insufficient, since deformations, motion of the internal organs and changes in the position of the patient can severely influence the result.

The task of compensating those effects is commonly approached with a class of techniques in the domain of medical image registration (Figure 2.10).

Image registration has been applied extensively and with good success in a number of clinical applications to pre-operative imaging modalities [JD14], but when applied to intraoperative data several different problems arise

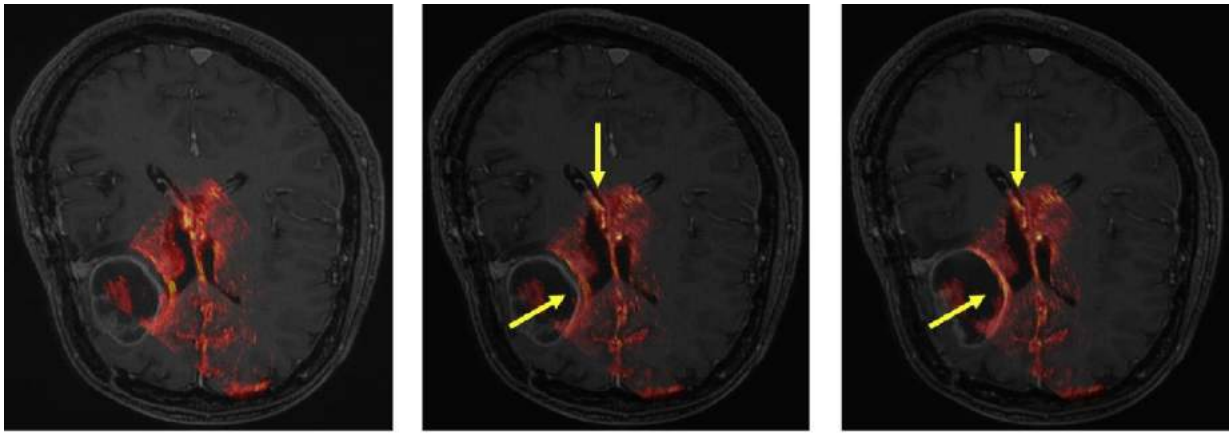

(a) Initial Alignment (b) Rigid Registration (c) Deformable Registration

Figure 2.10: An example of anatomical deformation correction using deformable registration in an US-MRI image fusion approach [FWMN14].

While pre-operative image-registration is typically related to volumes, when intraoperative imaging modalities are used images can represent two dimensional slices, as in B-mode ultrasounds, and/or to two dimensional projections of surfaces, as in intraoperative microscopy. Accurate registration of these kinds of data is a complex task that requires specific solutions.

### 2.5.1 Standard Multimodal Image Fusion

Most of the state of the art methods show successful applications in the standard settings of image fusion: MRI-CT, MRI-Positron Emission Tomography (PET), CT-PET fusion [JD14].

The key step of any classical image fusion method is image registration. The registration process requires a method to correct spatial misalignments between images resulting from scale changes, rotations, translations and deformations. The problem of registration becomes complicated in the presence of inter-image noise, missing features and outliers in the images [HBHH01].

The typical classification of image registration methods[MV98], which is still valid to these days [VMK$^+$16] [MTLP12] [EGEA16] is based on the following basic subdivision criteria:

- The **dimensionality** of the transformation (including both spatial and temporal dimensionality). Regarding spatial dimensionality, 2D-to-2D, 3D-to-3D and 2D-to-3D registration are possible. The latter is particularly relevant in recent approaches [MTLP12] [VMK$^+$16] also due to the diffusion of the need in IGS for image fusion between US and preoperative volumetric images (e.g. usually CT or MRI) [MA13]. Temporal registration is employed when, e.g. the evolution over time of a disease has to be quantified, motion has to be compensated or when physiological processes has to be monitored.

- The **registration basis**. The primary distinction is between extrinsic and intrinsic methods. In extrinsic methods external instruments are employed in order to perform the registration, as in the case of stereotactic frames or markers attached to the patients [MA13]. Intrinsic methods, on the other hand, rely only on the image content and exploit anatomical landmarks, segmentations and/or voxel intensities in order to guide the registration process. Voxel based methods have been the prominent approach in the field and are still the method of choice for multi-modality applications [VMK+16]. The key element in these approaches is the definition of a similarity measure, or metric, which is a general quantitative measure of the alignment of the two images. The most notable examples are Squared Sum of Intensity Differences (SSD) and Cross-correlation Coefficient (CC) [AvSSC08], used for intra-modality registration, and Mutual Information (MI) [WVA+96] for inter-modality registration.

- The nature of the **geometric transformation** that one tries to estimate between images. A key distinction is between rigid and deformable models [KSM+10]. Much of the early work done in radiology has involved the rigid registration of brain images of the same subject acquired according to different modalities (MRI, CT or PET) [PCS+89]. Since then research has mostly focused on deformable registration [HBHH01] [KSM+10], which is needed for compensating organs displacement, patient movements and inter-subject differences. Despite the popularity of deformable registration, it is reported that clinical practice still relies on simpler rigid registration approaches [VMK+16].

- The **domain** of the transformation, which may be global, if the registration process is based on the entire image content, or local, if just a portion of the image is considered.

- The user **interaction** that can occur during the registration process. Registration methods are usually divided in automatic, semi-automatic and manual/fully interactive. While most of the advanced registration methods are designed to be fully automatic [MA13], user interaction is often used as an initialization step (e.g. providing a rough segmentation or selecting key anatomical landmarks and seed points) in order to speed up the registration process.

- The **optimization** process used in estimating the optimal set of registration parameters. The optimization process relies on the minimization of a cost function. If the cost function (or rather its derivatives) is sufficiently regular, a large number of standard techniques of optimization can be used. Among the most popular optimization methods used in image registration the most relevant are: gradient descent and its variations [RS10], stochastic gradient descent [WVA+96] and simulated annealing [ROC+99]. Furthermore, it is important to remind that in optimization it is sometimes advisable to use regularization [CJ01], in order to reduce sensitiveness to errors.

- The **modalities** involved in the registration process. Registration methods are often subdivided in four classes: a) mono-modal registration, when both of the images are obtained

from the same imaging modality, b) multi-modal registration, when the two images belong to different modalities, c) patient-to-modality registration, which are related to the task of intra-operative patient positioning with respect to pre-operative data d) modality-to-model registration, in which an image is registered to a model, often for segmentation purposes or for detecting anatomical anomalies [MV98] [VMK+16].

- The **subject** of the registration. Intra-subject registration is still the most common registration approach, especially in clinical practice [VMK+16], since it is critical to match multi-modal acquisitions (e.g. MRI and CT) of a patient for diagnostic purposes. Inter-subject registration is relevant when several patients have to be compared, while atlas registration is employed when a set of reference images is used, often to transfer annotations and segmentations to a target image [AHH+09] [LVSOMR02].

### 2.5.2 Ultrasound and Image Fusion

US, being a real-time imaging modality, is becoming progressively more widespread during surgical procedures. As mentioned in Section 2.3.3, one severe limitation of US is that image quality is highly linked to the operator skills. Moreover, US images aren't easily understood by non trained surgeons.

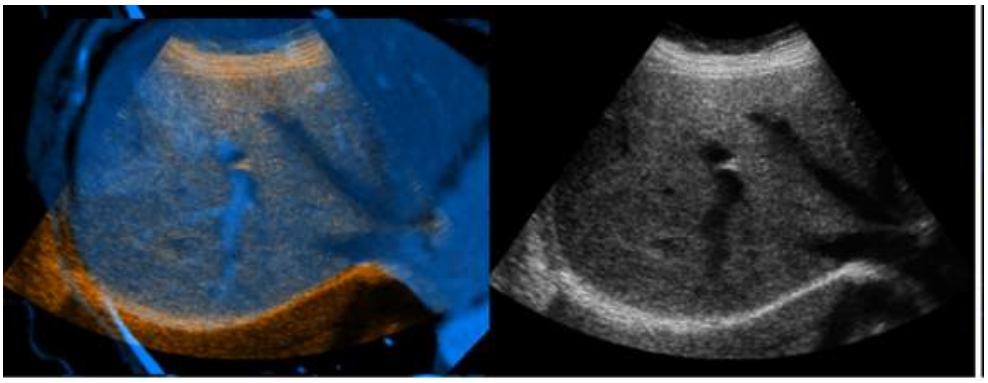

Figure 2.11: An example of US-CT image fusion result, from [WBK+08].

This factors lead to the usage of fusing US with other modalities to get a better understanding of the anatomical regions to analyze. Examples of fusion techniques that incorporate ultrasound are US-CT [DMS09] [WBK+08] [HDDC+11], US-MRI [MYN13] and PET-CT-US [WSP+11]. Functional imaging data (i.e. data that focuses on delinating physiological activities in the body, often by revealing spatial distribution of a chemical compound) has also been fused with US, as in the case of US-nuclear gamma probes data fusion [WFT+07]. US–US registration and fusion is also employed in some techniques [YNA02][SRG+10] for combining multiple US acquisitions

of the same anatomical area in order to improve signal-to-noise ratio in comparison with single scans.

Standard voxel-based intrinsic registration methods are known to fail in registering US with other modalities, but different valid approaches are known from literature:

- Model based approaches, exploiting the matching of a deformable shape model (which may be generated from pre-operative data, or directly from 3D US) to the image or to an extracted surface. Model based approach examples comprehend applications to prostate interventions, [HAT+12], liver interventions [KZW+12], lumbar spine needle injection [KMG+10], femur and pelvis surgery [BCE+08].
- Simlarity based approaches, based on the usage of ad-hoc defined metrics in order to find similarities between US and other modalities. The employed metrics usually exploit functional relationships between appearances in different modalities, while being as insensitive as possible to typical US artifacts[NNB11]. Sometimes standard registration approaches are employed only after relevant preprocessing steps, aimed at extracting properties of each image to be later registered in place of intensities (e.g. vesselness measures [PBH+04], local-phase representations [MB05] [ZNB07])
- Simulation based approaches, based on the generation of pseudo-US, which are transformed MRI/CT scan in order to match the intensity patterns of US acquisitions. These techniques can be applied either through pre-processing or through incorporation of the transformation function in the chosen similarity measure [WBK+08] [KRM+10] [MFH+12] [FWMN14]. Standard deformable registration can then be applied to pseudo-US datasets in order to find the transform between pre-operative data and intraoperative US.
- Landmark-based approaches, which are simpler approaches, usually employed in routine clinical practice [MYN13], based on the matching of manually or semi-automatically defined points in the two images to be registered. The landmark points must be chosen so that it is easy to identify, segment or track them in the US stream (e.g. highly echogenic structures) [RDSC07] [PRS+01], sometimes these approaches are used in combination with similarity-based techniques [CHMB12] [LPH+09].

### 2.5.3 Surgical Microscopy and Image Fusion

Application of medical image fusion to surgical microscopes is a far less popular topic in medical image fusion literature, with few approaches documented, also due to limited availability of devices and datasets for research purposes. Early works on intraoperative microscope-MRI image fusion exploited OTS and standard computer vision techniques applied to a stereo surgical microscope, showing promising results [PFJ05] (Figure 2.12).

Figure 2.12: Early approach to surgical microscope image fusion with pre-operative segmentations from [PFJ05]. Two viewpoints of a virtual 3D scene in which the surface mesh is merged with segmentations highlighting a glioma (in blue) and other anatomical features of the brain.

More recent works focused on improving accuracy and stability of stereo reconstruction techniques applied to intraoperative microscopes to enable effective clinical usage [JFRP14][KMP+15].

Research in brain tumor treatment showed that microscope guided gliomas resection along with intraoperative MRI have been functional to improve tumor resection [STR+05] [KtMS+11]. iUS-guided resection could be an alternative solution, even though US images are often difficult to interpret [PVF+14]. Indeed both intraoperative microscope and US guidance proved to be functional to improve surgical outcome.

In order to provide neurosurgeons with a comprehensive intraoperative visualization of the area to treat, combining iUS with surgical microscope images and preoperative MRI could be highly desirable, as further detailed in Chapter 4.

# 3 Ultrasound-Guided Minimally Invasive Surgery

Advancements in technology keep on changing the broad field of surgery by enabling novel approaches that may improve clinical outcome for patients, while being more efficient and cost-effective. [VLCY13]

While aiding and enhancing the abilities of surgeons, technology is also redefining their skills, requiring a surgeon to constantly train and learn in order to be familiar to the latest tools, that can enable surgical workflows which are significantly different from the standard.

As remotely controlled instruments and video displays are becoming the standard in many procedures where minimally invasive surgery technologies are available, surgeons cannot rely anymore on their sight and on the dexterity and coordination of their hands.

Several robotic approaches have been developed in the latest years in order to help surgeons in the difficult process of adapting to novel procedures, which may require precision and dexterity that a human is not capable of providing.

Robotic approaches should help surgeons by enabling:

- Effective therapy planning, by providing novel ways to access intraluminal sites, reducing harm to the patient and thus post-treatment recovery;
- Efficient manipulation of target tissue with higher precision and dexterity;
- Advanced therapy delivery, by realizing tissue destruction using focused energy delivery devices or providing dissection instruments for resection or excision;

Among the wide range of approaches becoming available that could benefit from a robotic application, minimally invasive thermal ablation is becoming more and more common thanks to the advent of modern imaging technologies. [CD14].

Thermal ablation technologies are based on the local application of extreme, high or low, temperatures in order to cause tissue necrosis. This technique has been used in past for the treatment of many tumor types, including liver, kidney, lung, bone cancers, breast, adrenal glands, head and neck [CD14]. While percutaneous thermal ablation is mainly used nowadays for the treatment of a limited number of cases (based on the availability of standard surgical alternatives), studies show that it may offer various advantages including lower morbidity, reduced cost and increased preservation of healthy tissues [CD14].

In clinical practice, thermal ablation is usually obtained through Radiofrequency Ablation (RFA), Microwave Ablation (MWA), and cryoablation. Newer technologies, such as High Intensity Focused Ultrasound (HIFU), are less common but show promising results and are starting to be applied to a wider range of pathologies.

The focus of this chapter is to describe the design and development of a novel strategy to provide image guidance for robotic HIFU therapy delivery.

The main contributions of the author reside in:

- The complete design and development of a navigation system for a novel robotic platform for HIFU therapy.
- The complete design, development and integration in the robotic platform of a novel algorithmic pipeline to track respiratory motion of unknown targets in US images, to predict their trajectories and to monitor HIFU therapy delivery during robotic motion compensation.
- The major contribution to the design, development and validation of a novel angular motion compensation strategy for the aforementioned robotic platform.

Part of the work described in this chapter has been published by the author in [CMD+15], [DSC+17] and [DCS+17].

## 3.1 High Intensity Focused Ultrasound Therapy

High Intensity Focused Ultrasound (HIFU) is a non-invasive technology which can be used in the therapy of different kind of tumors in several anatomical districts. Examples of clinical HIFU application comprehend usages on breast, bones, prostate, liver, and kidney [FES+13].

Through HIFU, it is possible to deliver acoustic energy through the body, directly from an external transducer [LZCM42][FMJBF54] (Figure 3.1).

HIFU technology is based on the physical principle that an ultrasound field can be focused and applied to a tissue in order to cause mechanical stress in a process called HIFU sonication. Part of the ultrasound energy is absorbed by the tissue, causing a temperature increase which depends on its absorption coefficient. If an high enough temperature is reached for a certain amount of time, it is possible to damage the tissue in an irreversible way. [CTRG05]

By focusing US, HIFU can produce enough energy to cause tissue damages in a small volume (down to a cylinder with 1 mm diameter and a length 5/10 times larger than the diameter, depending on the employed HIFU transducer) [TMHJ11], inducing steep temperature changes (up to 100 °C)

in seconds, without damaging other tissues surrounding the target volume. Mechanical movement of the transducer or electronic steering can be employed in order to sequentially treat larger areas.

The damages caused to the target tissue by HIFU includes protein denaturation [FES+13], histotripsy by cavitation[RHI+06] and fragmentation by boiling [KWS+14]).

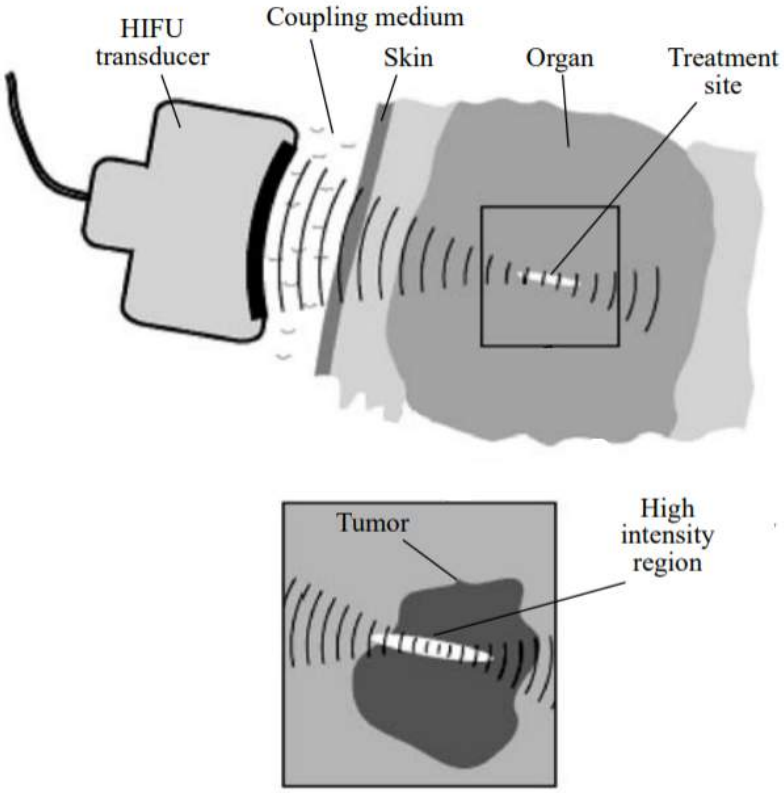


Figure 3.1: Schema of HIFU surgery, adapted from [BKS+03].

The first FDA approved HIFU system has been developed in the 1980's [Sil16], since then, thanks to the development of both HIFU technology and imaging technologies, HIFU started spreading, and an increasing number of clinical applications have been reported (Figure 3.2), including but not limited to tumor ablations [TATH+14] [IKW+05] (among other notable examples: drug delivery [CFK+14] and treatment of neurological disorders [MJM+09] [BMHL+14]).

Advantages with respect to standard invasive surgery include decreased morbidity [IKW+05] and increased accuracy (e.g. in HIFU tumor ablation under general anaesthesia ablated regions can be kept within 5 mm from the target, against the usual 1 cm or wider surrounding margin of normal tissue which is excised during surgical routine [IKW+05]). Despite this, some challanges with respect to patient safety and effective therapy delivery remain open, especially when applied to abdominal surgery [HKT+16] [CHCV15].

During HIFU therapy, different imaging modalities can be used in order to identify and monitor the target area. The main imaging modalities that can be used for these tasks are MRI and US, both presenting pros and cons.

When Magnetic Resonance-guided High Intensity Focused Ultrasound (MRgHIFU) is employed, clinicians can obtain high quality images, and temperature maps [SBD+13]. When Ultrasound-guided High Intensity Focused Ultrasound (USgHIFU) is employed, it is possible to verify the treatment acoustic window, and to monitor the target area in real-time, enabling more accurate compensation of organ movements [ETH15].

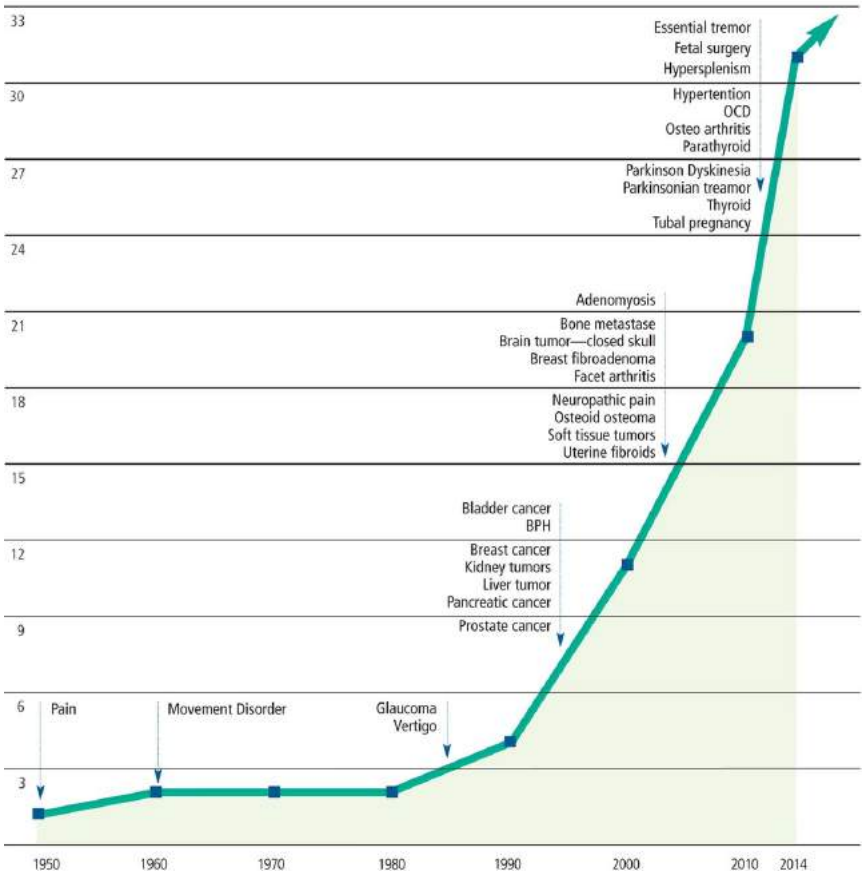


Figure 3.2: Timeline of HIFU clinical indications, adapted from [PSK16]

Regarding USgHIFU systems, several platforms already operate in clinical setting - examples include: HAIFU JC (Chongqing Haifu Medical Technology[1]), EchoPulse (Theraclion[2]) and Alpius (ALPINION Medical Systems[3]).

[1] www.haifumedical.com
[2] www.theraclion.fr
[3] www.alpinion.com

Despite their potential, the available clinical solutions for USgHIFU still present several problems which should be tackled, including the lack of flexibility in treating different targets (and especially the difficulies in treating moving targets without general anesthesia [IKW+05]) and the need for time consuming procedures (e.g. a median treatment time of 5.4 hours was shown in an early study on renal tumors [WWC+03]). For these reasons, novel approaches and image guidance strategies should be researched.

## 3.2 Image Guidance in HIFU Therapy

Image guidance is a key feature of any HIFU-based clinical solution. Both MRgHIFU and USgHIFU have been used succesfully to ablate solid tumors [WWC+04] [Ken05] [ZW10], but each image-guided method has several pros and cons, which are summarized in the following sections, highlighting how they come into play in each step of a typical HIFU procedure for tumor ablation.

### 3.2.1 Preoperative Stage: Therapy Planning

Any imaging system employed in HIFU therapy planning should help the surgeon:

- Identify the tumor borders with high confidence.
- Quantify the volume of the lesion to be treated.
- Measure the distance between the skin and the deepest surface of the lesion.
- Identify the best trajectory for carrying out the procedure.

MRI is the key modality for preoperative planning, providing volumetric images with high spatial resolution and thus enabling the assessment of tumor size and the identification of the surrounding structures [LW13].

Identification of the anatomical structures that surround the tumor is a crucial task, since the correct position of the transducer should be planned carefully in order to avoid the risk of damaging healthy organs, ribs, blood vessels or nerves.

US - and especially 3D US when available - can help in determining tumor borders, but overall MRI remains the modality of choice for tumor identification, MRI being able to detect lesions that are not apparent using US imaging only [LW13] (i.e. isoechoic lesions). On the other hand US is the modality of choice in the identification of areas which may reflect or absorb the acoustic waves of the HIFU, thus helping the identification of the best trajectory for the therapy.

Since both modalities have pros and cons, image fusion techniques should be considered in the therapy planning phase in order to combine their strenghts [WBK+08] [LKO+03]. Image fusion can help in the identification of the precise position of isoechoic lesions, small lesions, and lesions shielded by artifacts, gas, or the bones, while correctly identifying the safer trajectory for the therapy [LW13].

### 3.2.2 Intraoperative Stage: Therapy Monitoring

During any HIFU procedure, the imaging modality of choice should satisfy some requirements:

- The target and the focal spot should be easily identifiable in the images and the image quality should be robust to noise;
- If target deformation or movement occurs, it should be possible to detect it from the images in order to compensate it;
- It should be possible to quantify the extent of the HIFU induced necrosis in the target volume.

As mentioned in the previous section, target identification is possible in most cases with both MRgHIFU and USgHIFU. MRgHIFU, in particular, could provide better images since it is not affected by air bubbles or other artifacts that can be generated during the procedure.

Moreover, MRI is sensitive to temperature changes, thus enabling the identification of the focal spot in the images thanks to MRI thermometry [McD05]. Through MRI thermometry it is also possible to determine with good confidence the size of the focal spot of the HIFU system.

USgHIFU, on the other hand, presents several advantages in terms of motion and deformation compensation, which is a critical step in many procedures [CTT+12]. Thanks to US being almost real time, it is possible to employ dedicated algorithms in order to track and compensate breathing movements and other sources of deformations.

In order to assess the effects of the ongoing treatment, USgHIFU can rely only on immediate grayscale changes, which are a sign of a sufficient energy deposition causing cavitation bubbles and coagulative necrosis of the tissue [FNN+11] [YX08]. At the same time, grayscale changes are not always connected with complete necrosis of the cancerous lesion [LKO+03], and coagulative necrosis does not always show grayscale changes, despite confirmation from pathologic examination. Moreover, generated cavitation bubbles and other artifacts may alter the images creating problems in the observation of remaining tissue to treat.

Through MRI thermometry, as already mentioned, MRgHIFU procedures can rely on accurate temperature measurement in order to ensure that necrosis occurs on the basis of the in vivo-temperatures that can be monitored by an operator. Problems arise when breathing motion occurs,

since standard MRI is still quite slow to provide anatomic images for temperature measurements at high frequency, thus limiting the applicability of MRgHIFU [LW13]. Some recent advancements could tackle this problem, but are still in development [ZMF17] [BBdB$^+$16]. US thermometry, on the other hand still lacks decisive evidence toward a reliable clinical applicability [LSC15].

### 3.2.3 Postoperative Stage: Therapy Evaluation

After therapy, imaging should be used in order to verify the correctness of the treatment, which means to evaluate if all of the malign tissue was ablated correctly.

The means of evaluation of necrosis usually relies on elastography techniques [OCP$^+$91], which are available for both MRgHIFU, with a technique called Magnetic Resonance Elastography (MRE) [MGE10], and USgHIFU, through Ultrasound Elastography (USE) [Vap12]. Elastography enables the computation of the stiffness of a selected volume of interest.

The different kinds of elastography techniques that are currently developed or applied in clinical practice are based on the principle that mechanical properties can be inferred from a two-step process composed by a) distortion induction and b) response observation.

The first step (distortion induction) is usually performed in one among these three ways:

- Inducing vibrations in the anatomical area of interest with a dedicated tool;
- Using ultrasound to remotely push the tissue from outside;
- Exploiting distortions related to physiological changes (e.g. heartbeat)

The second step (response observation) is based on the principles that a) under stress less deformations are produced in stiffer tissues and b) mechanical waves travel faster in stiffer tissues.

Since the mechanical properties of normal tissue and ablated tissue are different, these differences can be imaged and quantified using elastography in order to assess the success of the HIFU procedure [LW13].

MRE was performed by [LGR$^+$06] as part of a HIFU procedure to obtain data for therapeutic evaluation. Different studies also used USE to monitor changes in tumor during HIFU therapy [TGO11].

Compared to MRE, USE has lower cost/efficiency, but has the drawback of being operator dependent, requiring the surgeon to be well trained in the specific technique in order to understand it correctly.

### 3.2.4 Other Remarks

Other factors, like cost and compatibility, play an important role in the choice oh the imaging modality to guide HIFU procedures, since they directly influence adoption rate and availability.

For instance patients with stents or prosthetic made of ferromagnetic materials are not suitable for MRgHIFU, since those materials may corrupt the images and cause safety issues.

MRgHIFU requires that all of the devices used during the procedure should be magnetically compatible, and has considerably higher costs than USgHIFU. Moreover MRgHIFU may create discomfort in the patients, while USgHIFU is much cheaper and comfortable for patients, and does not require additional equipment.

## 3.3 A Novel Robotic Approach to USgHIFU

Robotic assistance to HIFU surgery intrinsically adds robustness and reproducibility of the treatment, by allowing the implementation of automatic control strategies for image registration, therapy planning and optimal acoustic window definition, target identification, motion target estimation, ultrasound therapy and lesion assessment [VMO05] [SCC$^+$04][SSA04] [KMQ$^+$09] [DSB$^+$10].

In order to overcome the downsides of the currently available USgHIFU platforms, highlighted in the previous sections, an innovative robotic platform intended for USgHIFU procedures was developed within the Focused Ultrasound Therapy Using Robotic Approaches[4] (FUTURA) FP7 European project (grant agreement n°611963), in which robotics, therapeutic ultrasound, ultrasound guidance and machine learning algorithms were merged to improve current HIFU interventions [TCD$^+$17].

The control of two independent anthropomorphic manipulators provides the FUTURA platform with high flexibility in terms of operating workspace and maneuverability. The FUTURA platform as illustrated in Figure 3.3, is composed of a) a robotic module, b) a monitoring module and c) a therapeutic module,.

- **The robotic module** is composed by two anthropomorphic industrial manipulators (i.e.IRB 120, ABB[5], Zürich, Switzerland) equipped with two force/torque sensors (ATI mini 45, NC; USA). The force/torque sensors are fixed to the end-effectors of the robots and they are used in the integrated control force of the IRB 120, which allows exerting controlled forces along specific directions.

[4] www.futuraproject.eu
[5] new.abb.com

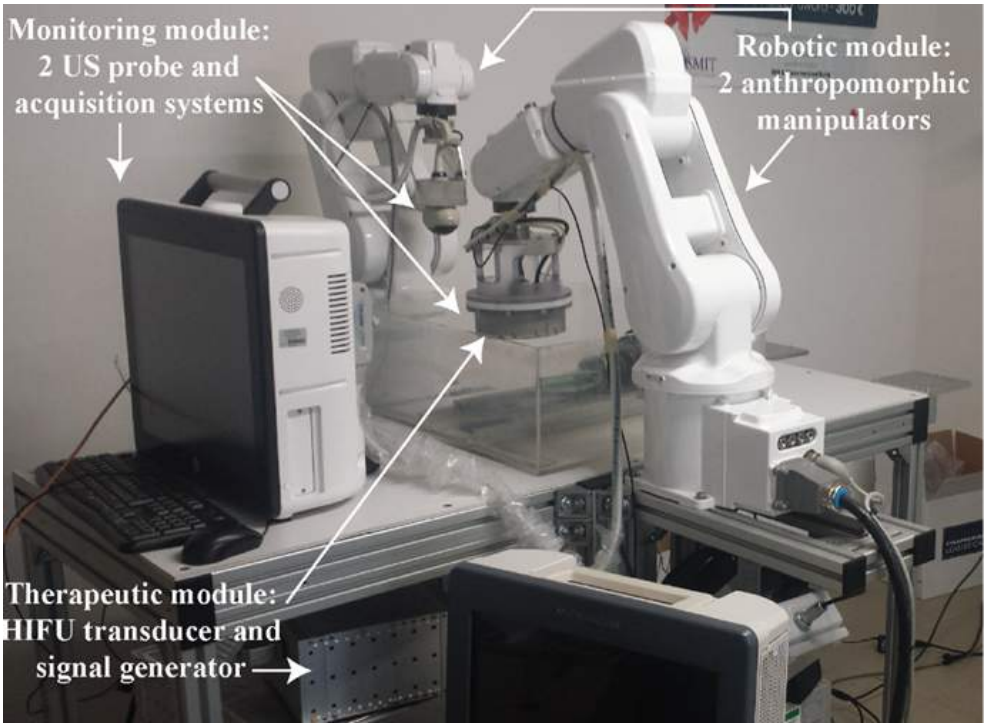


Figure 3.3: A shoot of the FUTURA platform, the different modules composing the platform are highlighted in the picture. From [DCS+17]

- **The monitoring module** is composed by two different US probes: i) a 2D imaging US probe (Analogic Ultrasound[6] PA7-4/12, MA, USA) confocal to the HIFU transducer and mounted on the first robotic manipulator, and ii) a motorized 3D imaging US probe (Analogic Ultrasound[6] 4DC7-3/40) mounted on the second manipulator, both connected to two different ultrasound machines for continuous targeting of the organ and therapy monitoring.

  It is worth mentioning that the 3D US probe is used to acquire a 3D volume only during the preoperative phase of the HIFU therapy and not during the treatment, when it is used as a standard 2D US probe for motion tracking purposes. This probe uses an electric motor to scan the body area; consequentially, the volume acquisition and reconstruction rate is about 0.1 volume per second, which is insufficient to track the physiological respiratory motion of organs (see Section 2.3.3 for details about mechanical 3D US probes).

- **The therapeutic module** consists of a custom-made HIFU system. This system has three main components: i) a multi-channel high power signal generator (Image Guided Therapy[7],

[6] www.analogic.com
[7] www.imageguidedtherapy.com

Pessac, France), ii) a 16 channels phased annular array transducer (by Imasonic[8] Voray-sur-l'Ognon, France), and iii) a coupling system (small pillow filled with water) which provides a good acoustic path between the HIFU transducer and the patient.

The 16 channels HIFU generator driven in phased array (i.e. 20 W of RF power per channel) allows to steer the HIFU focus along the central axis of the transducer. The remote control on the HIFU generator allows adjusting the shooting parameters (e.g., focal depth) with a frequency of 20 Hz.

The coupling system guarantees the acoustic path between the transducer and the patient, and it is realized by a flexible membrane (150 μm latex membrane) connected to the HIFU transducer and filled with degassed water.

To avoid excessive heating of the transducer and patient's skin, a continuous water flow of degassed water is obtained by using a dedicated closed circuit system composed of a pump that guarantees a flow of 50 ml/min and a filter (MiniModule membrane Contactors, Liqui-Cel[9], NC, USA) for the degassing process. The distention of the membrane is directly proportional to the water pressure, which is controlled by the circulation system.

By exploiting the inflation and deflation process of the flexible membrane and considering the intrinsic features of the transducer (focal length of 120 mm and axial electronic steering of $\pm$40 mm around the natural focus), the FUTURA platform can deliver the therapy in a range of distance from 10 to 130 mm from the patient's skin, suitable for human anatomy [AT16].

The different modules of the FUTURA platform are mutually controlled through a dedicated software developed in the Robot Operating System (ROS)[10] framework [QCG+09].

The HIFU treatment is managed through a navigation system with real-time visualization of the working scenario.

### 3.3.1 Navigation System Design

Information coming from a number of different tools are needed in the described platform to enable the complete monitoring of the ongoing procedure.

The confocal US probe, the 3D motorized probe and the HIFU transducer have been integrated in an ad-hoc developed navigation system, so that all of the monitoring and delivery functionalities can be made available on a single Human Machine Interface (HMI), enhancing usability of the robotic platform as a whole.

[8] www.imasonic.com
[9] www.liquicel.com
[10] www.ros.com

When applicable, standard communication protocols were employed in the integration of the different hardware and software components of the platform, pursuing the objective of having a modular system in which new components can be efficiently integrated for future developments.

#### 3.3.1.1 US Acquisition and Remote Control

A client-server architecture is exploited between the US machine(s) and the developed navigation system in order to acquire US images remotely from multiple US machines, while controlling all of the needed parameters from the platform navigation system.

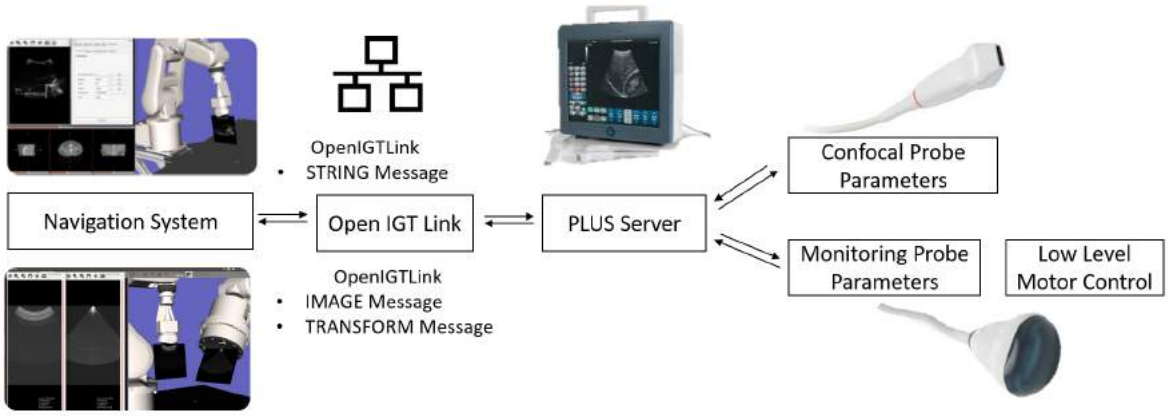


Figure 3.4: Remote US Acquisition and Control, scheme of the communication pipeline.

The server-side software, which runs on the US machine(s), is based on a customized version of the Public software Library for US imaging research (PLUS) library server module, which is an open-source C++ software package for tracked ultrasound image acquisition, calibration, and processing [LHR+14].

The server-side software internally employs the Ultrasonix[11] Porta Application Programming Interface (API), which comes with the research package of the employed US machine, providing full control over the imaging parameters of the US probe.

Through this API, it is possible to provide the collected images with the spatial information needed to map points from the image space to the physical space of the transducer, which is calibrated with respect to the robotic platform.

The navigation system acts as a client, and is capable of receiving data from, and sending data to, multiple servers on the network (Figure 3.5).

[11] https://bkultrasound.com

The images, the spatial information, and the commands are transmitted between the client(s) and the server(s) through an high-speed Ethernet connection using the OpenIGTLink protocol [TFP+09] [ETC+12], which is the de-facto standard in the development of IGS applications.

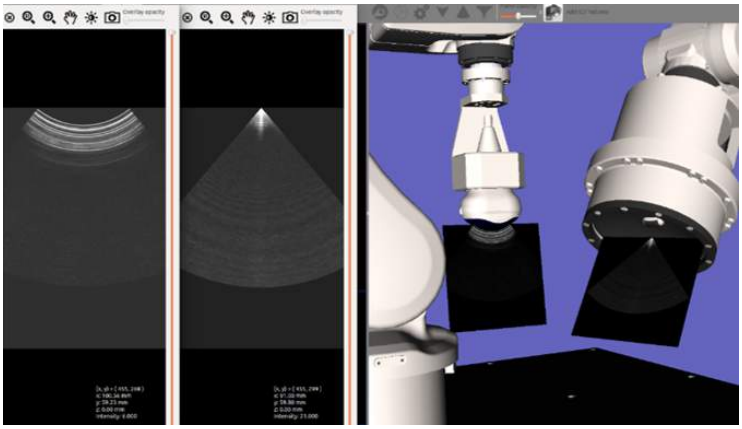

Figure 3.5: Simultaneous acquisition from two different US probes, screenshot of the developed interface.

#### 3.3.1.2 Motorized 3D US Probe Remote Control

A software module has been developed and implemented in the navigation system in order to control the motorized probe and to reconstruct the 3D volumes from B-mode US images acquired during the continuous movement of the probe transducer. This module is integrated in the same client-server architecture described above.

Through the Ultrasonix Porta API, a number of parameters related to the control of motorized probes can be set, in particular:

- FPV: frame per volume, number of frame to be acquired on a complete motor run
- SPF: step per frame, number of motor steps that separates each frame
- FOV: field of view in degrees to be covered on a complete motor run

Thanks to the aforementioned software module, which sends commands to the server-side application running on the US machine though OpenIGTLink (as described above), the navigation system can remotely set these parameters, and start the 3D acquisition process (i.e. activation of the 3D probe motor) at any time.

When a 3D US volume is requested by the client-side software during the motor movement, images acquired from the machines are recorded and interpolated with respect to the motor

position in which they were acquired, in order to reconstruct a complete 3D US volume of the region of interest. Such a volume is then sent to the navigation system, together with its spatial information though a dedicated OpenIGTLink message.

Whenever a volume is received by the navigation system:

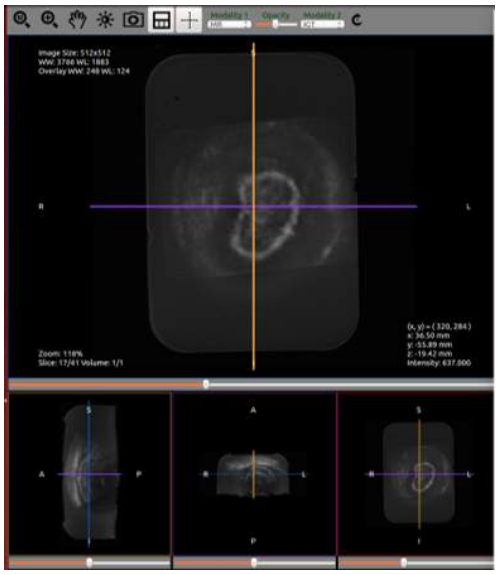

Figure 3.6: Visualization of a reconstructed US US volume (with MRI as overlay).

- The 3D US volume is referenced with respect to the robot frame of reference, taking in consideration the current robot configuration read from a dedicated ROS topic.
- The 3D US volume is added to the available data that can be explored through dedicated visualization tools (Section 3.3.1.4).

Different 3D volumes acquired during the procedure can be compared in the navigation system in order to monitor the advancement of the therapy.

#### 3.3.1.3 HIFU Integration

A software module has been developed and implemented in the navigation system in order to enable full control of the HIFU system employed in the FUTURA platform.

Such a module is composed by a graphical control panel integrated in the navigation system and a ROS node that employs the proprietary HIFU transucer API to control it via Ethernet connection.

All of the parameters of the HIFU transducer can be controlled and read including single sonication settings (i.e. steering, amplitude, frequency) and general sonication strategy parameters (i.e. number of execution, duration, interval).

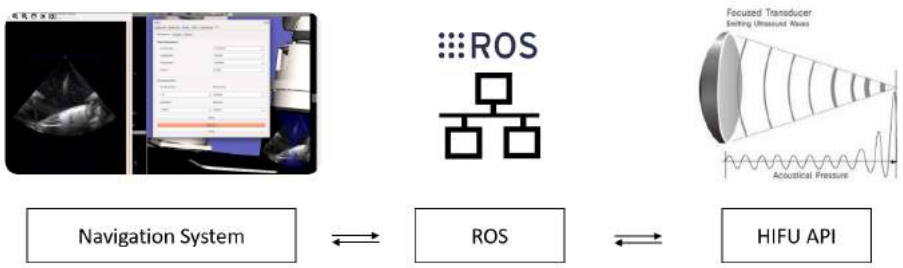


Figure 3.7: HIFU integration, communication pipeline.

In this way, it is possible for the navigation system to provide automatic HIFU focus position visualization on the US images, taking in consideration the current steering setting of the HIFU transducer. Moreover, whenever a sonication is executed, the navigation system receives from the dedicated ROS node the output parameters of the 16 channels of the HIFU transducers, in order to monitor the generated and the reflected power.

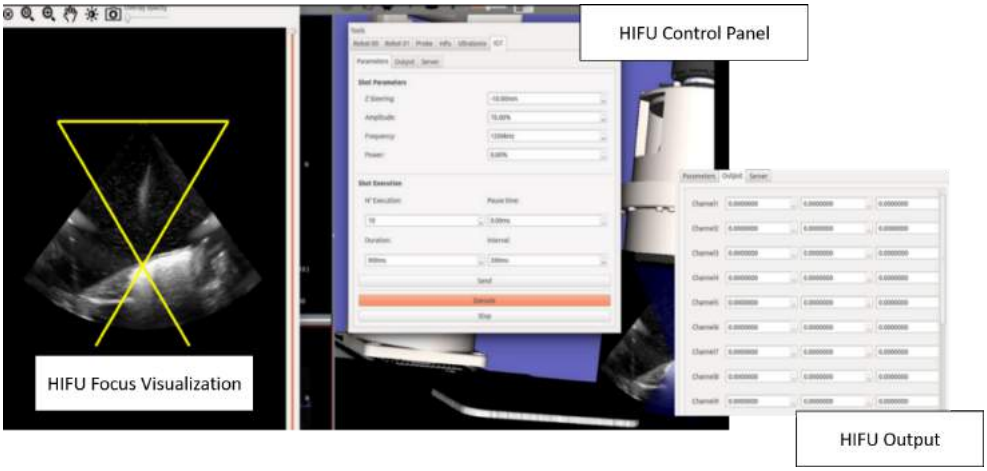


Figure 3.8: HIFU integration in the developed navigation system interface.

#### 3.3.1.4 Intraoperative Data Visualization and Fusion

The navigation system is provided with multiple graphical panels dedicated to the straight-forward visualization of the different types of data that can be acquired.

An interactive 3D scene integrates all of the information coming from (a) the robotic arms, (b) the monitoring US probe, (c) the confocal US probe, (d) the HIFU transducer and (e) the preoperative datasets.

The 3D scene, which is implemented by the means of the Visualization ToolKit (VTK) library, is composed by:

- The robotic arms in their current position, updated continuously (i.e. the update frequency is set to 60 Hz in the current implementation) thanks to the integration of the robotic platform in the ROS framework
- The updated preoperative datasets with respect to the registered patient position and their segmentation generated in the planning stage.
- The real-time US images in their calibrated 3D position and orientation in the robot space
- The 3D US volumes acquired during the procedure
- 3D indicators showing the updated position of the HIFU focus in the robot space

The 3D scene represents a valuable control panel for the clinician, helping in the monitoring process by providing in one view all of the information needed to understand what is going on in the OR.

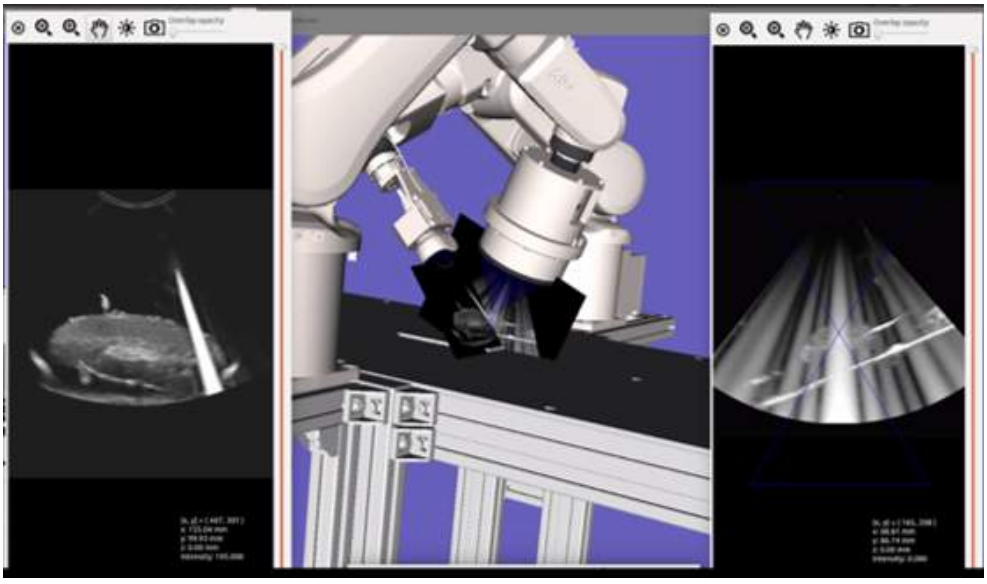

Figure 3.9: Image navigation and robot visualization in the developed interactive 3D scene.

The navigation system is also provided with other 2D visualization panels, that can be shown either next to the interactive 3D scene or in different dedicated screens (Figure 3.9, on the sides).

Those visualization panel can show

- The last image acquired by the US probes.
- A reformatted view of a selected preoperative volume in the direction and position of the current/last image acquired by the US probes, optionally blended with the corresponding real time B-mode US images

Additionally, a typical Multiplanar Reconstruction (MPR) visualization, is always available to enable better inspection of preoperative and intraoperative 3D data (Figure 3.6).

## 3.4 A Novel Motion Compensation Strategy for HIFU Therapy

Among the problems that have to be faced when designing and developing an USgHIFU platform for abdominal tumors treatment, one of the major challenge is accurately compensating for continuous physiological respiratory motion of organs; in this regard, the most critical organs are the one located in the abdominal area.

Indeed, if not correctly compensated, the organ motion can lead to a spreading of the thermal dose which is the cause of two main problems: i) loss of treatment efficiency, and ii) generation of not planned lesions on adjacent healthy tissues [OPS12].

As depicted in Figure 3.10, the problem of organ motion can be faced mainly with two different approaches: i) motion suppression techniques, or ii) motion tracking techniques. Motion suppression techniques induce temporary respiratory depression by controlling patient's breathing (e.g., use of external mechanical ventilators) in order to perform multiple sonications on the same target area as in static conditions [MPA+13].

These techniques, more largely studied and more similar to what is already common in clinical practice [MPA+13], are currently the only ones approved in clinics for hepatic [JCJH11], pancreatic [JCJH11] and renal [RLP+10] cancer HIFU treatment. However, the motion suppression methods are generally more invasive and time consuming with respect to organ motion tracking solutions [Mur04], which in theory should allow to continuously treat the target area during normal breathing.

This is of particular importance in the case of highly perfused tissues, such as liver and kidney [KTL+08], because the blood perfusion removes heat from the treated area; therefore, more time

is required for performing the therapy. For these reasons, researchers are currently investigating respiratory motion compensation techniques during procedures by estimating the motion trajectory thanks to magnetic resonance-based tracking strategies [DSMM07][STdS+16] or ultrasound-based ones [APV+12][KFS+14][DLBK+15], and by combining image processing with different technologies, such as robotics and machine learning.

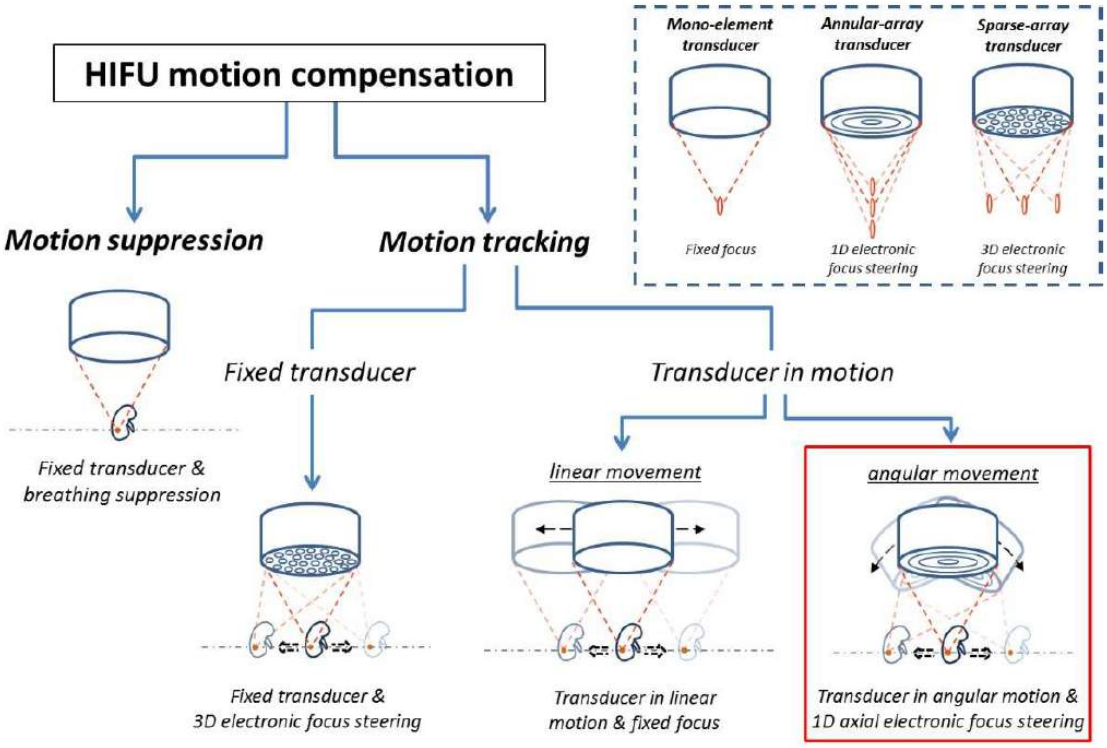


Figure 3.10: The scheme of the most common motion compensation strategies in HIFU therapy. From [DCS+17].

Figure 3.10 schematizes the common motion compensation methodologies reported in literature. These methods are performed by moving or by keeping steady the HIFU transducer. The latter approach (i.e., motion tracking with fixed HIFU transducer position) requires complex multi-elements phased array transducers capable to electronically steer the focal point in the 3D space.

Indeed, the electronic steering of the focal point compensates the target area motion, while the transducer is stably maintained in a fixed position. In [HGS+14] a dedicated system for HIFU liver ablation by using a 1000 elements phased array transducer (ExAblate, Insightec[12], Israel) was presented. Accuracy results are similar with those obtained with breath-holding techniques.

On the other hand, multi-elements array HIFU transducers with electronic steering are quite

[12] www.insightec.com

sophisticated, due to the high number of emitter elements. This drastically raises the complexity and the costs of the transducer and the driving electronics, thus being a limit when costs and clinical flexibility are relevant issues.

In the proposed framework, the technological limitations of the modern multi-elements phased transducers can be circumvented employing single element (fixed focal point) or annular array transducers (able to steer the focal point along the central axis, [GCM$^+$93]) and compensating the motion of the target area by moving the transducer.

A non-invasive ultrasound diagnostic system that compensates organs motion was described in [KFS$^+$14] and[KFS$^+$15]. This system is able to track and follow the area to be treated using stereo US imaging while irradiating the target area with HIFU. An all-in-one robotized HIFU system was developed in [CNV$^+$15] for real-time intra-abdominal organ motion compensation by exploiting a US visual servoing scheme. A visual US based servoing system was also developed in [SKMS17] for sonicating moving targets.

All the reported works successfully compensate a simulated 1D organ motion with a linear movement of the HIFU transducer, which is the simplest way to compensate the motion at the target point. However, this approach could limit the range of imaging and treatment: the continuous modification of the acoustic window could hamper the correct identification and treatment of the target (e.g., due to the presence of the ribs/bones in the path of the HIFU beam) [SKMS17], thus decreasing the number of possible applications in clinics.

A Robotic-assisted approach can be exploited to develop new strategies that overcome the problems and limitations mentioned above. The peculiarity of the FUTURA platform's architecture, described in Section 3.3 is that the HIFU transducer – attached to an anthropomorphic manipulator – can be positioned in direct contact with the patient from above, thus reversing the common architecture of traditional HIFU systems (e.g., HAIFU, Chongqing Haifu Medical Technology Co. Ltd, Chongqing[13], China) in which the therapeutic transducer is located below the patient's bed.

Below, a module for tracking and detection of a target regions is proposed, that enables efficient treatment with HIFU by exploiting an angular tracking approach (i.e. Pivot Motion Compensation (PMC)), thus avoiding the above-mentioned limitations of motion tracking techniques using 3D electronic steering and strategies based on a linear movement of the transducer.

Briefly, the proposed PMC method consists in:

1. maintaining approximately the same contact point between the transducer acoustic coupling system and the patient's skin by means of a force control implemented on the robotic arm,
2. adjusting the orientation of the HIFU transducer (i.e. pivot motion compensation),
3. continuously regulating the focal depth thanks to the axial steering capabilities of an annular

[13] www.haifumedical.com

array HIFU transducer.

The next subsections describe:

- the Pivot Motion Compensation strategy
- the image based guidance system that has been designed and developed in order to apply the PMC strategy to the FUTURA platform.

### 3.4.1 Pivot Motion Compensation Strategy

In order to effectively compensate the motion of the target area and efficiently delivery the ultrasound energy without harming the patient, it is necessary to:

- Accurately place the HIFU focal spot for the whole duration of the sonication;
- Monitor and control the forces generated by the transducer on the patient;
- Ensure a good acoustic path between the transducer and the target area.

During the preoperative phase, the physician chooses an acoustic window according to the anatomy of the patient. To ensure a good acoustic path during the treatment, the pre-planned acoustic window should be preserved by the motion compensation method. Therefore, the contact area between the skin of the patient and the transducer acoustic coupling system should not significantly change during the procedure.

To maintain approximately the same contact area, we take advantage of the pivot point concept: the transducer rotates around the position of the manipulator end-effector ($\vec{EE}$) for compensating the motion of the target area. This would be not sufficient to preserve the acoustic path, because a contact area must be guaranteed and not only a single contact point. However, the use of a pillow filled with degassed water as coupling system mitigates this constraint. The contact area between the patient's skin and the transducer acoustic coupling system is increased by pushing the transducer against the patient with a controlled force.

Figure 3.11 illustrates notable points, forces, and versors involved in the developed PMC strategy when the HIFU transducer is in contact with the patient. The $\vec{z_E}$ axis corresponds to the central axis of the transducer along which it is possible to steer the position of the focal spot $\vec{S}$. The position of the focal spot $\vec{S}$ is defined in eq. (3.1).

$$\vec{S} = \vec{EE} - (d_f + s)\vec{z_E} \tag{3.1}$$

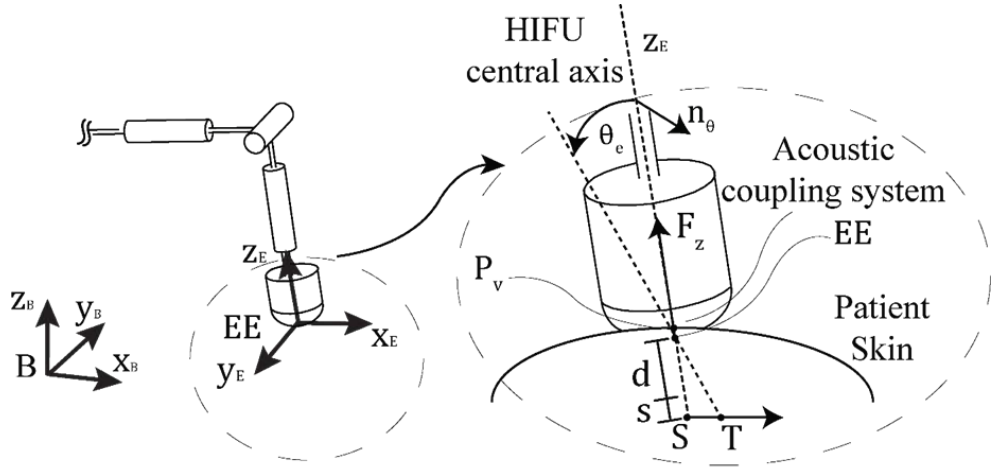


Figure 3.11: The scheme of the proposed PMC method. From [DCS+17].

where $\vec{EE}$ is the position of the manipulator end-effector, $d_f$ is the distance between the $\vec{EE}$ and the geometric focal spot of the transducer and $s$ is the electronic steering of the focus from its natural position.

The focal spot $\vec{S}$ is always along the $\vec{z_E}$ axis, and therefore, to sonicate the correct target point $\vec{T}$, the central axis of the HIFU transducer must be aligned with the straight line passing through the $\vec{EE}$ and the target $\vec{T}$. This alignment is accomplished through angular movement of the transducer around the manipulator $\vec{EE}$.

Namely, the transducer is rotated by the angle error $\theta_e$ (defined in eq. (3.2)) along the direction $\vec{n_\theta}$ (defined in eq. (3.3)), which is perpendicular to the straight line passing through the $\vec{EE}$ and $\vec{T}$ and $\vec{z_E}$.

$$\theta_e = cos^{-1}(\vec{z_E}^T(\vec{T} - \vec{EE}))/\| \vec{T} - \vec{EE} \|) \tag{3.2}$$

$$\vec{n_\theta} = (\vec{z_E} \times (\vec{T} - \vec{EE}))/\| \vec{T} - \vec{EE} \|) \tag{3.3}$$

In order to place the focal spot $\vec{S}$ in the correct target $\vec{T}$, we also need to compensate the distance between $\vec{EE}$ and $\vec{T}$ that continuously changes during the treatment. This is done by adjusting the focal depth accordingly by minimizing the distance $s$ between the focal spot $\vec{S}$ and the target $\vec{T}$ (defined in eq. (3.4)).

$$s = \vec{z_E}^T(\vec{T} - \vec{EE}) - d_f \tag{3.4}$$

Besides positioning the HIFU focal spot, we need to preserve the contact area between the

transducer acoustic coupling system and the patient's skin in the planned acoustic window. To achieve this, the HIFU transducer is pushed against the patient with supervised and controlled force that must be always under certain threshold [BKK+16]. The contact force can be decomposed in three forces $F_x$, $F_y$ and $F_z$ along the three axes $\vec{x_e}$, $\vec{y_e}$ and $\vec{z_e}$.

The force $F_z$ is used to maintain the contact area between the patient's skin and the acoustic coupling system, the physician can tune the reference value of this force $F_z^r$ in the preoperative phase. The physician also selects the acoustic window setting a reference point for $\vec{EE}$; this reference is called "virtual pivot point" $\vec{P_v}$.

However, the $\vec{EE}$ cannot be just placed at the virtual pivot point $\vec{P_v}$ because the movements of the patient can generate large values of forces along $\vec{x_e}$ and $\vec{y_e}$. These forces must be monitored together with the force $F_z$ to ensure patient safety; additionally, $\vec{EE}$ must be kept close to $\vec{P_v}$ for preserving the planned acoustic window. To do this, a virtual spring between $\vec{P_v}$ and $\vec{EE}$ is designed to generate resistance force along $\vec{x_e}$ and $\vec{y_e}$.

The virtual spring has a configurable stiffness $K_f$ that regulates the forces amplitude applied to the patient; higher value of this parameter determines higher values of resistance forces. Equation (3.5) defines the reference values of these resistance forces $F_x^r$ and $F_y^r$. The use of virtual springs to improve the contact between patient's skin and ultrasound probe has been already exploited in the state of art [SBI+13] [FZF+17].

$$\begin{bmatrix} F_x^r \\ F_Y^r \end{bmatrix} = K_f \begin{bmatrix} \vec{x_E}^T \\ \vec{y_E}^T \end{bmatrix} (\vec{P_v} - \vec{EE}) \tag{3.5}$$

### 3.4.2 Tracking and Learning Respiratory Motion

A novel US based guidance pipeline has been designed and developed by the author, that uses computer vision and machine learning techniques to actively track and predict the periodic motion of a target area, thus enabling the robotic arms to continuously compensate it during HIFU treatment, even when the B-mode US images are corrupted by interferences [VSM+01] caused by the HIFU transducer .

The integration of such a pipeline in the developed navigation system of the FUTURA platform has been carried out in order to automate the guidance of the robotic platform, and to provide advanced navigation capabilities.

The pipeline is composed of three modules:

- a tracking module that detects and tracks a Region of Interest (ROI) on B-mode US images
- a trajectory prediction module capable of anticipating the target trajectory by exploiting machine learning to model on previous observations provided by the tracking module

- a safety module that stops the HIFU sonication when the detected error between the current tracked target position and the predicted target position is larger than a user-defined threshold (depending on the error margin that is considered acceptable according to the therapy plan).

The combination of tracking and learning the target trajectory is needed to:

- compensate for delays in the US acquisition and elaboration chain,
- keep the target in the desired position with respect to the HIFU focal spot while the therapy is ongoing and the B-mode US images are corrupted by the HIFU-generated reflections.

In the following subsections, all of the steps needed in order to realize efficient and effective guidance will be presented.

#### 3.4.2.1 Ultrasound Probe Calibration

As a preliminary step, in order to minimize the systematic error that occurs when selecting and/or tracking anatomical landmarks on ultrasound images provided by any US probe, it is necessary to perform an accurate calibration of the US probes with respect to its reference system, in this case, with respect to the robotic platform.

Calibration was performed using the well known PLUS library[LHR+14]. PLUS library provides a calibration software platform that includes a suite of tools and algorithms for temporal and spatial calibration of an US probe with respect to an external sensor. Moreover, the project for a 3D-printable calibration phantom is is available in the PLUS documentation.

The main steps involved in the calibration process are:

- Calibration of an optical pointer (i.e. in our case, the NDI[14]Polaris pointer)
- Localization of the calibration phantom via selection of a set of known points on the phantom, using the previously calibrated optical pointer.
- Automatic identification of known features of the calibration phantom on the US images while moving the US probe in different poses (which are known thanks to the optical markers fixed to the robotic arm holding the probe)

Exploiting an optical sensor attached on the robotic arm and a 3D-printed calibration phantom (Figure 3.12) it was possible to estimate the transforms between the coordinate system of the US image and the coordinate system of the optical sensor.

[14]www.ndigital.com

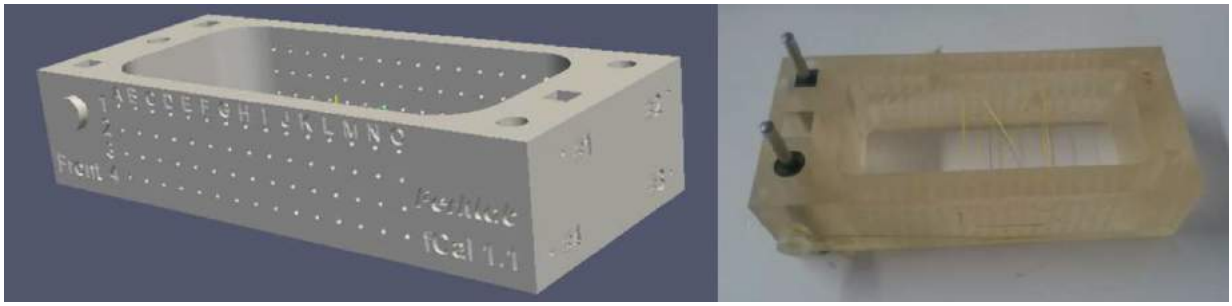

Figure 3.12: 3D rendering and digital photo of the employed calibration phantom.

| | 2D US Confocal Probe | 3D US Monitoring Probe |
|---|---|---|
| Pointer Calibration | 0.16 mm | 0.16 mm |
| Phantom Calibration | 0.25 mm | 0.25 mm |
| Image Calibration | $0.76 \pm 0.46$ mm | $0.64 \pm 0.28$ mm |

Table 3.1: Calibration errors

Thanks to the known rigid transform between the optical sensors and the end-effector of the calibrated robotic platform, spatial information of the US image can be referred to the robot space simply by solving the cinematic chain of the robot.

Errors for each calibration step are resumed in Table 3.1.

#### 3.4.2.2 Target Tracking

The developed HMI of the FUTURA platform requires the user to manually select a target ROI on B-mode US images, which is employed to initialize a tracking algorithm. The ROI is updated whenever a new frame is acquired and the position of the ROI center is forwarded to the trajectory prediction module.

The ROI tracking functionality is based on the well known framework for long-term tracking of unknown objects called Tracking-Learning-Detection (TLD) which was presented in [KMM12].

The TLD approach decomposes the long-term tracking task into a) tracking, b) detection, and c) learning [KMM12]. In this approach, a tracker and a detector are combined to increase robustness of the long-term tracking task and to improve its performance over time, actively learning from past mistakes and adapting to ROI appearance changes.

The three components of the TLD approach are briefly described below:

- **Tracking** The tracker relies on optical flow, and follows the forward-backward approach of

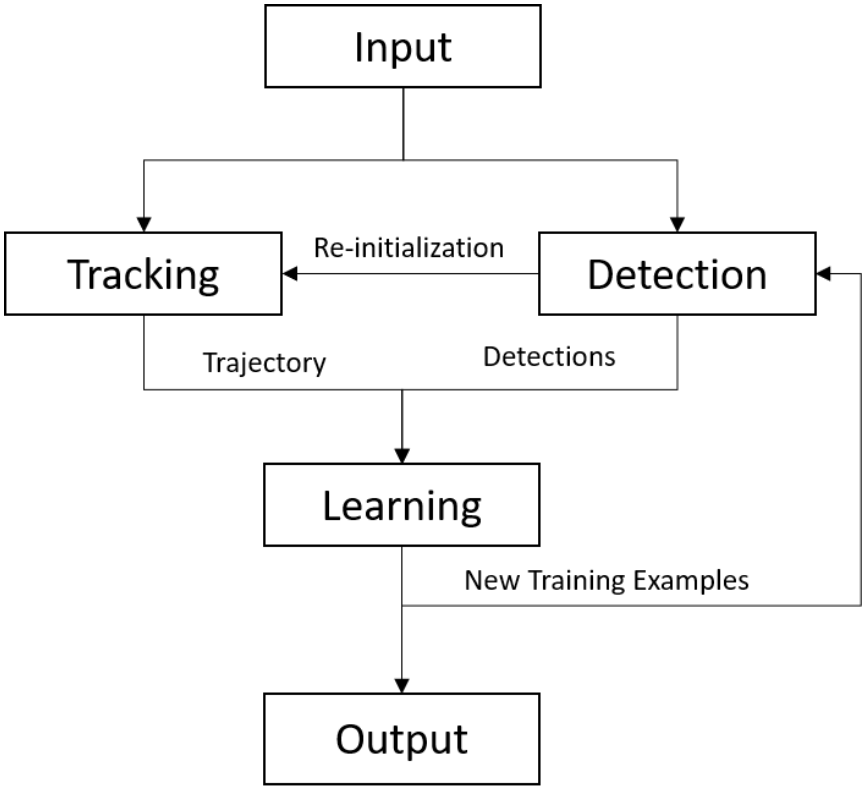


Figure 3.13: Scheme of the TLD algorithm.

[KMM10] to robustly identify motion across consecutive frames (Figure 3.14). Every time that a new frame is acquired, if motion of the ROI is identified with enough confidence, measured in terms of Normalized Cross-correlation Coefficient (NCC) between matching ROIs in consecutive frames, the position of the ROI is updated.

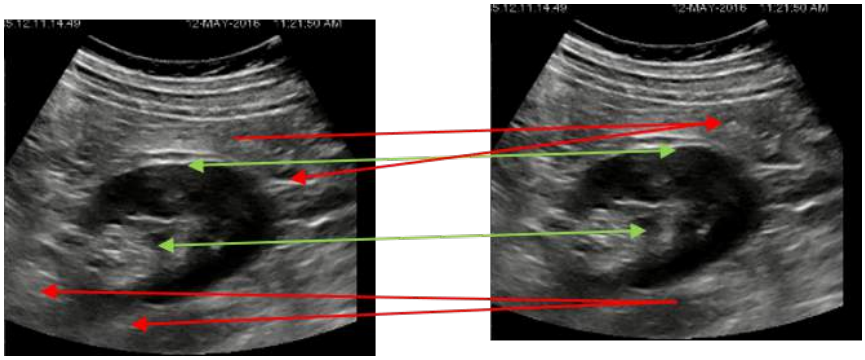

Figure 3.14: Simplified scheme of the tracking step. Motion is estimated both forward and backward in time, in order to estimate the most reliable trajectories.

- **Detection** The detector finds image patches similar to the ROI in the last acquired frame using a template matching approach. The following steps can summarize the detection procedure (Figure 3.15):

  – Image patches of the size of the ROI are extracted from the image using a sliding window approach.

  – A filtering cascade is used as a preliminary step to reduce computational time, mainly consisting of a variance filter and an ensemble classifier [OCLF10]. Thanks to this step, a number of candidate image patches are discarded.

  – The remaining patches are sorted thanks to their similarity to an appearance model consisting of a nearest-neighbor classifier which is trained on tracked patches (i.e. positive examples) and background patches (i.e. negative examples). NCC [Lew95] is employed as the main similarity metric.

    Given a reference patch $R$ a the target patch $T$ of equal size $n \times n$ ($n = 50$ in our implementation, all of the patches are resized before comparison), NCC is computed as:

$$NCC = \left(\frac{\sum_{i=1}^{n}\sum_{j=1}^{n}(T(i,j) * R(i,j))}{\sqrt{\sum_{i=1}^{n}\sum_{j=1}^{n}T(i,j)^2 * \sum_{i=1}^{n}\sum_{j=1}^{n}R(i,j)^2}} + 1\right)/2$$

    NCC is computed for the target patch and each one of the patches composing the set of positive and negative examples. Let $s_{pos}$ and $s_{neg}$ be the maximum NCC values of the target patch respectively among the positive examples set and the negative examples set. The final similarity measure is computed as:

$$s_{tot} = (1 - s_{neg})/(2 - s_{neg} - s_{pos})$$

  – The patch that results most similar to the appearance model is chosen, given that $s_{tot}$ is above a threshold $\theta_{TP}$ ($\theta_{TP} = 0.65$ in our implementation), the others are discarded.

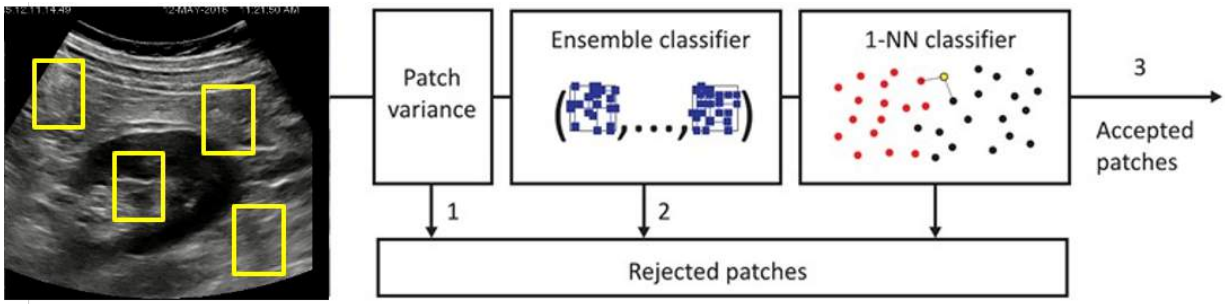


Figure 3.15: Simplified scheme of the detection step. Adapted from [KMM12]

- **Learning** The learning task combines the tracker and the detector information in order to allow:
  - the re-initialization of the tracker when the detector output has higher confidence;
  - the update of the appearance model when the tracker output has higher confidence.

  The same distance measured computed via the nearest neighbor classifier which was described above, is employed for evaluating both the detector confidence and the tracker confidence.

  When the image patch identified by the tracker has higher confidence than the detector one, the detector is updated by expanding the positive examples set of the mentioned nearest-neighbor classifier with chosen image patches from the tracker and discarded image patches from the detector (as positive and negative examples, respectively).

  A patch chosen by the tracker needs to satisfy the following constraints in order to be added to the positive examples set:

  - Its confidence has to be higher than a threshold $\theta_{FP}$ ($\theta_{FP} = 0.5$ in our implementation), in order to only enable gradual changes to the positive example set;
  - Its confidence has to be lower than the threshold $\theta_{TP}$ ($\theta_{TP} = 0.65$ in our implementation), in order to avoid that patches that are already similar to the positive examples set are added, increasing computational costs and providing no benefits.

  Similarly, a patch chosen by the detector, but then discarded, has to satisfy the following constraint in order to be added to the negative examples set:

  - Its confidence has to be higher than the threshold $\theta_{FP}$, in order to avoid the excessive growing of the negative examples set;
  - Its overlap with the chosen patch, computed as the percentage of area between the chosen patch which is covered by the discarded patch, has to be lower than a threshold $\gamma$ ($\gamma = 0.2$ in our implementation), in order to avoid adding to the negative examples set those patches which are very close to the correct result.

  As a result of this process, the detection pipeline actively learns a model of the target appearance during the tracking process, and it is capable of automatically adapting to modifications of the anatomical feature of interest.

A more accurate description of the TLD approach and its learning framework is out of the scope of this work and can be found in [KMM12].

The choice of TLD is based on the following considerations:

- It is capable of automatically recovering the tracking after temporary losing the target, as in case of out-of-plane motion which can occur in B-mode images.

  In the developed system, whenever a tracking failure occurs, the therapy is promptly stopped and it is allowed to restart only when the target is recovered and its trajectory is correctly identified and estimated (see Section 3.4.2.3 for additional details).

- Can adapt to slight changes in appearance and shape of the target area, which may be caused by the HIFU therapy and by patient movements.

- It is designed for long-term tracking, thus making it suitable for tracking a target during the entire procedure with little to no human intervention. It should be noted that the risk exists for the TLD method to gradually learn new ROI shapes and drift from the original target. While this risk can be partially mitigated by tuning the thresholds influencing the update criteria of the classifier example sets, in the designed system it is also possible to temporarily or permanently disable the learning step of the TLD method at any time during the procedure.

  Whenever HIFU shooting is activated, in particular, TLD internal model update has to be disabled, in order to avoid learning from the US images corrupted by HIFU noise. (see Section 3.4.2.3 for additional details about other automatic safety measure which are set in place during shooting).

The described tracking strategy has been integrated within the navigation system of the FUTURA platform via ROS. The employed C++ implementation is based on [Neb12] and can provide continuous tracking at 30 Hz on 600x600 B-mode US images.

#### 3.4.2.3 Trajectory Prediction

The task of the trajectory prediction module is to estimate the periodic motion of the target position provided by the tracking module. Every time the ROI is updated its position in the robotic platform reference frame is communicated to the trajectory prediction module, which stores it in a first-in/first-out buffer (the max size of the buffer is set to 300 samples in our implementation), together with its acquisition time.

The trajectory prediction task is treated as a machine learning regression problem where the position of the target is described as a function of time.

Such problem is approached by using Gaussian Process (GP) regression [WR96] which is a standard machine learning technique often used to model temporal series [ROE+13][BBB04]. One of the defining elements of a GP regression model is its covariance function, or kernel, which specifies the type of functions that can be learned by the model.

The trajectory prediction module makes assumes that induced respiratory motion can be approximated to be periodic. In order to model this kind of motion a periodic kernel is employed [RW06], suitable for learning periodic functions [CV11]:

$$k\left(x_i, x_j\right) = e^{-2\left(\sin\left(\frac{\pi}{p}\left(x_i - x_j\right)\right)/l\right)^2} \tag{3.6}$$

The periodic kernel has two parameters: a length-scale parameter $l > 0$ and a periodicity parameter $p > 0$ which are found automatically via gradient based optimization [Ben00]. An initial estimate for $p$ can be provided by the user in the developed system, on the basis of the estimated period of the respiratory motion (which can be known, as in the case of forced respiration conditions).

Observations of the target positions over time are continuously collected together with their time points, composing the set of data which is used to train a regression model for each spatial dimension (i.e. three models are employed in our implementation, for the $x$, $y$, and $z$ dimension respectively), the target positions being the target of the model and their acquisition time being the input.

Model training is triggered once a predefined number of samples $n$ is collected ($n = 250$ in our implementation, corresponding to a 10 s acquisition at 25 fps US acquisition rate, which was found to be sufficient in the experimental setting described in Section 3.4.3.2). A new model is continuously trained on background whenever an additional number of samples $k$ is collected ($k = 150$ in our implementation).

Despite the automatic model retraining capabilities, the choice was made to only update the predicted trajectory on user request (i.e. immediately picking the latest available trained model). This is especially important during HIFU shooting, since less tracking samples can be acquired due to the HIFU noise corrupting the US images, a situation that can potentially cause larger errors in the trajectory estimation. A more detailed explanation on the behavior of the system during HIFU shooting, and its interactions with the trajectory prediction module can be found in Section 3.4.2.4.

Once the trajectory of the target area is learned and accepted by the user, it is continuously provided to the therapeutic manipulator with a configurable time offset (i.e. 0.25 $s$ in our implementation) that compensates for the delay in the acquisition and elaboration of the B-mode US images.

A python implementation of GP based on the open-source scikit-learn machine learning library [15] [PVG+11] is employed in the developed module.

[15] www.scikit-learn.org

#### 3.4.2.4 Safety Shooting Strategy

During HIFU treatment the robotic platform has to be able to stop the treatment if an abrupt movement of the patient occurs, or if the tracking strategy is not confident enough in providing the identified target position.

During shooting, no valid information from the US probe can be acquired due to the strong noise that partially or entirely corrupts the image. In order to overcome this limitation an intermittent sonication strategy is employed, as depicted in Figure 3.16.

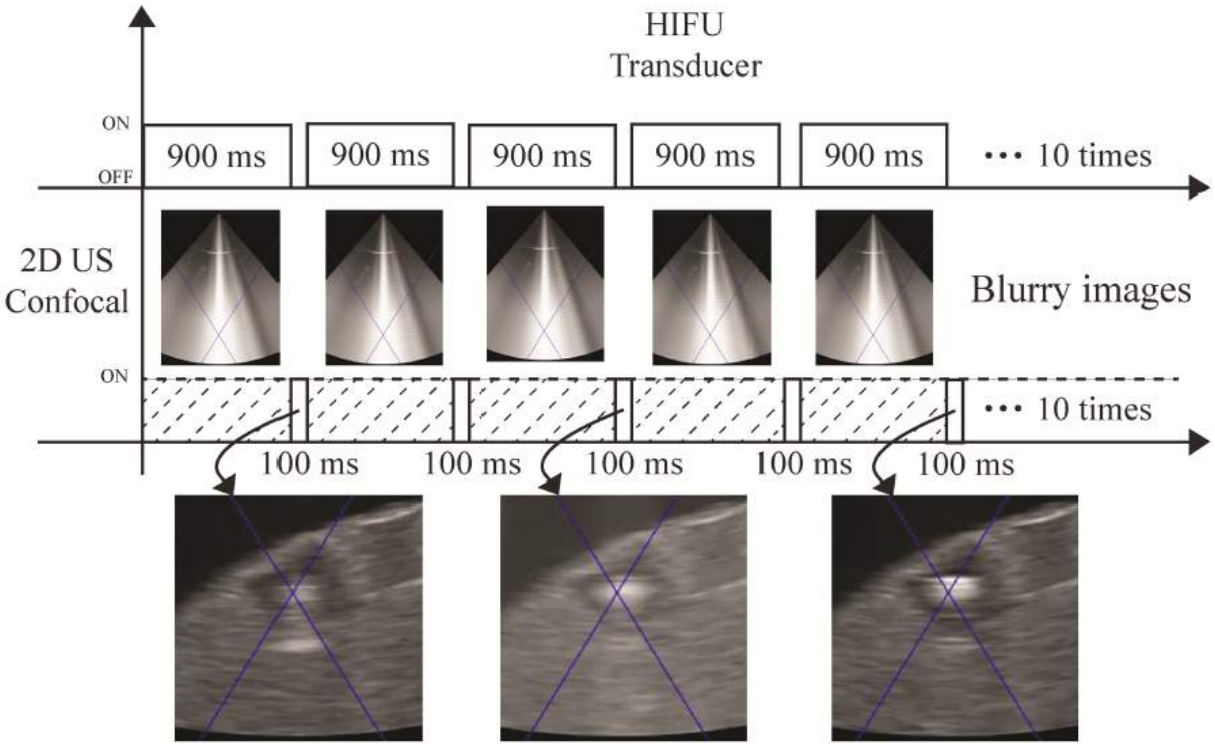


Figure 3.16: Intermittent sonication strategy scheme, the transducer is switched off for brief amount of times during the sonication, enabling the US probes to catch images which are not corrupted by noise.

This enables the confocal US probe to visualize the target when the HIFU is briefly switched off during the therapy. A safety shooting strategy enables the continuation of the HIFU sonication only if the tracking module (described above) is confident enough that the target position is in its expected position (under the HIFU focus). Such a strategy can be decomposed in the following steps:

- Target point selection: the user is required to select a region to track in the image.

- Target point periodic motion estimation: the periodic motion of the target is estimated and its accuracy is evaluated on the previously observed and tracked motion.
- Trajectory generation: the learned trajectory is generated, and forwarded to the robot, so that the observed movement is compensated and the target is actively kept under the HIFU focus.
- Error evaluation and safe shooting authorization: whenever an image is acquired from the machine, and the target point is identified by the tracking module, its position is compared to its currently predicted trajectory, and the authorization to shoot is given to the HIFU only if the computed error is below a configurable threshold $t$ ($t = 1.25mm$ in our implementation). Otherwise, the sonication is stopped, and an updated estimation of the trajectory is requested to the learning module.

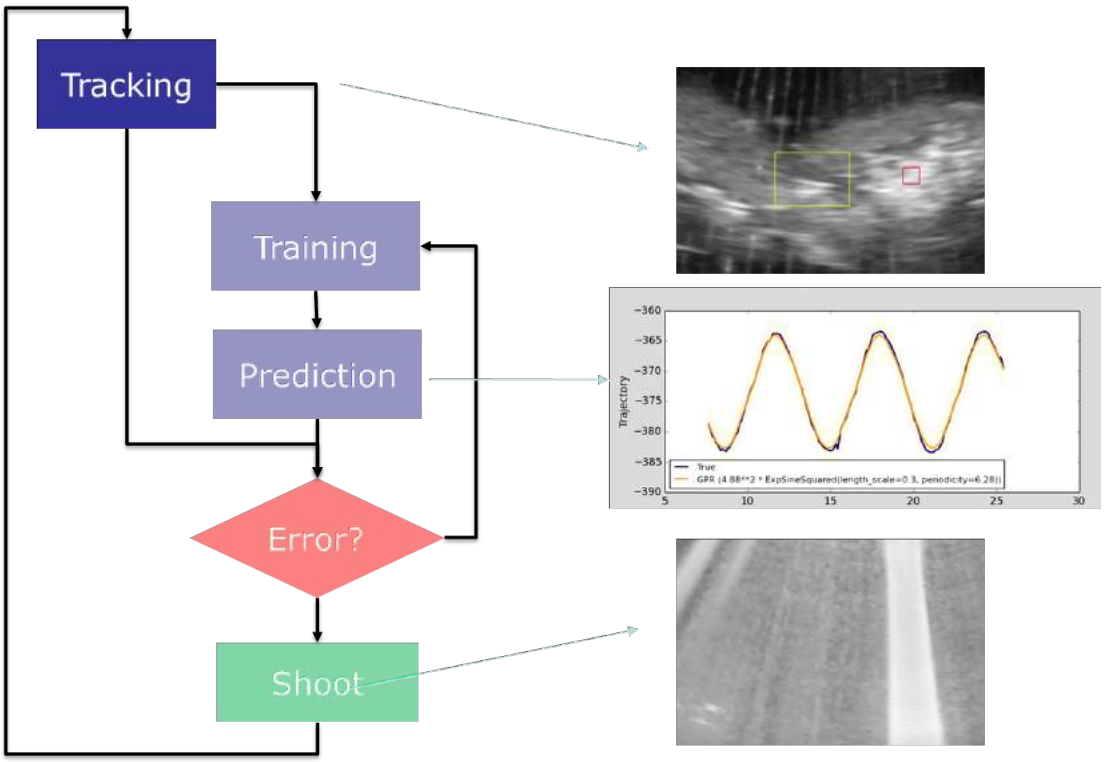


Figure 3.17: Scheme of the developed safety shooting strategy.

To evaluate this error, clear US images (without HIFU sonication) must be acquired and processed, thus requiring a time lag between consecutive HIFU sonication. The time needed to acquire a clear US image and evaluate the error between the tracked and the predicted target was estimated to be $0.07 \pm 0.04$ $s$ with a maximum value of $0.17$ $s$ that is the maximum time between two consecutive HIFU sonication in the employed strategy.

Thanks to this procedure, if the target is lost due to a non-predicted patient movement, the therapy is not allowed to continue and no damage is dealt to the patient.

### 3.4.3 Results

In order to evaluate the performance of the described pipeline applied to the PMC strategy described in section Section 3.4, several tests have been carried out in a dedicated experimental setup.

In these tests the presented PMC method was also compared to a simpler linear compensation method (see Figure 3.10 for a schematic representation of the linear compensation method), in which the HIFU focus is fixed and the HIFU transducer is always parallel to the employed motorized slide. In this setting the robot end-effector is only translated along the 1D target motion direction. Linear motion compensation method is employed in relevant works [SKMS17] which are the current state of the art in terms of accuracy, but it is not well suited for clinical application, since it requires continuous modification of the acoustic window and it usually requires a tank completely filled with degassed water (i.e. the target has to be submerged to provide constant acoustic coupling while moving the HIFU transducer).

#### 3.4.3.1 Experimental Procedure

The dedicated experimental setup (Figure 3.18) consists of an ex-vivo porcine kidney placed on a 1 degree of freedom motorized slide used to simulate breathing motion. A mechanical structure with a 20 μm polyester membrane was used to mimic the abdominal wall (in the following, this membrane is called abdomen simulator), thus allowing the simulation of the contact force with the HIFU transducer.

The pillow is filled with degassed water, which is also present into the tank in order to guarantee constant acoustic coupling with the ex-vivo organ and for reproducing a realistic in-vivo condition. The second manipulator of the robotic platform is kept stable during the entire test and it is used to track the target area, whereas the first manipulator is moved following the PMC method.

The choice was made to simulate the tissue motion as 1 degree of freedom as a trade-off between the complexity of the experimental setup and the simulation fidelity of the kidney breathing motion (movement in the cranio-caudal axis [SPM84]). It is worth mentioning that even if the accuracy of the method was assessed in a 1D simulated breathing-like motion, neither the proposed motion compensation strategy not the developed trajectory learning pipeline assume 1 degree of freedom motion.

The experimental procedure started with the manual selection of a target area on the ex-vivo porcine kidney from the US images. Then, the motorized slide was activated and it started to

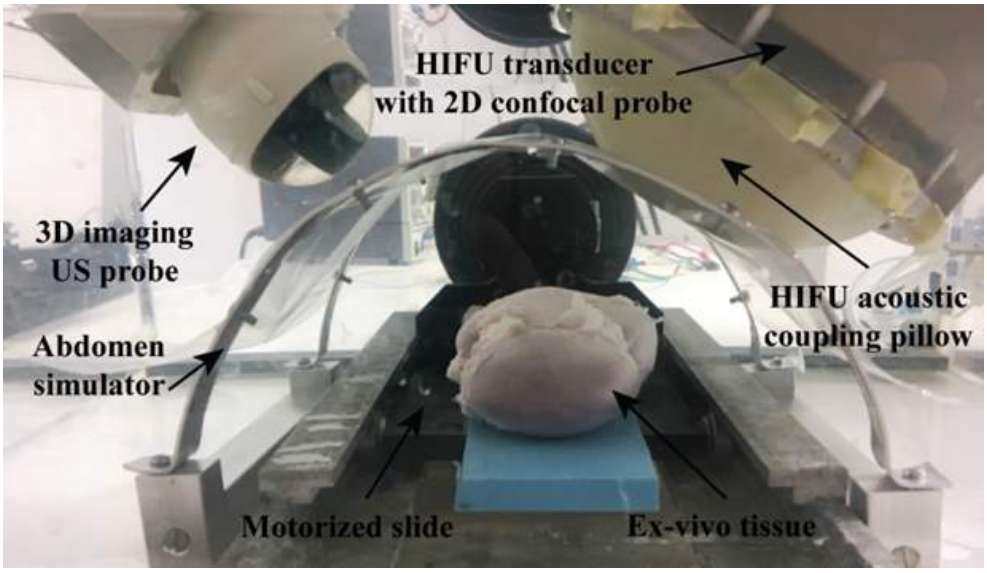


Figure 3.18: The proposed experimental setup, an ex-vivo porcine kidney is moved by a 1 degree of freedom motorized slide. The setup is immersed in a tank filled with degassed water. From [DCS+17]

perform a breathing-like sinusoidal motion with an amplitude of 20 mm and a frequency of 0.2 Hz (i.e. 12 breaths per minute).

At this point, the tracking and learning modules were activated. When the trajectory of the target area was learned (maximum error between the tracked and learned trajectories under 1 mm), the therapeutic manipulator started to compensate the motion according to the designed motion compensation method. The duration of the motion compensation was set to 20 seconds. This procedure was performed 10 times on randomly selected kidney target areas.

All the data were recorded to calculate the error vector between the target point and the nominal HIFU focal spot, and to evaluate the interaction forces between the abdomen simulator and the pillow. The target point is calculated adding at the initial target point position (measured through an ultrasound probe) the slide displacement (provided by the slide encoder) along the slide direction (measured through an active optical sensor). The nominal HIFU focal spot was computed through eq. (3.1) where $\vec{EE}$ and $\vec{z_E}$ are manipulator measurements (exploiting the direct kinematics and encoders), and $d_f$ and $s$ are known parameters of the HIFU transducer.

The target point is calculated adding at the initial target point position (measured through an ultrasound probe) the slide displacement (provided by the slide encoder) along the slide direction (measured through an active optical sensor).

The force applied at the manipulator end effector is regulated using the integrated control force assembly on the IRB 120. The value of the force reference $F_z^r$ was set to 8 N. This force amplitude

guarantees the contact between the abdomen simulator and the pillow without damaging the abdominal simulator and it is a reasonable value for in-vivo application [BKK+16]. The stiffness of the virtual spring $K_f$ was set to 2 N/mm.

#### 3.4.3.2 Motion Compensation Assessment

The accuracy of the proposed angular tracking strategy and its image based guidance pipeline was quantitatively assessed by computing the error between the target point and the nominal HIFU focal spot(i.e. compensation error) and qualitatively evaluated by checking the position, the size and the geometry of the performed lesions on ex-vivo tissues.

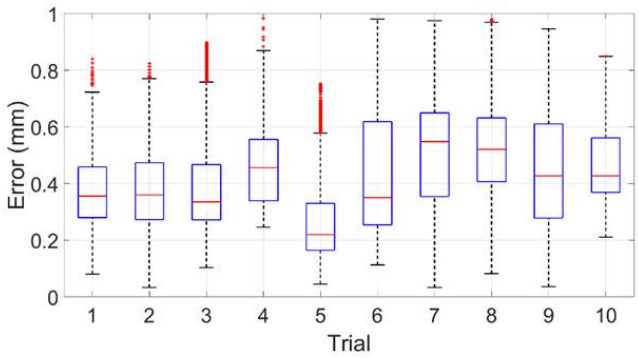


Figure 3.19: Box–and-whisker plot of the compensation error obtained using the PMC method. From [DCS+17]

The experimental results of the PMC method are reported by box-and-whisker plot (Figure 3.19) where the points outside the box are outliers and the ends of the whiskers indicate the maximum and the minimum of the compensation error. It can be observed that the compensation error is always less than 1 mm for each trial.

Figure 3.20 reports the compensation errors expressed in the manipulator base reference system (Figure 3.20-a) and the forces measured by the force sensor (Figure 3.20-b) during a single experimental test conducted using the PMC method.

At the beginning of the experiment (i.e. $t = 0$) the manipulator is not in contact with the abdomen simulator, the three forces are close to zero and the error between the nominal focal spot and the target area is large (Figure 3.20-a).

Then, the motion compensation kicks in and the error norm decreases while the forces become significant (i.e. the contact with the abdomen simulator was established). During the transient phase, $F_z$ increases achieving its reference value (8 N), thus ensuring a correct acoustic coupling between the pillow and the abdominal simulator. The forces along $x_E$ and $y_E$ keep the HIFU

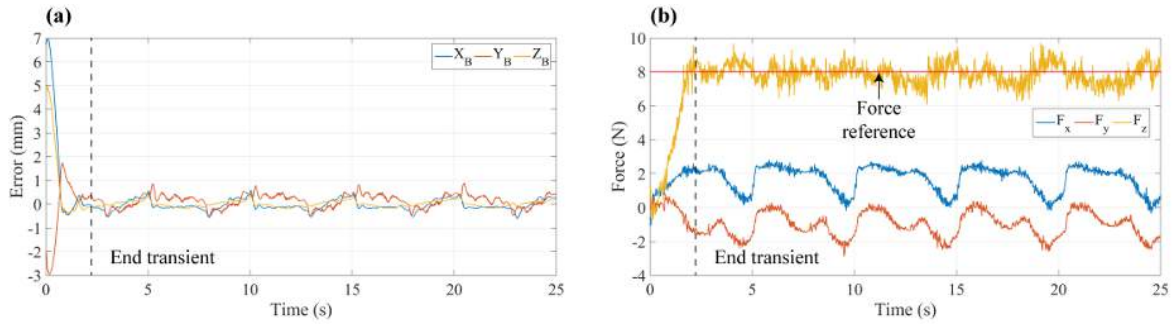


Figure 3.20: a) Compensation error over time and b) forces over time of a single trial using PMC method. From [DCS+17]

transducer as close as possible to the reference $P_v$, and consequently these forces preserve the contact area between the abdomen simulator and the pillow.

It is possible to tune the amplitude of these forces is through the configurable stiffness $K_f$. Being $K_f$ equal to 2, the maximum distance between the manipulator $EE$ and the virtual pivot point $P_v$ during this experimental trial is in the order of 3 mm.

Table 3.2 reports the mean, standard deviation, and maximum values of the compensation error for both the PMC and the linear compensation method. The linear method also compensates the motion of the target area with an error lower than 1 mm.

| | | TRIAL | | | | | | | | | | mean | std | T-test |
|---|---|---|---|---|---|---|---|---|---|---|---|---|---|---|
| | | 1 | 2 | 3 | 4 | 5 | 6 | 7 | 8 | 9 | 10 | | | |
| mean (mm) | Linear | 0.29 | 0.35 | 0.45 | 0.40 | 0.29 | 0.28 | 0.35 | 0.34 | 0.34 | 0.33 | 0.34 | 0.05 | true |
| | Angular | 0.38 | 0.38 | 0.38 | 0.46 | 0.26 | 0.44 | 0.50 | 0.52 | 0.45 | 0.47 | 0.42 | 0.07 | |
| std (mm) | Linear | 0.17 | 0.24 | 0.09 | 0.15 | 0.15 | 0.20 | 0.17 | 0.18 | 0.16 | 0.18 | 0.17 | 0.04 | false |
| | Angular | 0.14 | 0.15 | 0.15 | 0.13 | 0.14 | 0.23 | 0.19 | 0.17 | 0.21 | 0.14 | 0.16 | 0.03 | |
| max (mm) | Linear | 0.93 | 0.84 | 0.79 | 0.93 | 0.82 | 0.75 | 0.93 | 0.85 | 0.83 | 0.79 | 0.85 | 0.06 | false |
| | Angular | 0.84 | 0.82 | 0.90 | 0.98 | 0.75 | 0.98 | 0.98 | 0.98 | 0.95 | 0.85 | 0.90 | 0.08 | |

Table 3.2: Results of the motion compensation strategies. For each trial the mean, the standard deviation and the maximum values are reported. It is also reported, for each indexes, the result of the statistical analysis performed using the one-tailed t-test and the mean and standard deviation of each index.

To evaluate differences between the linear and PMC methods, a statistical analysis was performed by means of one-tailed t-test. The alternative hypotheses are that the three indexes of the linear method are statically smaller than the indexes of the angular method. The tests do not reject null hypothesis for the standard deviation and maximum values, whereas confirms a statistical difference with 5% of significance level between the compensation methods for the mean index.

This result states that the performance of the linear compensation method is slightly better than

the angular method. However, the difference between the average values of the two mean indexes is 0.08 mm that is one order of magnitude less than the dimension of the HIFU focus.

It should be noted that while linear compensation performs slightly better than the proposed PMC method, it needs a larger acoustic window and it is therefore less applicable to real life scenarios, especially for treatments in the abdomen area, in which ribs force the treatment to stop whenever they cross the HIFU path,.

Moreover, it should be considered that while targeting error should always be kept as low as possible, a considerable margin of normal tissue (i.e. $> 1$ cm) is usually resected in clinical practice [IKW$^+$05] during kindey and liver tumor surgeries. Therefore, the difference in accuracy between the proposed PMC method and the linear compensation method can be considered as irrelevant in the context of potential applicability to clinical practice.

The proposed PMC method, while just slightly less accurate than the linear compensation method, has the key advantage of keeping approximately the same contact point between the skin and the transducer acoustic coupling system, thus enabling continuous targeting, resulting in shorter treatment times, and providing more flexibility in the choice of the acoustic window from which to carry out the treatment, which is critical for clinical applicability of USgHIFU [IKW$^+$05].

#### 3.4.3.3 Lesion Size Assessment

Since precise histological evaluation of HIFU-generated lesions is not feasible on the employed porcine kidneys, due to the structured tissue which does not guarantee reliable results among different experiment, lesions were also performed on a simpler phantom, i.e. a chicken breast, in order to quantitatively evaluate the accuracy of the different sonication strategies, by means of the histological analysis of the size and shape of the performed lesions.

Namely, 8 different tests were performed for each of the three different experimental conditions: static conditions (chicken breast not in motion), dynamic conditions with a linear compensation method, and dynamic conditions with the PMC method. These lesions were induced with a sonication composed of 20 time slots of 1 s with a duty cycle of about 90%.

The values of frequency and acoustic power of the sonications have been set to 1.2 MHz and 115 Watts, respectively. Lesion width ($d$) and length ($D$) were measured with a caliper. By approximating the lesion geometry as a symmetric ellipsoid (i.e. cigar shape), the volume ($Vol$) was therefore estimated as follows:

$$Vol = 4/3\pi d^2 D \tag{3.7}$$

The results show that the HIFU focal spot (6 dB region) has the typical cigar shape with a width close to 2 mm and length of about 10 mm. This cigar shape can be observed in Figure 3.21-a,

where three representative thermal lesions obtained on chicken breast samples using the same acoustic parameters are shown.

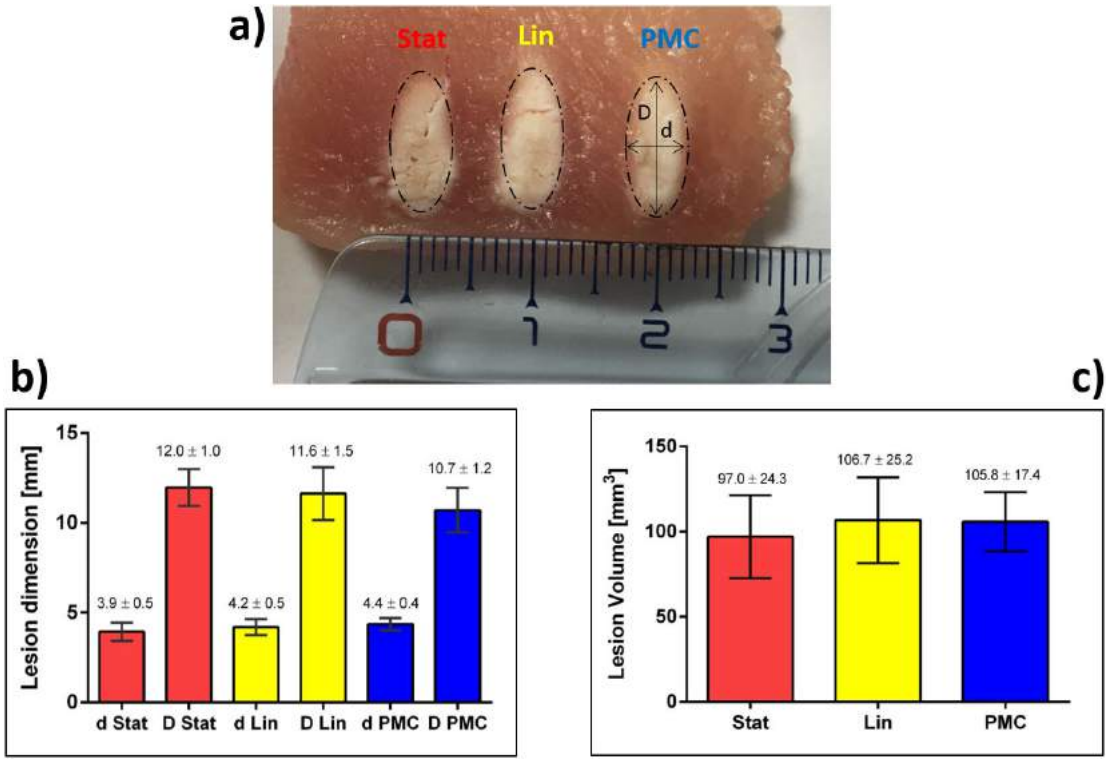


Figure 3.21: Lesions on chicken breast performed in: a) static conditions, b) dynamic conditions with a linear compensation method, and c) dynamic conditions with PMC method. The lesions were generated at 10 mm distance one from each other. From [DCS+17]

Lesion size was quantified through histological evaluation and the results reported in Figure 3.21-b and Figure 3.21-c demonstrate the high similarity in terms of length, width and volumes between the lesions induced in static conditions with the motorized slide turned off, and those obtained in dynamic conditions with the activation of the linear compensation and PMC methods, respectively.

The aim of motion compensation methods is to perform lesions during organ motion which are as close as possible to the ones obtained in static conditions. Therefore, these results confirm the high accuracy of the developed PMC method, together with the applicability of the proposed tracking and learning pipeline.

## 3.5 Discussion

Despite the rapid development and promising results of image-guided HIFU procedures (both under US or MRI), this technology suffers from important limitations, such as i) the poor flexibility in targeting and monitoring and ii) the inability to compensate abdominal organs motion during sonications.

A robotic-assisted approach for USgHIFU was presented in this chapter to try and overcome these limitations. The peculiar feature of this platform is represented by its two anthropomorphic manipulators that can be positioned directly on top of the patients, providing higher flexibility and enabling a wider range of procedures with respect to other state of the art approaches [SKMS17]. The integration of the different components composing the platform in a unique navigation system enabled the application of advanced therapy monitoring and delivery strategies.

A new motion compensation strategy suitable for robotic USgHIFU abdominal procedures was introduced, described and assessed through experimental tests exploiting the FUTURA platform. The main innovation of the proposed method resides in the combination of the angular motion of the HIFU transducer, kept in contact with the patient's skin thanks to a dedicated acoustic coupling system and a force control strategy, with the fast adjustment of the focal depth thanks to the axial electronic steering capabilities of an annular array HIFU transducer. This procedure is made possible by a navigation system that incorporates a tracking and learning pipeline which is capable of identifying and predicting the target trajectory on US images.

Compared to the existing solutions for compensating organ motion (e.g., linear motion tracking strategies [SKMS17]), this solution allows to just slightly modify the acoustic window, thus minimizing reflection and attenuation problems of heterogeneous tissues.

Several future developments of the proposed system and methods are foreseen, including:

- Further experimental validation. Real life applicability of the proposed system and motion compensation strategy should be verified through in-vivo tests on animals. In this type of tests it would also be possible to evaluate the produced lesions by using US contrast media to highlight blood diffusion changes before and after treatment, thus highlighting burned areas, as proposed by recent studies [GWW$^+$17] [CZX$^+$15].

- Extension to 3D tracking. The system accuracy was demonstrated in a dedicated setup for simulating breathing in the case of 1D motion of the target (e.g., cranio-caudal movement of kidneys [SPM84]), which is not always the case since anter-postierior movement can be non-negligible [GWJ$^+$09]. Both the PMC strategy and the trajectory learning strategy does not rely on the motion being 1D or 2D, but since TLD-based tracking happens on 2D B-mode US images it is not possible right now to track off-plane movements of the target. The usage of suitable 3D US probes coupled with an appropriate tracking method

(several 3D US tracking strategies have been covered in [DLBK+15]) can be considered a promising next step in the evolution of the presented robotic platform.

- Accounting for larger tissue deformations. Tissue deformation is a relevant problem in clinical applications. The employed tracking algorithm tracks features nearby the target area adjusting to its changes in shape and appearance over time. By deciding to track a single region of interest, we assume that, locally, the changes in shape and appearance will be moderate and that inter-distances between the tracked features and the treatment target will not change considerably. Extending this approach to compensate for larger tissue deformations is one of the envisioned future developments of the system, since it becomes particularly relevant when the treatment of larger volumes (i.e. through multiple consecutive sonications) has to be planned, as in more realistic abdominal tumor ablation scenarios.

- Extension to other types of USgHIFU therapy. Even if the proposed motion compensation method was drawn-up mainly for high intensity focused ultrasound applications (e.g. tumor ablation), the proposed system and strategy can also be applied whenever a focused ultrasound stimulation is required in a moving abdominal organ. Examples of alternative applications are: targeted drug delivery [CFK+14], ultrasound-induced immunomodulation [HPS+11], sensitization to chemotherapy [SPLG05] and sensitization to radiotherapy [FPS+11].

# 4 Ultrasound-Guided Neurosurgery

Neuronavigation is one of the oldest branches of IGS. The neurosurgical community was the first to adopt image navigation in its surgical routine, due to the fact that the task of operating the brain requires close-to-perfect planning and gives very little room for mistakes during the procedure.[MJB13].

In these demanding conditions, any technological help can increase surgeon confidence and accuracy, both in the planning phase and during surgery, resulting in better outcome for the patient.

Comprehension of intraoperative imaging is critical for the outcome of neurosurgical procedures but it isn't always trivial. This is the case of iUS technology, which has shown limited adoption despite its potential. The focus of this chapter is to describe the design and development of novel systems and strategies to provide neurosurgeons with better ways to correctly decipher iUS images during surgery.

This objective is pursued by a) realizing a novel training and simulation instrument (described in section 4.3) and b) developing techniques for intraoperative surgical microscope and iUS image navigation and fusion (described in section 4.4).

Part of the work described in this chapter has been published by the author in [PPM+17].

## 4.1 Image Navigation in Neurosurgery

Image navigation has been applied to a number of neurosurgical procedures, including tumor resection, biopsies and pedicle screws placement [MJB13]. Numerous clinical studies showed how the usage on neuronavigation suites may result in improved patient outcome, especially in the case of glioma surgery [RWAS+00].

The main task of glioma surgery is to resect as much as possible of the tumor mass in order to avoid relapses. Gross total resection (resection with no visible tumor parts in post-operative imaging data) is reported to be one of the most impacting factors in survival rates [TMBN12], but it is usually difficult to realize in practice due to the difficulties in distinguishing tumoral tissue during surgery. Moreover, while supra-maxima resection (resection of the tumor as imaged by MRI plus a safety margin of up to 20 mm) has been shown to be a successful strategy [Duf13], it is not always viable due to the presence of functional areas of the brain in the resection margin.

During the first steps of the procedure it has become standard clinical practice to use a tracked instrument to display preoperative data on a dedicated monitor in the OR. Slices of preoperative data are extracted and shown by the navigation system of choice, the orientation and position of the slices being linked to the position and orientation of the tracked instrument. This process is used to optimize the opening of the patient's skull, an operation called craniotomy (depicted in Figure 4.1).

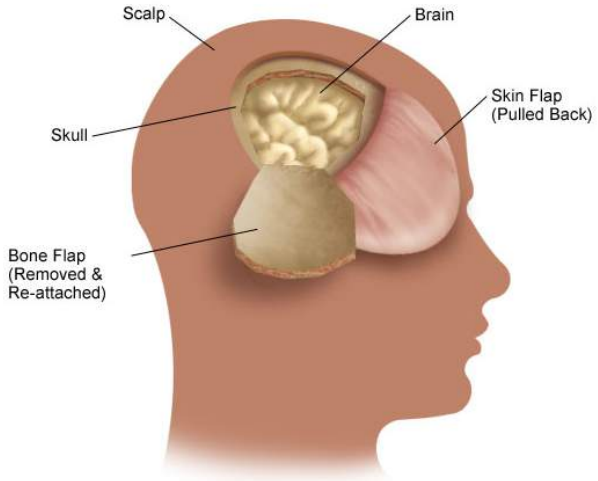


Figure 4.1: Scheme of a craniotomy: a preliminary step in glioma surgery procedures in order for the surgeon to reach the tumor tissue. Image from John Hopkins Medicine Health Library.

Visualization of the tumor area under the skull is crucial in order to minimize the size of the craniotomy, while simultaneously placing it in a way that will grant access to the tumoral mass. Reducing the craniotomy size can speed up the intervention, while reducing blood loss for the patient, as well as post-operative recovery [PWKT00].

During planning, surgeons can exploit advanced systems that enable the use of preoperative multimodal images to outline in the best possible way different anatomical parts that may be relevant to the intervention. MRI is usually employed to discriminate between soft tissue structures (and outline the tumor borders), while CT may be used to better outline bones, which is especially useful if skull fractures are involved.

The information coming from preoperative imaging is then elaborated by a software, automatically or with the aid of manual input, in order to define the optimal route to the tumor and thus the best position on the skull for the craniotomy.

Multimodal imaging also comes into play during the procedure, when real-time and multiplanar visualization of preoperative images from the surgeon point of view may aid anatomical comprehension of deeper brain structures, resulting in better tumor resections. [JJK$^+$06]. Moreover,

functional imaging can be used to map cortical functions and subcortical pathways, highlighting areas that should be preserved during resection in order to preserve patient neurological functions [NGF06].

Navigation systems and multimodal image fusion may also be used offline as a learning tool for less experienced neurosurgeons and trainees, which need to increase their confidence before going into the OR.

This is especially true when intraoperative imaging comes into play, which may be hard to understand and manage correctly without proper experience. In the following subsection, a brief overview of the most relevant intraoperative imaging sources employed during neurosurgery is presented.

### 4.1.1 Intraoperative Imaging

Imaging has been used to guide invasive procedures in the neurosurgical field since the early days of radiography. As they become more complex, but also more usable and portable, diagnostic imaging systems are starting to be considered a standard instrument in neurosurgical operating rooms.

Intraoperative imaging devices mostly comprehend iCT, iMRI and iUS (Figure 4.2).

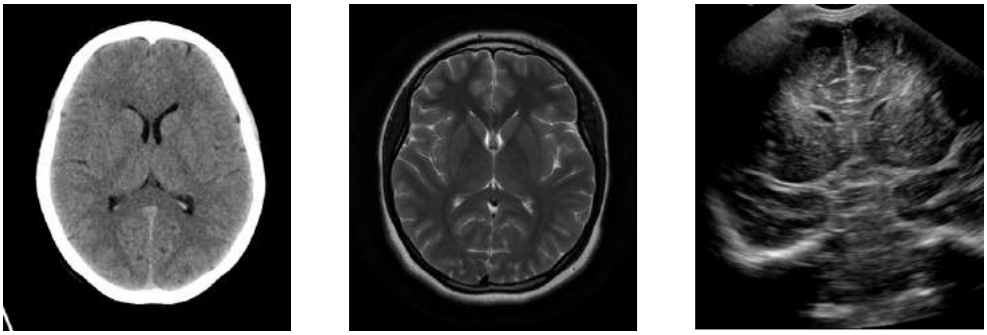

Figure 4.2: Examples of imaging of normal brain anatomy: CT (left), MRI (center), US (right).

iMRI has gained a lot of interest, thanks to its capability to outline brain tumors that have the look and feel of normal brain (i.e. low-grade gliomas). In these cases, without imaging aid, surgeons are forced to be aggressive, potentially resecting healthy areas of the brain around the tumor. iMRI can be used to evaluate the remaining tissue at any time, greatly improving the accuracy of the resection. [Bra02]. A number of studies confirm these findings in both pediatric [RBE+14], and adult populations [GZL+16]. Major downsides of iMRI are costs and compatibility with standard surgical equipment, which make its usage cost-ineffective in some cases[MCE+11].

iCT can be seen as a compromise between image quality, versatility, costs and usability [MJB13].

Compared to iMRI, latest iCT scanners enable shorter scan time and less limited patient positioning, at the cost of lower capabilities in soft tissue discrimination. Nonetheless, studies have shown iCT potential in residual tumor resection [LLC+11]. iCT may be especially useful in spinal surgery (which is often carried out by neurosurgeons in the same ORs needed for brain surgery), where bony structures need to be visualized in high resolution [SFED11].

iUS use is increasing in the neurosurgical community, despite this, it is still not considered a standard tool [FGPZ16]. iUS main benefits come from its real-time nature, its low impact on standard surgical procedures and its capability to identify tumor residuals, especially when used in conjunction with suitable contrast media [PPM+14]. One of the main limitations of iUS is its steep learning curve [Moi14].

Additionally, optical imaging is also emerging due to the development of fluorescent chemical compounds that can be shown by the operative microscope, which is a standard element of the OR, and can highlight blood flow or pathological tissues. [FGPZ16].

Intraoperative imaging technologies has yet to be exploited to their full potential, and multimodality imaging is still not very frequently used in clinical practice during surgery [FGPZ16]. iUS, in particular, appears to be under-used despite its potential.

A deeper analysis of the state of the art of current iUS guidance techniques in neurosurgery is presented in the next section.

## 4.2 US guidance in Neurosurgery

iUS saw a recent growth in Neurosurgery. The first reports [CKM+82] are now supported by larger case series publications [SMS00] [PAV+15] [PVF+14], which have widened and extended a full range of possible indications for this method, also thanks to the use of contrast medium during surgery with a technique which is usually called Contrast Enahnced Ultrasound (CEUS) [PPM+14].

iUS technique is recognized to be practical and handy, and has proven to be effective in the detection of brain lesions, both deeply and superficially located [PVF+14] [PPM+14]. It has been shown that iUS integration into routine tumor surgery is practical and feasible, also allowing real-time localization and visualization of residual tumor masses while operating. This is especially useful after brain shift have occurred (i.e. deformations occurring in the brain after recision of the dura mater membrane due to edema or tumor mass effect [RGW11] [SWM12] ), when typical preoperative imaging-based navigation systems usually lose their accuracy and can't be fully trusted by the surgeon. [PDBM+15] [PDBM+14].

The real-time nature of iUS comes in help of traditional intraoperative navigation systems, which otherwise can rely only on preoperatively acquired imaging datasets; intraoperative MRI could

also help in this matter, but, apart being much bulkier and more expensive, it doesn't allow continuous assessment.[KtMS+11].

Intraoperative CEUS has also been shown to be a valid alternative to intraoperative angiography, and can be used in order to assess perfusion of brain masses, identifying their fine vascular pattern together with larger arterial/venous blood supplies. [PMDB+14] [PDBS+15].

The main factor that is limiting iUS from really spreading and being accepted as a standard in neurosurgery is related to its strongly operator-dependent nature, in association with the steep learning curve necessary to master iUS technique. Neurosurgeons need to be involved in many cases, with large investments of time, in order to really be familiar and proficient with iUS.

Interpreting iUS represents a challenge to neurosurgeons, since the peculiar US physics principles (see Section 2.3.3) produce unusual images to the operator, with many different sources of artifacts and features that should be fully understood to be exploited in clinical practice. Due to this factor, identifying the correct matching between traditional imaging modalities (like MRI) and iUS is not trivial for the surgeon.

Moreover, neurosurgeons typically see and recognize preoperatively acquired, patient-specific anatomical features along the standard planes (axial, sagittal, coronal), while iUS data are usually obtained along arbitrary planes - depending on how the US probe is oriented in the space; the unorthodox imaging scans represent an additional difficulty in the understanding of the intraoperative information for surgeons which are approaching the technique.

High user dependency and unusual anatomical representations can actually be seen both as an advantage, by expert surgeons, and as a disadvantage, by trainees and less experienced surgeons [NNB11].

This factor makes training a critical subject for iUS, pushing research in this direction. Indeed, US simulation has seen a growing interest, with the objective of improving the overall training results of practitioners [NNB11].

Image fusion with other modalities such as CT and MRI is also fundamental during the learning process, enabling expert neurosurgeons with less experience on iUS to use their knowledge in the OR and adapt more rapidly. Moreover, systems that enable full iUS exam off-line review can represent a precious learning instrument by letting different groups share their expertise.

In order to tackle some of this open problems a novel application based on image-navigation for US training and case rehearsal in ultrasound-guided neurosurgery has been developed in the scope of this work, which is presented in the following section.

## 4.3 A Novel Application for US Training and Rehearsal in Neurosurgery

As previously described, iUS could represent an useful aid for neurosurgeons to perform better and safer operations thanks to real time and high-informative intraoperative visualization.

Since the diffusion of iUS is hampered by its learning curve, novel techniques are needed in order to teach how to perform iUS in neurosurgery to trainees and less experienced neurosurgeons.

The objective of this section is to describe the design and development of a novel method to teach iUS in neurosurgery. The new method is based on acquisition of US scans from patients undergoing surgical tumor resections, to be rehearsed and navigated later on in an off-line virtual 3D scene with the aid of hardware capable of mimicking the usage of an US probe. Preoperative and intraoperative data are fused together for aiding the knowledge transfer from common preoperative imaging modalities to iUS semiotics.

This novel method has been integrated in a complete software platform that has been developed as part of this thesis, in collaboration with Camelot Biomedical Systems[1] and the Besta NeuroSim Center[2]. Such a platform, which has been code-named "USim", has been tested during neurosurgical training course, showing promising results.

### 4.3.1 Simulation and Rehearsal System Design

In order to overcome some of the difficulties in understanding iUS, a new system, namely the USim training system, has been designed and developed, which allows neurosurgeons to familiarize with US imagining by simulating and rehearsing iUS scans coming from a library of real cases acquired at the Neurosurgery Department of the Fondazione IRCCS Istituto Neurologico Carlo Besta [3].

By simulating and rehearsing real cases, neurosurgeons can safely learn a number of useful skills, including:

- How to handle a US probe and how to move it on the dura mater or on the brain in order to replicate standard scanning planes;
- How to interpret and anticipate iUS appearance of important anatomical features and of different kinds of brain lesion.

[1] www.camelotbio.com
[2] www.bestaneurosim.com
[3] www.istituto-besta.it

The main concepts behind the design of the proposed simulation approach are related to image fidelity and portability. Differently from other state of the art approaches [MMH+14] - which rely on phantoms, slice extraction from volumetric interpolated US acquisitions and complex instrumentation - the objective of the development of USim was to create a simpler system that:

- can be run on any laptop with simple to no additional specialized hardware (the typical simulation setup is shown in Figure 4.3);
- only shows original iUS images comprehending artifacts and noise that are typically encountered in iUS.

While keeping a focus on these two objectives, realistic interaction and navigation experience should be provided in order for the simulation system to be as immersive as possible for the user.

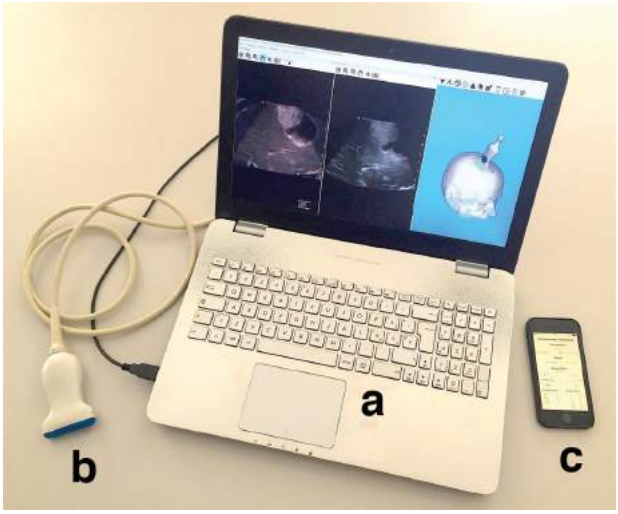


Figure 4.3: Typical setup for USim usage: a) a standard laptop, b) an usb virtual probe for interaction, c) optionally, a standard smartphone that can be used instead of the virtual probe. From [PPM+17]

In order to reach the first objective, which is portability, a crucial design choice was to exploit devices mimicking a US probe in which only orientation was tracked, instead of orientation and position. While reducing the degrees of freedom of the simulation, this allowed to exploit simpler hardware, like common mobile phones which are low cost, portable and accessible.

This choice is justified by the observation that little space is available after craniotomy, and that during a typical iUS scan the probe contact point stays fixed in one position. As a result, the position of the probe in the virtual environment has to be chosen by the user beforehand, while its orientation can be changed freely during the simulation.

For satisfying the second objective, which is image fidelity, only real patient data is employed in the system, acquired with an ad-hoc protocol to guarantee the creation of a satisfyingly large iUS dataset. Moreover, all of the acquisitions made by the leading surgeon during surgery were recorded, and they can be replayed later in the software.

In order to preserve all of the original features of the recorded US dataset, no image interpolation is performed in the system and only the originally acquired images are shown to the users.

Preoperative MRI data was also acquired and registered to the iUS dataset, in order to provide iUS-MRI image fusion during simulation, so that the learning process of the users can be aided by the MRI scans they are familiar with.

To realize efficient and effective navigation, a frame extraction strategy was designed, which selects the best image in the dataset in real time, based on the orientation of the employed probe-mimicking device.

An interactive virtual 3D scene integrates patient-specific data and intra-simulation information about the position and orientation of the user-controlled virtual US probe. Separate panels show the extracted iUS image and the corresponding preoperative MRI slice (Figure 4.4).


Figure 4.4: Example of usage of USim. The software shows the position of the probe on the preoperative patient data. From [PPM+17]

The following subsections describe all of the steps required for the realization of the described system.

### 4.3.2 Freehand Referenced US Dataset Collection

For each patient, a complete 2D US dataset was recorded by means of an ad-hoc developed acquisition platform connected to a commercial US system. The acquisition platform is composed of:

- A device capable of acquiring images from the chosen US system (i.e. a frame-grabber directly connected to a video-output port of the chosen US machine);
- An EMTS;
- A personal computer with an ad-hoc developed software capable of storing the images and the tracking coordinates.

During the US exam, all of the images generated by the US system are captured by the frame grabber (namely, the Epiphan[4] DVI2HDMI 3.0 framegrabber) and sent to the personal computer via USB, which stores them at a rate up to 60Hz, preserving their original quality and size.

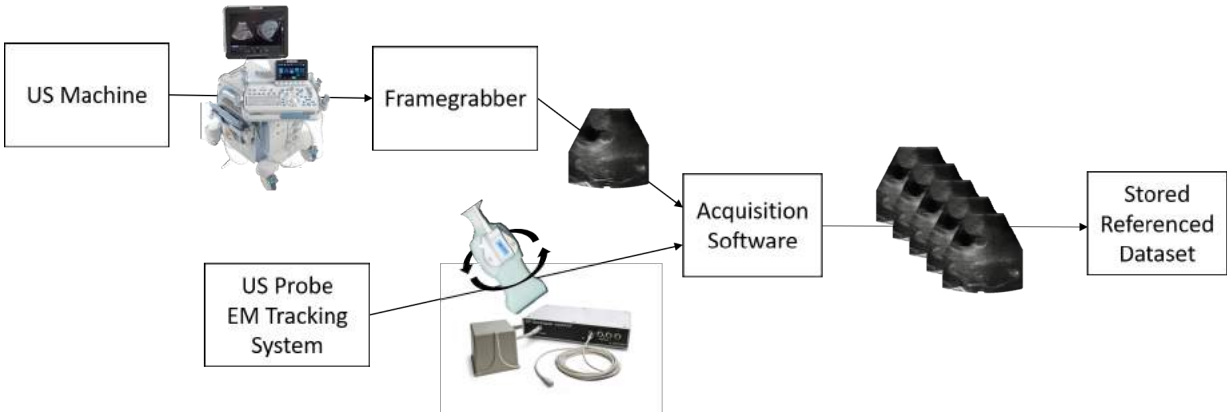


Figure 4.5: Referenced US acquisition scheme, the acquisition software combines and stores the information coming from both the framegrabber and the EMTS.

The orientation and the position of the US probe during image acquisition are simultaneously recorded, thanks to an EMTS, namely a Trackstar Drivebay [5].

The Trackstar Drivebay is an high-accuracy EMTS designed for medical applications, which is also employed for US tracking purposes in commercial US system (i.e. in the Esaote[6] MyLab Twice US machine).

[4] www.epiphan.com
[5] www.ndigital.com/msci/products/drivebay-trakstar
[6] www.esaote.com

The pose of a sensor attached to the US probe is continuously acquired and stored as a 7D tuplet (composed by its 3D physical position and 4D orientation quaternion), relative to the EMTS transmitter frame of reference.

Thanks to the known transform between the sensor frame of reference and the US probe transducer (since we exploit a commercial calibrated sensor holder), the recorded coordinates can be directly mapped to each US frame, defining its origin and orientation. Since the US depth is known for each acquisition, the image spacing is also computed (by dividing the depth for the number of rows in the image frame) and the image physical space is completely defined.

The developed acquisition software acquires simultaneously, in two parallel threads of execution, both the images coming from the frame grabber and the information coming from the tracking system. Every time a new image is acquired, its actual origin and orientation, in the EMTS transmitter frame of reference, is stored together with the imaging data. Additionally, the timestamp of the acquisition time is stored in order for the exam to be faithfully replayed later on.

#### 4.3.2.1 Acquisition Protocol

iUS was performed on several intraparenchymal and extraparenchymal brain lesions (e.g. lower/higher grade gliomas, meningiomas, metastases) in order to collect representatives case for the major neurosurgical pathology entity. Each patient's brain was scanned intraoperatively before opening the dura, to obtain a full US data acquisition. Additionally, all of the US scans acquired during the normal procedure are recorded by the system.

An acquisition protocol has been designed to acquire the required datasets during neurosurgical tumor resections.

The protocol should account for:

- Required time, which means that it should not slow down the procedure, posing risks for patients and increasing surgical costs.
- Acquisition completeness, which means that the acquired dataset should provide as many US orientations and positions as possible, in order to enable effective simulation.

Three typologies of acquisition are planned by the protocol: a) tilting acquisition, b) spinning acquisitions, c) sliding acquisitions.

Tilting acquisitions are performed with the following procedure:

1. Probe positioning in the center of the craniotomy
2. Idetification of the two available acquisition direction among the ones listed below:

- Sagittal (first acquisition) - Axial (second acquisition)
- Sagittal (first acquisition) - Coronal (second acquisition)
- Coronal (first acquisition) - Axial (second acquisition)

3. First direction acquisition: consisting in the probe slowly tilting from +45°to -45°in order to cover the lesion area in its entirety. The tilting should be slow in order to avoid blur and motion should occur:
    - From left to right in the sagittal plane (see Figure 4.6)
    - From anterior to posterior in the coronal plane (see Figure 4.7);
    - From up to down in the axial plane (see Figure 4.8).
4. Second direction acquisition, with the same acquisition pattern defined in the previous point.

Spinning acquisitions are performed with the following procedure:

1. Probe positioning in the center of the craniotomy, perpendicular to the brain surface;
2. Slow rotation of the probe around its axis by 360°;

Sliding acquisitions are collected only if the craniotomy is large enough to move the probe laterally. In case they are possible they are acquired as follows:

1. Probe positioning along the same axis of the first acquisition, but at the extremity of the craniotomy (left, for sagittal plane, anterior, for coronal plane, up, for axial plane)
2. Slow lateral sliding of the probe while keeping it perpendicular to the brain surface, covering the whole craniotomy span.
3. Repeat for the second acquisition direction

During the acquisition process, a suitable depth, frequency, and gain for the US is set so that the lesion and the anatomical feature in its surroundings are clearly visible.

Fixing the US parameters may be seen as a limitation, since it reduces the kind of images that trainees may learn from. Nevertheless, it should be considered that repeating acquisitions at different depth, frequency and gains would have been much more time consuming during surgery.

The described acquisition protocol has been designed in order to provide as many US orientations and positions as possible, preferring this aspect of the simulation (i.e. probe positioning) over

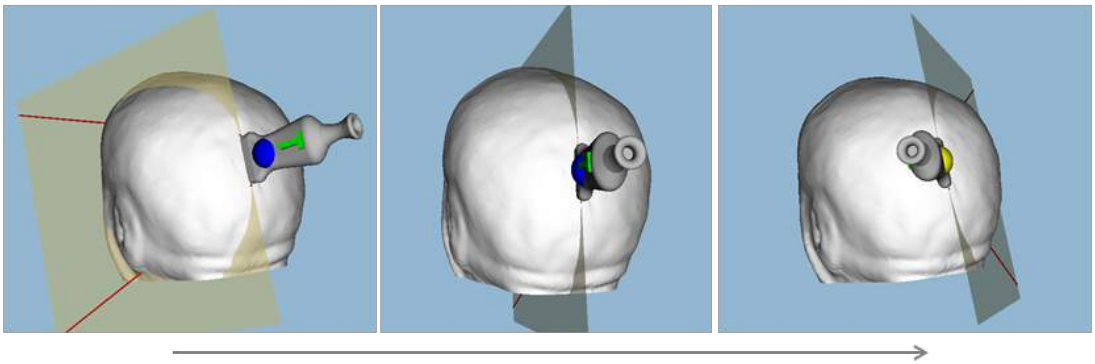

Figure 4.6: Tilting acquisition along the sagittal plane

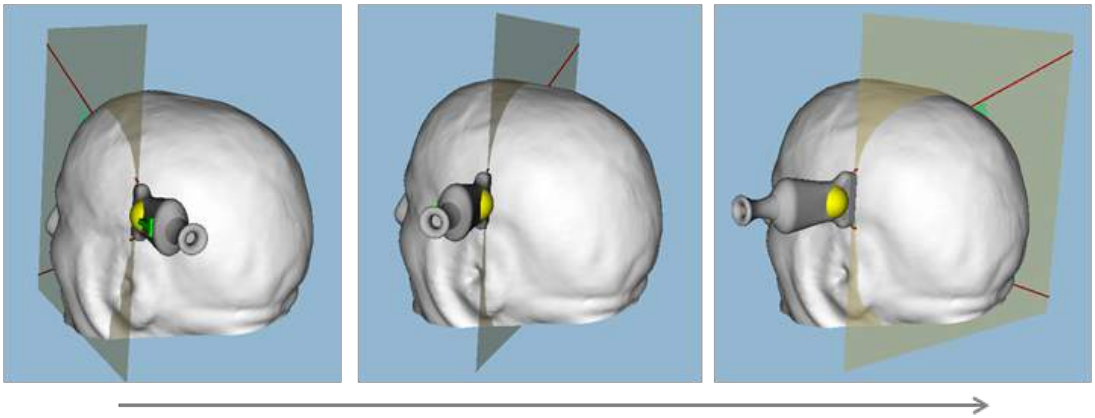

Figure 4.7: Tilting acquisition along the coronal plane

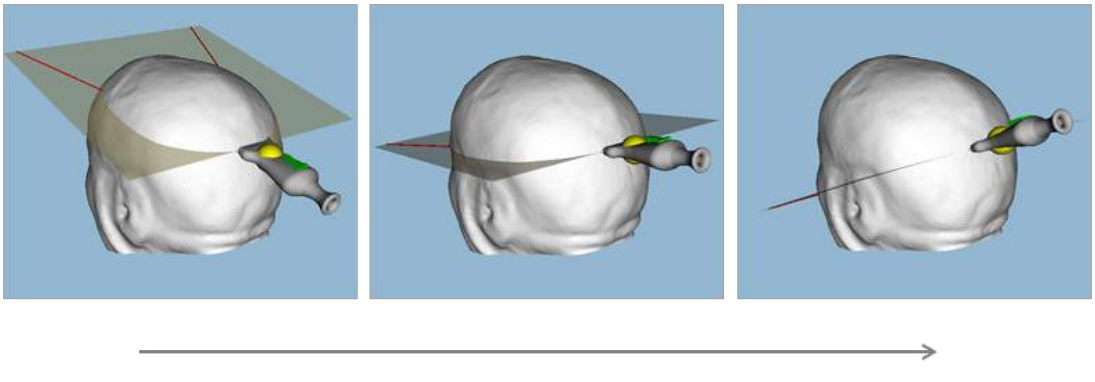

Figure 4.8: Tilting acquisition along the axial plane

the possibility to change US parameters. The assumption is made that given a clinical case, one set of US parameters may be considered optimal by the leading surgeon for highlighting the key anatomical structures that should be recognized by trainees and that are useful for carrying out the surgery.

A different acquisition protocol may be designed during further developments to acquire multiple set of US images while varying the main US parameters (i.e. gain, frequency, depth), at the price of acquiring less poses of the US probe. Trainees may then be enabled to select different imaging sets corresponding to several parameters combinations, in order to learn how they influence US imaging.

#### 4.3.2.2 Patient Registration

Registration between the acquired dataset (that lies in the EMTS transmitter frame of reference) and the preoperative MRI datasets (that lie in their own physical frame of reference) is performed via rigid landmark registration.

In order to perform the registration, the following steps are needed:

1. After surgical procedure completion, the positions of a number of anatomical landmarks on the skin of the patient are acquired using the same EMTS that is employed during the freehand referenced US acquisition.
2. The same anatomical landmarks are manually selected by the user on the surface rendering of the skin of the patient (Figure 4.9), previously segmented on the routine preoperative MRI dataset.
3. Given the points in the two spaces, the transformation matrix $\mathbf{T}_{\text{em}}^{\text{pre}}$ that minimizes the registration error can be inferred [Hor87] so that:

$$\mathcal{X}_{em} = \mathbf{T}_{\text{em}}^{\text{pre}}(\mathcal{X}_{pre}) \tag{4.1}$$

   Where $\mathcal{X}_{em}$ is a point in the EMTS transmitter frame of reference and $\mathcal{X}_{pre}$ is the corresponding point in the preoperative space.

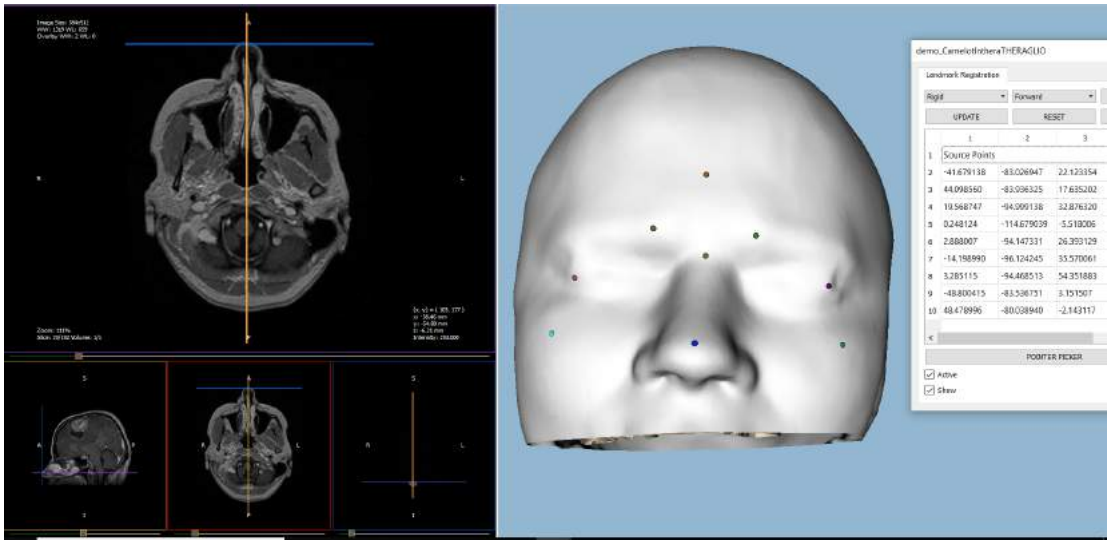


Figure 4.9: Point selection for preoperative data registration - interface of the developed software

### 4.3.3 Exam Navigation

Offline navigation of the original US images is made possible in the developed system by means of two different methods. In both cases, a navigation device sends its current orientation to the USim software; that information is shared thanks to its internal Attitude and Heading Reference System (AHRS).

The first method requires the use of a navigation device mimicking a real US probe, the "USim Probe" (Figure 4.10), connected to the USim simulator system via USB. The USim probe exposes a simple API for retrieving the current orientation of the instrument, which is expressed in the form of orientation quaternions.

The second method allows for a less realistic but more portable user-experience with the use of a commercial smart-phone as US probe (Figure 4.11), which is connected through Wi-Fi to the USim simulator thanks to an ad-hoc application which communicates to the main software via WebSocket protocol, constantly streaming the orientation of the device, expressed in the form of orientation quaternions.

Such a device is used to control, in an intuitive way, a virtual US probe in an interactive 3D scene, which shows the previously segmented patient skull, and the current position and orientation of the probe.

In order to initialize the navigation, two preliminary steps are required:

- Probe placement on the segmented patient skull: via mouse click on the automatically generated surface rendering, the user can chose in which of the available positions to

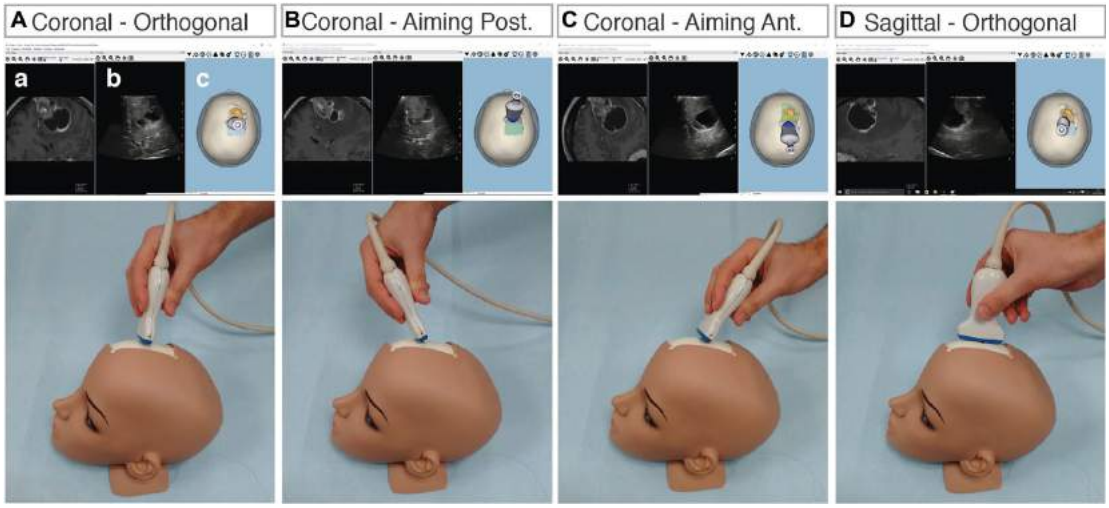


Figure 4.10: Example of rehearsal using the USim software and a virtual probe on a mannequin. From [PPM+17]

Figure 4.11: A common mobile phone can be used in order to simulate the probe positioning on any surface. From [PPM+17]

place the probe (i.e. the positions in which images have been acquired with the previously described acquisition protocol);

- Orientation initialization: the user is requested to place the navigation device of choice in a desired starting orientation, matching the one displayed in the 3D scene.

After these two steps, the user can start navigating. While the user moves the virtual probe (i.e. by moving the chosen probe-mimicking device), the US image with the closest position/orientation with respect to the patient is extracted from the recorded US dataset and presented in real-time to the user. The frame extraction strategy is described below.

#### 4.3.3.1 Frame Extraction

Once the user moves the probe, the software updates the virtual probe orientation in the virtual space and extracts a iUS frame which is close to the current position and orientation, choosing from the previously acquired dataset.

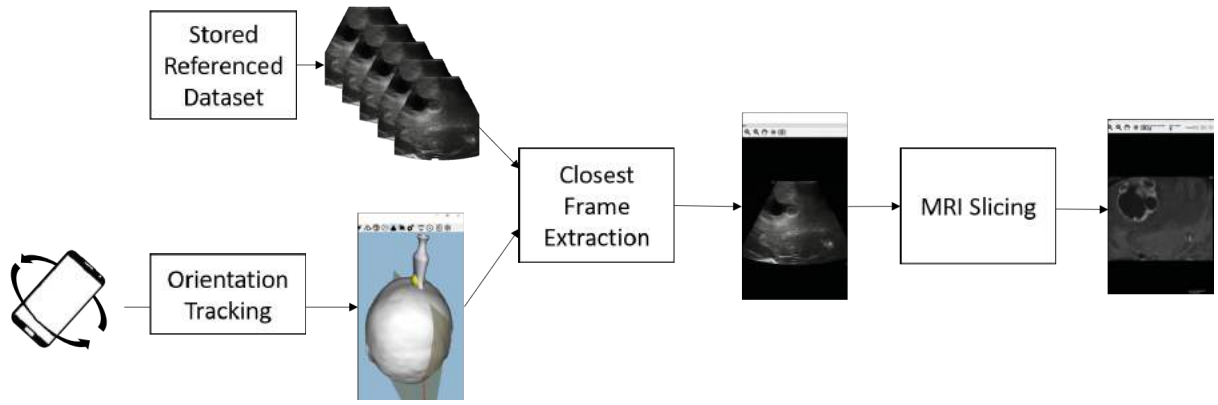


Figure 4.12: Frame extraction scheme: the software chooses an US frame among the available ones, on the basis of the position of the virtual probe in the 3D scene.

This result is obtained through the following procedure.

Let the virtual probe transducer position and orientation be represented as a tuple $v_{p,q}$ consisting of the 3D position of the center of the virtual US image and 4D quaternion.

$$v_{p,q} = \{v_p, v_q\} \tag{4.2}$$

where $v_p \in \mathbb{R}^3$, $v_q \in \mathbb{R}^4$ represent 3D position and 4D quaternion of the virtual probe respectively.

Let $m^{th}$ acquisition of an iUS dataset composed by $M$ frames, be represented as a tuple $u^m_{p,q}$ consisting of 3D position of the center of the image, 4D quaternion, and a timestamp of acquisition.

$$u^m_{p,q,t} = \{u^m_p, u^m_q, u^m_t\} \tag{4.3}$$

where $u^m_p \in \mathbb{R}^3$, $u^m_q \in \mathbb{R}^4$ and $u^m_t \in \mathbb{R}$ represent 3D position, 4D quaternion and timestamp of $m^{th}$ frame respectively.

Let the timestamp of the currently displayed iUS frame (or to the first timestamp in the iUS dataset in the case of the first run of the procedure) be $t_{curr}$.

The problem is to find the frame $\eta$ that best matches the current virtual probe position and orientation,

$$\eta = \arg \max_{m \in \{1,\ldots,M\}} D\left(u^m_{p,q,t}, v_{p,q}, t_{curr}\right) \tag{4.4}$$

The objective is to find a function $D$ that, given all iUS frame tuplets of position, quaternion and timestamps, can select the tuplet which is similar to the current virtual probe position.

The function $D$ in eq. (4.4) is actually a measure of a geometric based similarity (which is based on probe position and angle), that also takes in consideration the difference in acquisition time between consecutive extracted frames. Image content is not taken in account in the similarity measure, under the assumption that the registration of the US dataset with the pre-operative patient space is accurate and that the final purpose is the system is to only enable extraction of the already co-registered US and MRI scans.

The estimation of $D$ can be broke down in the following steps,

1. For a given virtual probe position $v_p$, all the points in the iUS dataset which lie within a specific radius are selected. Let $\rho^m$ represent the distance between $m^{th}$ frame position $u^m_p$ and current virtual probe position $v_p$

   $$\rho^m = \|v_p - u^m_p\| \tag{4.5}$$

   Let $c_1, c_2, c_3, \ldots\ldots, c_K$ represent indices of the K neighbors in the iUS dataset that lie within a certain distance $\epsilon$ of $v^*_p$

   $$c_k = m \quad \text{if} \quad \rho^m < \epsilon \quad \forall m \tag{4.6}$$

   where $c_k \in \{c_1, c_2, c_3, \ldots\ldots, c_K\}$.

   Such task is made efficient by exploiting a C++ k-d tree implementation available in the Fast Library for Approximate Nearest Neighbors (FLANN) [ML09].

2. The angular distance of the selected frames with respect to the current orientation of the virtual probe is computed. The angular similarity function between current virtual probe quaternion $v_q$ and $c^{th}_k$ iUS frame quaternion $u^{c_k}_q$ is defined as [Huy09],

   $$\psi^{c_k} = 1 - \left| v_q \cdot u^{c_k}_q \right| \tag{4.7}$$

   where $0 \leq \psi^{c_k} \geq 1$, 0 representing two identical orientation. The selected frames are ordered by means of an aggregated metric:

   $$d^{c_k} = \frac{\rho^{c_k}}{w} + \psi^{c_k} \tag{4.8}$$

Where $w$ is a weight that serves the purpose of scaling the positional distance with respect to the angular distance ($w = 125$ in our implementation). The low value $d^{c_k}$ represents a particular iUS frame which is geometrically close to the current virtual probe position and angle. The $J$ indices are then rearranged in ascending order of aggregated metric, i.e.,

$$s_j = c_k \ : \ d^{s_j} < d^{s_{j+1}} \quad \forall k \tag{4.9}$$

where $j \in \{1, 2, 3, ...., K\}$.

3. Once the resulting frames are ordered, the top $J$ frames are taken and the one is selected which is the closest in acquisition time with respect to the last chosen frame, i.e.,

$$\eta = \arg \min_{s_j \in \{s_1, ..., s_J\}} \left( t_{curr} - u_t^{s_j} \right) \tag{4.10}$$

This step is useful in order to provide smoother transitions between frames when the user is following a path that is close to the one of the original acquisition, but not identical, and multiple frames have been acquired in the same position and orientation at different times (e.g. during the tilting acquisition step and the spinning acquisition step). The assumption is made that when very close frames (in terms of spatial similarity) are selected, the best simulation experience is guaranteed by presenting to the user that one frame which has been collected during the same acquisition step of the currently shown frame.

Following this procedure the US images that are presented to the user are not altered in any way with respect to the original acquired US/MRI data sets.

While through interpolation it could have been possible to reconstruct the most likely appearance of the US image from any given position and orientation of the virtual US probe, the choice was made to only present original non-interpolated images in order to preserve all of the original US features (such as noise, reflections and other typical US artifacts).

#### 4.3.3.2 Image Fusion

Thanks to the registration between the preoperative patient space and the EMTS transmitter frame of reference (the physical space of the acquired iUS dataset) the acquired oriented iUS images can be co-localized onto the preoperative MRI data, allowing an offline, synchronized navigation of the two imaging modalities.

Whenever an iUS frame is shown by the system, a slice with the same orientation, origin and extent of the chosen US image is extracted from the registered preoperative MRI dataset. This image is shown to the user either in a separate window, or fused with the corresponding iUS frame.

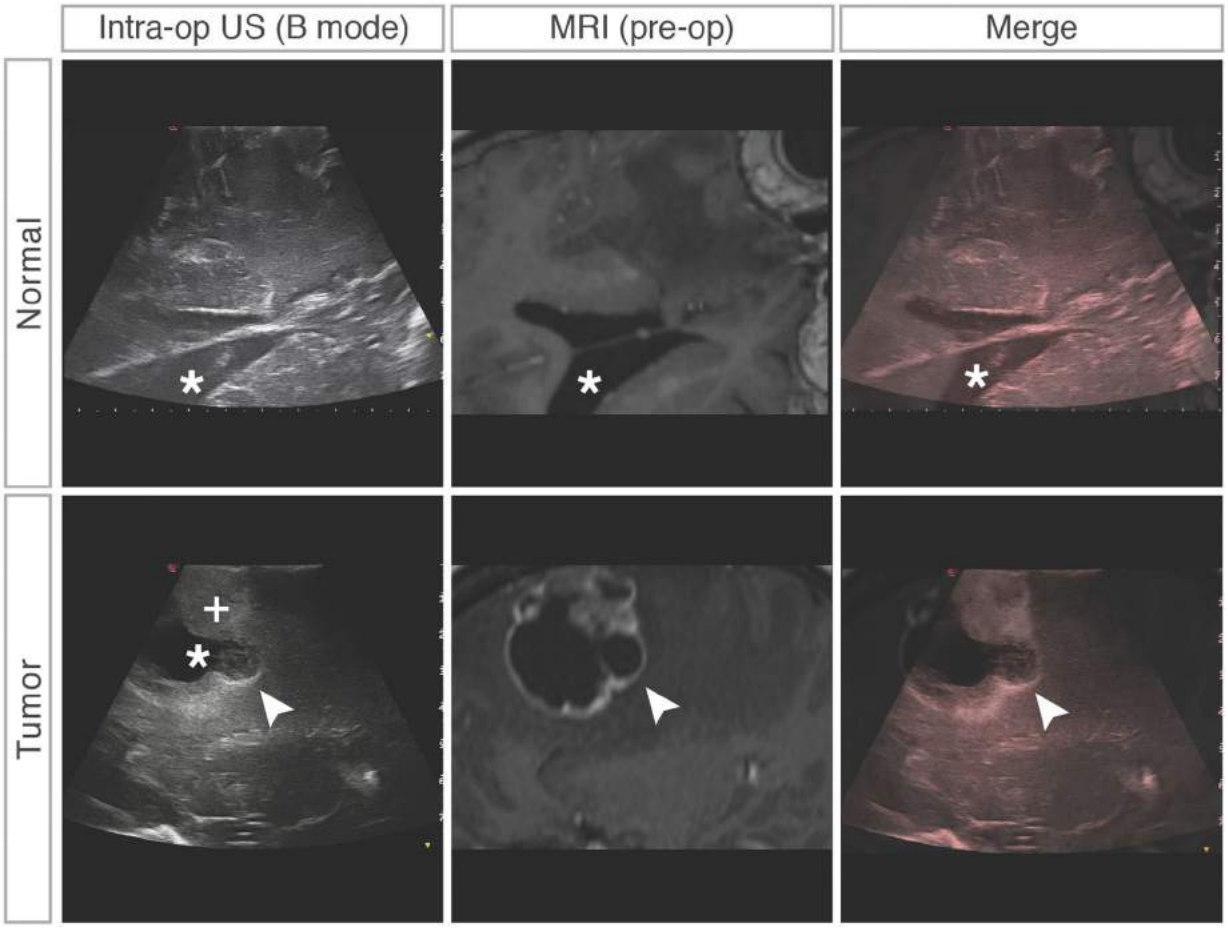


Figure 4.13: Example of image fusion using the USim software. Normal anatomy in the top panel, a brain tumor in the bottom panel. From [PPM+17]

Neurosurgeons might decide to simulate by means of US scans alone, or to superimpose traditional, coplanar MRI images to what they are visualizing as US images, according to their personal learning curve and confidence level.

In order to let the two modalities merge smoothly when superimposed, the US images intensities are mapped to *RGBA* values (i.e. values in the *RGB* color space plus an alpha value, representing the opacity of the pixel) applying the following method to each pixel of the acquired US image:

- Let $x$ be the normalized grey-level intensity in the $[0-1]$ range of a pixel in the image, where the value 0 is equal to a black pixel and the value 1 is equal to a white pixel.
- Let $(r_v, g_v, b_v)$ be a selected blending color expressed as a normlalized *RGB* triplet, the final

RGB components of the pixel in the output image $(r, g, b)$ are obtained as:

$$\begin{aligned} r &= x * r_v * 255; \\ g &= x * g_v * 255; \\ b &= x * b_v * 255; \end{aligned} \tag{4.11}$$

- Let $a_{req}$ be the requested blending level between the two images, the actual alpha value $a$ of the pixel in the new superimposed US image is computed as:

$$a = min(1, \frac{x - 0.5}{1 + \mid x - 0.5 \mid}) * a_{req} \tag{4.12}$$

The output of this blending process is shown in Figure 4.13.

#### 4.3.3.3 Exam replay

As an additional functionality, the system allows neurosurgeons to visualize and practice the original iUS exams that were originally acquired by neurosurgeons in the operating room as part of the standard surgical routine.

In this configuration the user can visualize not only the US images and the correspondent MRI images, but also the position of the probe on the patient's head and how the surgeon moved/oriented the probe during the acquisition.

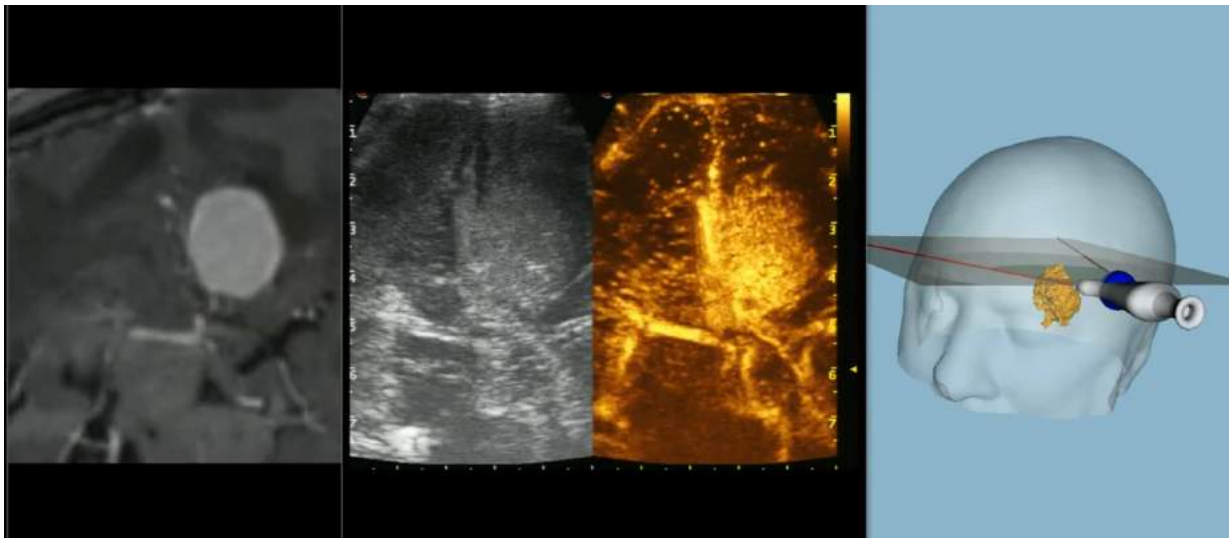

Figure 4.14: Example of CEUS exam replay in the USim application.

The whole exam can be replayed as it was performed by the surgeon; the user can pause or rewind it at any time. This is especially useful when replaying CEUS (Figure 4.14), allowing the user to appreciate the different US appearances related to the diffusion of the contrast media in the tissue.

Besides, the user can choose to stop the exam anytime to freely interact with it, by changing the probe orientation in order to navigate through the acquired US dataset, or just by adjusting the level of fusion of the two modalities. Moreover, annotations provided by the original surgeon can be added to any iUS frame, thus making them available in the software during exam replay.

In this manner, it will be possible for different groups to share their expertise with other neurosurgeons who want to practice and study the cases they have operated iUS.

### 4.3.4 Results

An intuitive, handy and simple simulation and rehearsal device that lets neurosurgeons familiarize with US brain anatomy and learn iUS semiotics may help increasing the diffusion of this modality, that has great potential but still scarce adoption in clinical practice.

The USim simulator was developed trying to find a balance between portability of the simulation system, navigation ease and completeness and fidelity of the provided information.

Thanks to the developed system, neurosurgeons have the opportunity to picture, learn, practice, and simulate this new methodology without using dedicated hardware, but potentially using just their smartphone and laptop.

By enabling simulation without complex instruments, surgeons may integrate a training session in their routine, which often does not give them enough free time to approach more complex and time-consuming systems.

The employed system could allow any neurosurgeon to not only practice and rehearse this technique, but also find pre-registered cases of patients with a comparable lesion to the one that the neurosurgeon must imminently operate on in the OR, thus simulating pre-surgical intraoperative US visualization.

Neurosurgeons may familiarize and practice iUS on those cases by means of USim, so that when they will have to operate and use iUS themselves they will be already accustomed and familiar with the technique, saving time in the OR, and performing the operation with more confidence.

#### 4.3.4.1 Preliminary Validation Study

This iUS training method was tested on a small cohort of European neurosurgery residents at the European Association of Neurosurgical Societies [7] training course (2016 edition, located in Sofia, Bulgaria).

This was a one-on-one training session meaning that the instructor sat alongside each candidate, as they individually reached the USim stand. All candidates (No. 14; 8 men, 6 women; postgraduate year 4-5, with comparable surgical experience).

The instructor showed each candidate the preoperative MRI scan of a right frontal intraparenchymal tumor (previously iUS recorded and operated on at the Fondazione IRCCS Istituto Neurologico Carlo Besta [8]).

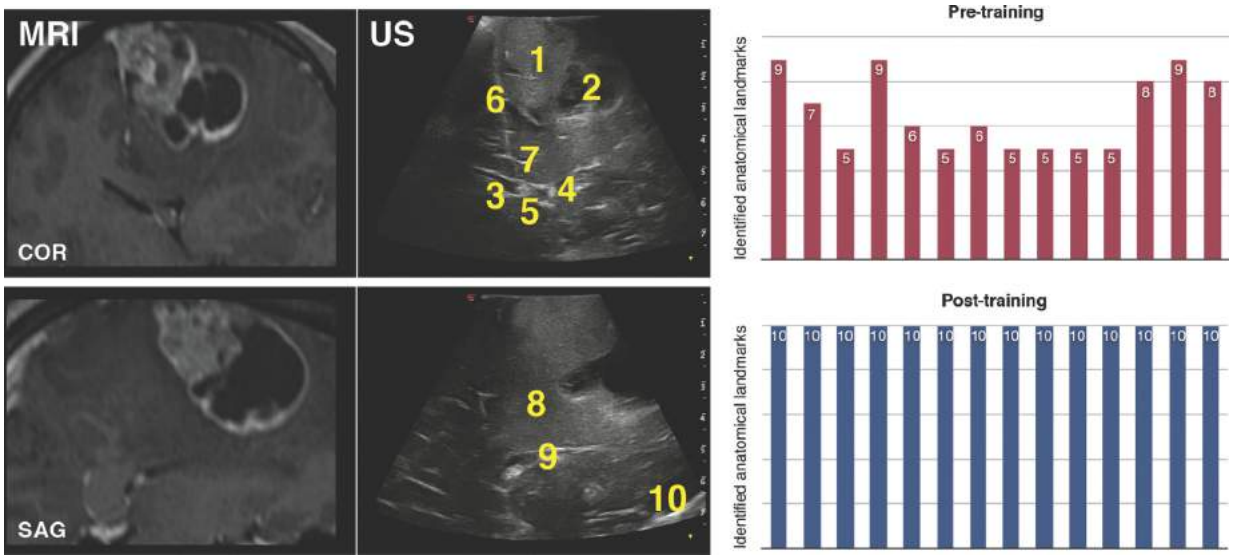


Figure 4.15: Fourteen European neurosurgery residents were first asked to identify 10 anatomical features using the developed software and visualizing US images only-scans. Each trainee could recognize 5 to 9 structures out of 10 (top graph - pre-training) before rehearsing the case and practicing with paired MRI-US scans by means of the USim (right + left columns of the panel). After rehearsal all the residents precisely identified all 10 anatomical structures on US images (bottom graph - post-training). From [PPM+17]

Once the case was evaluated, the candidates had to handle the smartphone with the USim app installed, and they were asked by the instructor to precisely identify 10 anatomical structures, while navigating and seeing US images only (evaluation #1). At this stage, candidates could identify correctly only 5 to 9 structures (Figure 4.15-right side, top).

[7] www.eans.org
[8] www.istituto-besta.it

The instructor then explained to the participants the differences in these imaging modalities and let them practice with USim by navigating through the coplanar, coregistered US and MRI scans.

At this point, their understanding and comprehension level noticeably improved, so that when the 14 candidates were asked to repeat the initial task (US navigation only) they recognized all of the anatomical landmarks (evaluation #2; Figure 4.15-right side, bottom).

These preliminary results show how such an instrument can be useful to teach how to transfer specific MRI features to US (i.e. helping trainees in the task of memorizing different feature appearances). A different experimental setup, exploiting an independent test set composed by US scans of different anatomical features (i.e. anatomical features not shown in the training step in which coregistered US and MRI scans were navigated), would be needed in order to evaluate a trainee general confidence in interpreting and understanding US data.

## 4.4 Techniques for Surgical Microscope and US Image Fusion

As described in the previous sections, iUS in neurosurgery suffers from a critical interpretability problem that is limiting adoption and effective usage. One of the ways to deal with this problem, both in training and during intraoperative navigation, is to exploit image fusion techniques to display iUS together with other modalities, which are usually preoperatively acquired.

One step further in tackling this problem can be represented by the integration of iUS with images coming from the operating microscope that neurosurgeons usually employ during the entirety of the procedure.

As presented in Section 2.5.3, surgical microscope image fusion with preoperative data was already proposed in [PFJ05]. One of the limitation of that approach is represented by the brain shift problem. As mentioned in Section 4.2 after the opening of the dura mater membrane, brain warping occurs due to a number of factors including gravity, edema, and tumor mass effect [RGW11], thus changing brain anatomy with respect to its preoperative appearance [SWM12].

Being acquired intraoperatively after brain shift, iUS is not affected by this problem and its fusion with surgical microscope images is always reliable during the procedure, without the need of applying complex brain shift compensation techniques.

By merging brain surface reconstructions obtained from the surgical microscope, which practically represents the surgeon field of view, and slices of the tissue which lies underneath, acquired through iUS, one can obtain a complete representation of the target area, enhancing anatomical comprehension during surgery.

This section objective is to describe the design and development of techniques needed to realize an

image navigation system capable of combining the 3D reconstructions of the surgical microscope field of view with iUS images, to provide a comprehensive multimodal visualization during neurosurgical procedures. In order to reach this objective, the following steps are needed:

- An image processing pipeline has to be developed to capture the stereo information coming from the microscope and reconstruct a 3D surface from it. The task of obtaining depth information from stereo image pairs is well known in literature [TV98], and standard stereo calibration and stereo reconstruction algorithms can be exploited for this purpose in this context, as shown by other works on surgical microscopes [FDSJ01] [PFJ05] [JFRP14] [KMP+15];
- The microscope position should be referenced with respect to the intraoperative patient space. An EMTS, the same one that is employed in the OR to register preoperative data and iUS, is used to track the position of an EM sensor on the microscope head, which has to be properly calibrated in order to find its transform with respect to the 3D reconstruction space.

After these two steps, a 3D reconstruction of the surface of the brain can be displayed together with iUS images into an interactive 3D environment which may enable surgeons to analyze intraoperative patient's data more intuitively, supporting decision making during surgery. Moreover, the obtained 3D reconstructions could also serve as an additional intraoperative information to be added to neurosurgical training tools, like the one presented in the previous section.

The following subsections describe all of the steps that were needed in the realization of such a system, along with preliminary experimental results.

### 4.4.1 Stereo Image Processing Pipeline

An acquisition and processing pipeline is employed to obtain 3D surfaces from the microscope images. Three main steps can be identified in order to reach this objective:

- Stereo acquisition from the surgical microscope
- Stereo calibration of the surgical microscope
- Reconstruction of a 3D surface from a stereo image pair

The following subsections describe each step in details.

#### 4.4.1.1 Stereo Acquisition

In order to generate the required depth information regarding the microscope field of view, the stereo signal coming from both the left and the right camera of the microscope must be acquired. Since both left and right video channels are needed, a Zeiss[9] Pentero 900 Surgical Microscope connected to a Zeiss Trenion 3D HD system is employed.

The Zeiss Trenion 3D HD system is capable of acquiring the stereo signal from the microscope and transmitting it to a dedicated 3D Monitor. Such a system is usually employed for teaching purposes, in order to share to trainees the 3D visualization otherwise available only to the main surgeon through the microscope oculars.

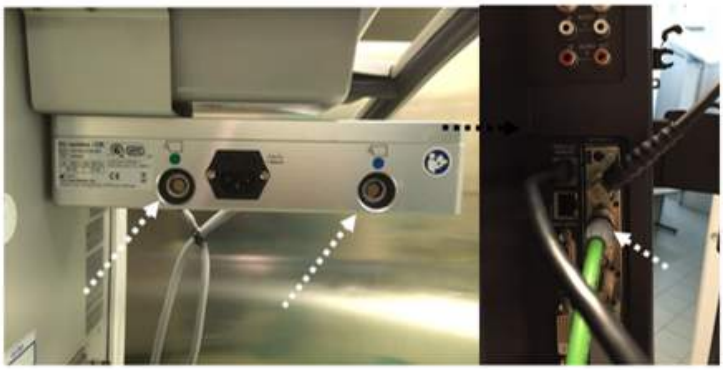

Figure 4.16: Zeiss Trenion 3D HD video output ports (left) and 3D monitor HD-SDI video output port (right).

An output HD-SDI video port is available on the 3D Monitor (Figure 4.16, from which it is possible to acquire the needed video signal in a side-by-side stereo format directly from the monitor, while using the Trenion system. An acquisition pipeline composed of an HD-SDI to HDMI converter (Figure 4.17) and an Epiphan[10] DVI2HDMI 3.0 framegrabber (Figure 4.17) is employed in order to get access to the high-definition stereo video stream of the surgical microscope.

Through this acquisition pipeline it is possible to acquire the full resolution (i.e. 1920x1080) video signal of the Zeiss Pentero 900 surgical microscope at a frame rate of a 30 Hz using a common Windows 10 laptop equipped with an USB 3.0 port. A sample of the stereo channels acquired in this way is presented in Figure 4.18. The stereo video signal is then automatically processed in order to split the left and right video sources, which are individually saved by an ad-hoc developed software exploiting the proprietary API of the employed framegrabber.

[9] www.zeiss.it

[10] www.epiphan.com

Figure 4.17: Acquisition pipeline hardware components, an HD-SDI to HDMI converter (left) and an Epiphan DVI2HDMI 3.0 Frame-grabber (right).

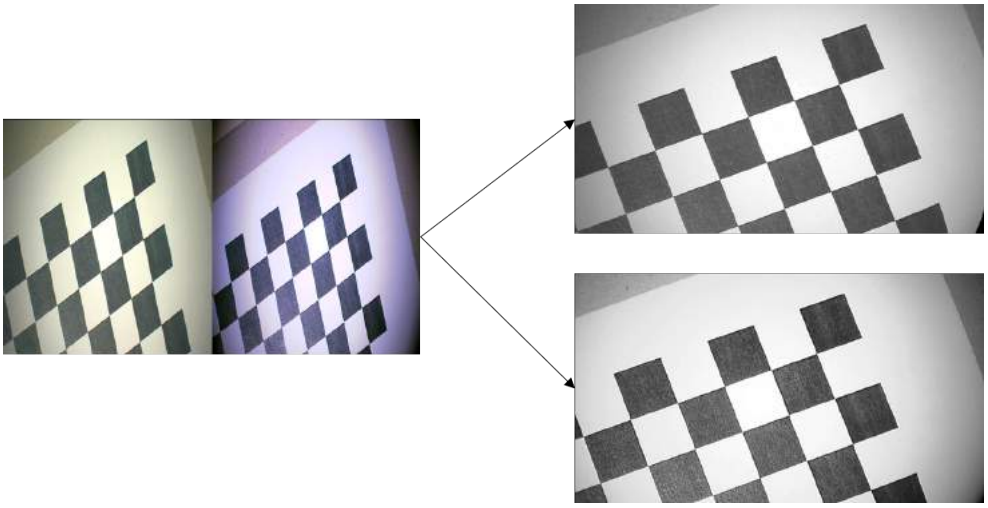

Figure 4.18: The signal acquired from the 3D monitor is splitted into its left and right components. To avoid the introduction of artifacts, the image size is halved after splitting, i.e. from one 1920 $\times$ 1080 3D side-by-side image, two 960 $\times$ 480 images are obtained.

#### 4.4.1.2 Stereo Calibration

Calibrating a stereo system is the task of estimating its configuration, comprising the parameters describing each of the two cameras, and the transform that maps the relative pose between them. This operation is typically carried out through the analysis of a calibration acquisition [Zha00].

The first step of the calibration procedure is related to the computation of the complete set of parameters that describes each camera. The camera parameters, in the well known pinhole camera model, can be divided in extrinsic and intrinsic parameters.

Let $\mathbf{X}$ be the 3D coordinates of a world point, then this point can be mapped to camera coordinates

$\mathbf{X}_{\text{cam}}$ by means of the extrinsic parameters $\mathbf{R}$ and $\mathbf{t}$ as follows:

$$\mathbf{X}_{\text{cam}} = \begin{bmatrix}\mathbf{R} & \mathbf{t}\end{bmatrix} \mathbf{X} \tag{4.13}$$

where $\mathbf{R}$ and $\mathbf{t}$ are respectively the rotation matrix and the translation vecot that bring the world coordinate system to the camera coordinate system [Zha00].

The intrinsic parameters provide a model of the camera geometry and a distortion model of the lenses, described respectively by the calibration matrix $K$ and a distortion vector $d$.

Let $\mathbf{x}$ be the 2D image coordinates of a 3D point $\mathbf{X}$ , the relation between them can be expressed as:

$$\mathbf{x} = \mathbf{K} \begin{bmatrix}\mathbf{R} & \mathbf{t}\end{bmatrix} \mathbf{X} \tag{4.14}$$

where $\mathbf{K}$ is the intrinsic matrix of the camera,

$$\mathbf{K} = \begin{bmatrix} f_x & 0 & c_x \\ 0 & f_y & c_y \\ 0 & 0 & 1 \end{bmatrix} \tag{4.15}$$

with $(c_x, c_y)$ and $(f_x, f_y)$ being respectively the coordinates of the principal point and the focal length of the camera in the x-axis and y-axis [Zha00].

Following the classical approach of Zhang [Zha00], a chessboard with known square size is presented to the microscope cameras in different poses. An appropriate algorithm locates the corners in each frame and, given that a sufficient the number of poses is provided, infers the intrinsic and extrinsic parameters of the camera.

Once both cameras are calibrated it is possible to perform stereo calibration with a similar procedure, which aims at retrieving the transform between the right and left camera coordinate systems.

Stereo calibration exploits the principles of epipolar geometry (Figure 4.19). Taken two images of the same scene from different point of views, for any given point in an image it is possible to compute a line on the other image, the epipolar line, where the corresponding point is constrained to lie.

The transform between the cameras composing the stereo system is directly related to the position of corresponding points in the left and right image planes. Taken a point $\mathbf{X}$ in the 3D world space, let $\mathbf{x}$ and $\mathbf{x}'$ be respectively its projection onto the left and right images, their relation is defined through the fundamental matrix $\mathbf{F}$ as follows:

$$\mathbf{x}'^T \mathbf{F} \mathbf{x} = 0 \tag{4.16}$$

In order to compute $\mathbf{F}$ a known pattern of points is shown to the stereo systems in different poses. The corresponding pairs of points in the images extracted from the two cameras are identified, and used to estimate $\mathbf{F}$.

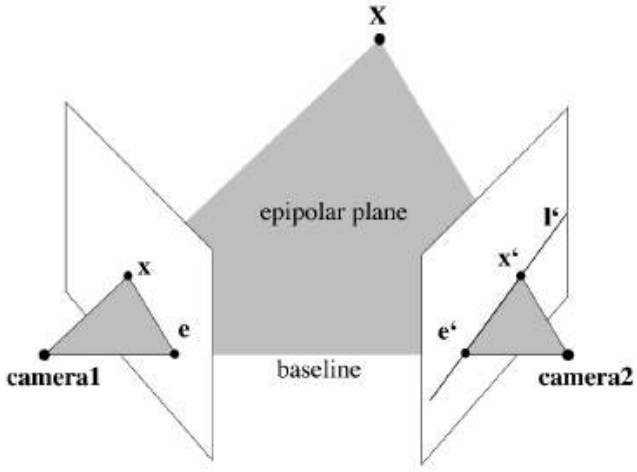


Figure 4.19: The projection of of a 3D point $X$ is imaged by two cameras, generating $x$ and $x'$. These projections are constrained to lie onto the epipolar plane.

Once the fundamental matrix is computed, it is possible to retrieve a single rotation matrix and a translation vector (also called baseline) that map the right camera coordinate system onto the left camera one in the real world.

After calibration the stereo system is fully described and, given that the combination of magnification and focal length of the cameras is not changed (thus keeping constant the estimated camera parameters), the stereo calibration can be used in order to identify the 3D positions of points identified by the stereo system.

In the presented system a well known focal length and magnification factor, i.e. an image acquisition setting, is always employed when reconstructing from the microscope, thus making a single stereo calibration sufficient for our purposes.

Future developments may require on-line reconstruction at different focal lengths and magnifications. In that case, to avoid the impractical need for multiple re-calibrations of the stereo system, an approach similar to the one presented in [JFRP14] can be exploited, enabling the estimation of the parameters for a wide different image acquisition settings from a limited number of stereo calibrations.

The implemented stereo camera calibration procedure is based on the open source C++ implementation that is available in the widely used OpenCV library [BK00].

#### 4.4.1.3 Stereo Reconstruction Pipeline

Any 3D point in the real space is projected to a unique pair of image points in an observing stereo camera system. As a consequence, given two images acquired from a stereo system, by identifying a pair of image locations representing a real world point, the three-dimensional location of that point can be determined [BBH03]. By repeating this procedure for a number of points related to the same real-world object, a 3D surface can be computed.

In the following paragraphs, the main steps that compose the developed stereo reconstruction pipeline are briefly described.

**4.4.1.3.1 Stereo matching** As a first step the correspondences between pixels of the left image and those belonging to the right image have to be found. This problem is solved through appropriate stereo matching algorithms.

Stereo matching is the process of identifying matching pixels in stereo image pairs, with the final objective of computing their real world 3D positions [KK16].

As already mentioned in the previous section, corresponding points are constrained to lie on epipolar lines in a stereo image pair. A preliminary step in typical stereo matching algorithms is represented by an image transformation process called rectifications. Thanks to the rectification process, both images are transformed so that corresponding epipolar lines become straight and lie in the same row.

After rectification, the 2D projections of a 3D point lies within the same row in the stereo camera images. The distance between these points in the two images is called disparity. Stereo matching algorithms can take advantage of the image rectification by limiting the research of disparities along a single row, thus making the research problem one dimensional.

A disparity map of an image consists of the disparities computed for all the pixels for which a corresponding one was found. Occlusions and textureless regions are common cause of void areas in disparity maps.

Several algorithms exist that attempt to compute disparity maps given a stereo pair in input. They can be generally divided into two main classes: a) local algorithms and b) global algorithms. [KK16].

- Local algorithms compute disparity for each pixel in the image on the basis of the intensity values that are found in its surroundings in the other image. They are usually efficient, at the price of being susceptible to occlusions and textureless areas in the images. Block Matching, gradient based and feature matching approaches [KK16] belong to this class.
- Global algorithms are less susceptible to ambiguous areas, since they usually rely on the minimizaztion of an energy function over the images - or just over rows in semi-global

approaches. Techniques like dynamic programming, graph cut, and belief propagation methods are exploited in global and semi-global algorithms for function minimization. [KK16].

Local algorithms are suitable for application in the proposed application due to the following considerations:

- Occlusion should not occur in out application since a view of the brain surface is acquired, after instructing the surgeon to remove any surgical tool before acquisition.
- Textureless area shouldn't be common, since the brain usually presents a very distinctive patten thanks to innervation and vascularization.
- Even if not required, higher efficiency is a nice-to-have feature, especially for future developments toward a continuous reconstruction of a the microscope stereo stream.

Among local algorithms, simple block matching approaches have already been shown to be adequate in the task of stereo matching when applied to surgical microscope images of the brain [KMP+15] [FDSJ01], and have been therefore selected for application in the developed pipeline. Among the different metrics that can be employed in block matching techniques, Sum of Absolute Differences (SAD) and Normalized Cross-correlation Coefficient (NCC) have been implemented and tested in our approach, starting from the open source Block Matching (BM) implementation available in the OpenCV library [BK00].

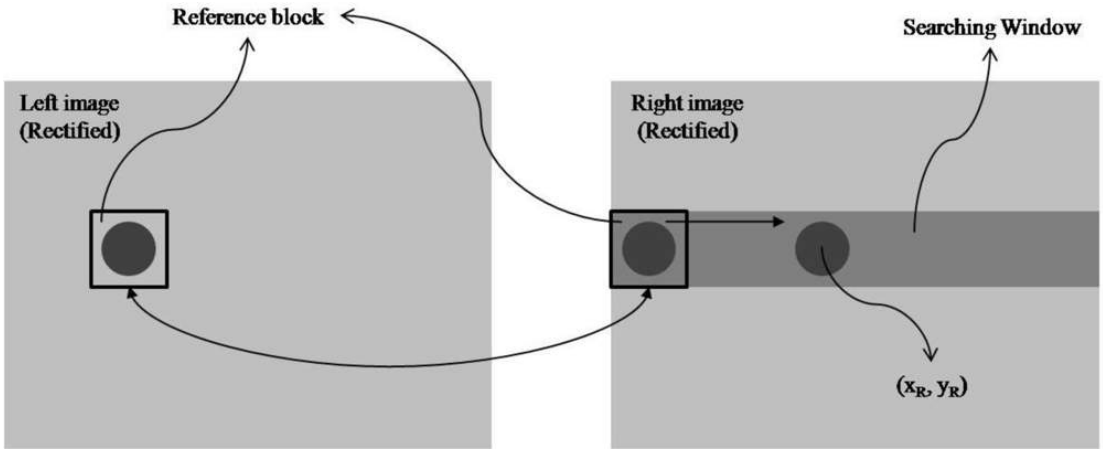


Figure 4.20: Scheme of a block matching approach for disparity map computation. From [CLH11]

Given the reference block $R$ and the target block $T$ of equal size $n \times n$ ($n = 31$ in our implementation), SAD is computed as:

$$SAD = \sum_{i=1}^{n} \sum_{j=1}^{n} |T(i,j) - R(i,j)|$$

while NCC is computed as:

$$NCC = \frac{\sum_{i=1}^{n} \sum_{j=1}^{n} (T(i,j) * R(i,j))}{\sqrt{\sum_{i=1}^{n} \sum_{j=1}^{n} T(i,j)^2 * \sum_{i=1}^{n} \sum_{j=1}^{n} R(i,j)^2}}$$

In the block matching approach (see Figure 4.20), given a reference block in the rectified left image centered at $(x_l, y_l)$ the chosen metric is computed for those target blocks on the rectified right image which are centered on the same scanline (i.e. centered in pixels $(x_r, y_r)$ with $y_r = y_l$. The block centered at $(x'_r, y_r)$ which minimizes the error metric, as in SAD-based block matching, or maximize the similarity metric, as in NCC-based block matching, is chosen, and the disparity for the pixel $(x, y)$ is set to:

$$d_{x,y} = x_l - x'_r$$

In the employed implementation of the SAD-based block matching, an additional threshold $\beta$ ($\beta = 15$ in the experiments reported in Section 4.4.3) allows us to filter out disparities that are generated from ambiguous matches. The condition on $d$ is imposed so that :

$$SAD(d) \geq SAD(d') * (1 + \beta/100)$$

where $d$ and $d'$ are respectively the selected disparity and the next-best disparity, and $SAD(d)$ is the computed *SAD* for blocks at disparity $d$.

In our implementation of the NCC-based block matching an additional threshold $\alpha$ has been set ($\alpha = 0.85$ in the experiments reported in Section 4.4.3) that filters out the disparities that were chosen with lower than $\alpha$ NCC value on matching blocks. A selected disparity $d$ is chosen only if

$$NCC(d) \geq \alpha$$

where $NCC(d)$ is the computed *NCC* for blocks at disparity $d$.

In addition to the aforementioned block matching approach, the Efficient Large Scale Stereo (ELAS) method described in [GRU10], has been integrated and compared to the mentioned block matching approaches.

ELAS is designed to be suitable for fast matching of high-resolution images and it is capable of estimate automatically disparity, thus making it suitable for application to microscopic approaches.

An open source implementation of ELAS is available on the official website of the project[11] and has been integrated in the developed software modules for stereo matching.

Briefly, ELAS consists in the following steps:

- A set of robustly matched features, the support points, is computed;
- The support points are triangulated and used to create a 2D mesh;
- A prior of the remaining disparities is produced via a piecewise linear function considering the support points disparities and the triangulated mesh;
- The remaining disparities are computed exploiting the prior for disambiguation and speed-up purposes.

A detailed description of the ELAS method is out of the scope of this work, additional details can be found in [GRU10].

A preliminary comparison of the results obtained with the different implemented methods is presented in Section 4.4.3.

**4.4.1.3.2 Disparity map refinement** The assumption is made that the disparity should be smooth, since the object to be reconstructed is the brain surface and obstructions should not be an issue in the proposed usage of the system. In order to enforce this smoothness constraint some additional filtering steps are applied to the disparity map:

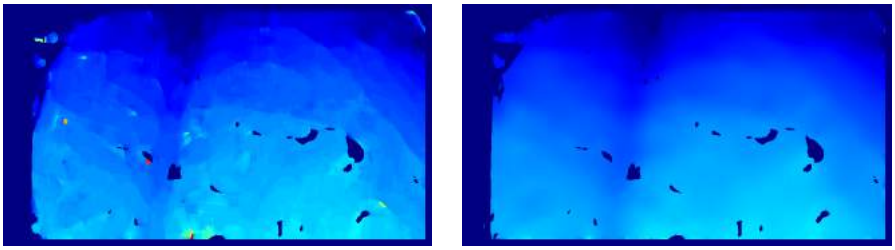

(a) Raw disparity map. (b) Smoothed disparity map.

Figure 4.21: Disparity map refinement

- A median filter is applied to the areas of the disparity map which exhibit larger standard deviations (i.e. non homogeneous areas, which can be corrupted by salt-and-pepper type noise). Given the mean $\mu$ and the standard deviation $\sigma$ of the intensities of the pixels in a $n \times n$ window, median filter is only applied to pixels that exhibit an intensity value $v$ for which $v \geq \mu + \alpha * \sigma$, where $\alpha$ is a configurable parameter, $\alpha = 2.5$ in our implementation;

[11] www.cvlibs.net/software/libelas/

- A mean filter is applied through a moving window to the whole image (considering only valid disparities) in order to further smooth the result, a $9 \times 9$ window is employed for the filter in our implementation;
- Histogram analysis is performed in order to discard outliers, defined as pixels that still exhibit rare disparity values (i.e. values that have low frequency in the histogram, as in small background or foreground objects). The minimum number of occurrences of a disparity value is set to 20 in our implementation.

**4.4.1.3.3 Point cloud computation** Given that the originating stereo system has been calibrated, the 3D position of the points in the disparity map can be computed, thus generating a 3D point cloud.

Let $T_x$ , $f$, $c_x$ and $c_y$ be respectively the baseline, the focal length and the x and y coordinates of the principal point in the left camera and let $c'_x$ be the principal point x coordinate in the right image. Points in the image can be reprojected into 3D coordinates thanks to the reprojection matrix $\mathbf{Q}$ [BK08]:

$$\mathbf{Q} = \begin{bmatrix} 1 & 0 & 0 & -c_x \\ 0 & 1 & 0 & -c_y \\ 0 & 0 & 0 & f \\ 0 & 0 & -\frac{1}{T_x} & \frac{(c_x - c'_x)}{T_x} \end{bmatrix} \tag{4.17}$$

Given a two-dimensional homogeneous point of coordinates $(x,y)$ for which a disparity $d$ was computed, we can project it in 3D using:

$$\begin{bmatrix} X \\ Y \\ Z \\ W \end{bmatrix} = \mathbf{Q} \begin{bmatrix} x \\ y \\ d \\ 1 \end{bmatrix} \tag{4.18}$$

The final three-dimensional will be $(X/W, Y/W, Z/W)$.

As shown in 4.19, the depth $Z$ of any 3D point is inversely proportional to its disparity.

$$Z = -\frac{T_x f}{d - (c_x - c'_x)} \tag{4.19}$$

**4.4.1.3.4 Outlier removal** As already mentioned, the assumption is made that the surface to be reconstructed should be smooth, given that it represents a magnified portion of a human brain

without occlusions. Exploiting this assumption, post-processing can be employed in order to further filter out stereo matching failures.

Once the physical coordinates of all of the points have been computed noisy measurement are removed from the dataset with the statistical filtering approach proposed in [RMB+08].

For each point, the mean distance to its $k$ nearest neighbors is computed. Then, the mean $\mu$ and standard deviation $\sigma$ of all of the previously computed distances (i.e. the whole set of mean distances computed for the entire input point cloud) are calculated and used to define a global threshold as $\mu \pm \alpha * \sigma$. The value of $\alpha$ being a configurable parameter. In our implementation, we set $\alpha = 0.7$ and $k = 90$.

The described outlier removal approach has been integrated in the proposed stereo image processing pipeline exploiting the open source implementation available in the Point Cloud Library (PCL) library [RC11].

**4.4.1.3.5 Mesh generation** A 2D-Delaunay triangulation[LS80] is exploited to build a topological mesh from the set of 3D points composing the obtained point cloud.

The 2D-Delaunay triangulation makes the assumption that no points of the dataset should lie inside the circumcircle of any triangle of the mesh and construct triangles in the x-y plane only.

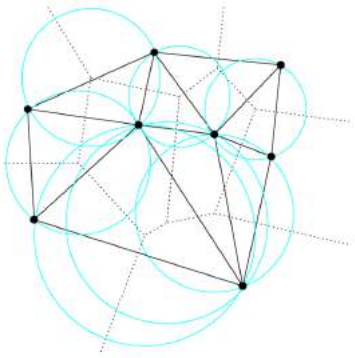

Figure 4.22: Example of Delaunay triangulation (black lines), no points lie in the circumcircles (in blue) of the triangles. From [VS08]

Since this triangulation process ignores the z-coordinate of the points (which is preserved in the reconstructed mesh), it may be suitable for robust 3D reconstruction of continuous surfaces imaged through stereo camera systems, presenting no obstructions in the line of sight.

2D-Delaunay triangulation has been integrated in the proposed stereo image processing pipeline exloiting the open source implementation available in the VTK library [SLM04].

**4.4.1.3.6 Mesh refinement** Some final post-processing filtering steps are applied to the computed mesh in order to improve the overall visual result. In particular after preliminary mesh subdivision [HDD+94], a laplacian filtering approach is employed to further improve the smoothness the obtained surface [VMM99] [LCS+17].

In Laplacian filtering, each vertex in the mesh is assigned to a new position which depends on the average position of neighboring vertices and on a parameter controlling the smoothing rate [VMM99].

The mentioned mesh post processing filters have been integrated in the proposed stereo image processing pipeline exloiting their open source implementation available in the VTK library [SLM04].

## 4.4.2 Microscope Tracking and Surface Localization

In order to fuse the reconstructed 3D surfaces with iUS data, it is necessary to track the microscope pose during the acquisition process.

This allows to reference the 3D reconstruction generated from the microscope in the same intraoperative space in which iUS images are acquired.

In order to reach this objective, the microscope is tracked using an EM sensor coupled with the same EMTS used to track US and to register the patient intraoperatively. The EMTS is integrated in the employed US system, namely an Esaote[12] MyLab Twice.

A custom API was made available by Esaote, in the scope of the FP7 TheraGlio European project, in order for the proposed software to automatically extract registered MRI and iUS from the mentioned US machine. In this way, the developed system has access to imaging data that is already referenced with respect to the EMTS transmitter frame of reference.

The usage of the same EMTS already exploited for the US machine allows to simplify the composition of the equipment in the operating room (meaning that no additional trolley is required). The possible limitation due to the cable length (from 2 up 3 meter) is avoided by placing the US system nearby the patient, which is possible since the probe, the microscope and the EMTS transmitter work in the same area inside the OR.

Since in the envisioned system the microscope needs to be tracked only in well-defined moments (i.e. when updated image fusion is needed), the sensor has been designed so that it can be attached on request, further reducing the impact of the approach on the standard surgical routine.

A reliable solution to attach the EM sensor to the microscope through a mechanical tool is proposed keeping into account the following basic requirements:

[12] www.esaote.com

(a) Upper part of the mechanical tool


(b) Overall mechanical tool

(c) Overview of the microscope from surgeon side

Figure 4.23: The proposed EM sensor mounting system for the surgical microscope

1. The sensor has to be attached to the microscope in a repeatable position to avoid the need for re-calibration;
2. Both the microscope and the sensor should be covered by a sterile sheath during the procedure;
3. The mounting system and the sensor should not interfere with the surgeon field of view;
4. The sensor has to be far enough to the main structure of microscope in order to avoid EM interference.

The proposed solution consists in a 3D-printed mounting system composed by two pieces that match together with high precision. One of the two components is fixed to the microscope head (Figure 4.23a) and can be wrapped by the standard sterile sheath designed for the microscope.

The second component matches with the previous one and is mechanically constrained to always be locked in exactly the same position and orientation (Figure 4.23b). The second component is sterilizable and can be attached to the first once the microscope is already covered by the sterile cover. In order to keep the two components together without mechanical stress, that could damage the sterile sheath, a neodymium magnet is used to keep the two pieces attached to each other.

The EM sensor can be attached to the second component of the mounting system at any moment with its own sterile sheath. Figure 4.23b and Figure 4.23c show the two parts attached to each other, with the sensor already inserted in the second piece. The cable of the sensor is directed away from the binoculars in order not to interfere with the microscope commands and/or surgeon and to be far from patient head.

#### 4.4.2.1 3D Reconstruction in the Intraoperative Space

Let the transform that maps 3D reconstruction space and the EMTS transmitter frame of reference be represented by the $\mathbf{T}_{\text{em}}^{\text{recons}}$ transformation matrix.

Two different transformation matrices have to be composed in order to obtain $\mathbf{T}_{\text{em}}^{\text{recons}}$ (Equation (4.20)).

$$\mathbf{T}_{\text{em}}^{\text{recons}} = \mathbf{T}_{\text{em}}^{\text{micro}}\,\mathbf{T}_{\text{micro}}^{\text{recons}} \tag{4.20}$$

- $\mathbf{T}_{\text{em}}^{\text{micro}}$, refers to the EM sensor pose - which is attached to the microscope head - with respect to the EMTS transmitter frame of reference.
- $\mathbf{T}_{\text{micro}}^{\text{recons}}$, refers to the 3D reconstructed space origin and orientation with respect to EM sensor space attached to microscope head.

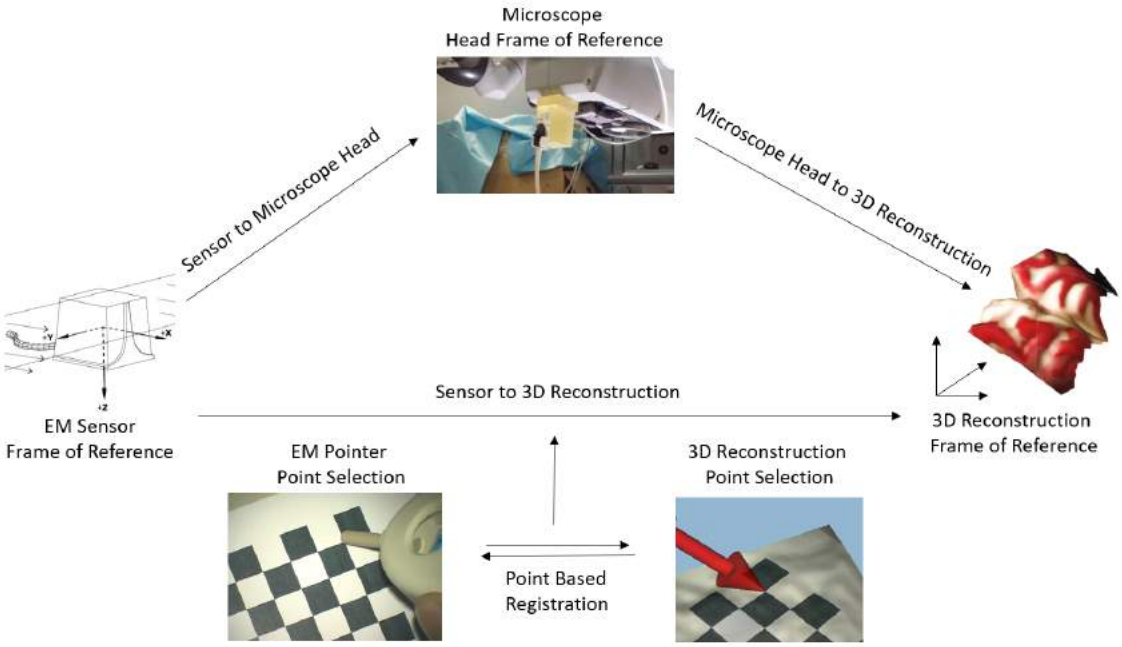


Figure 4.24: Transformations between the EMTS transmitter frame of reference and the reconstructed 3D space.

From eq. (4.20) the transform $\mathbf{T}_{\text{micro}}^{\text{recons}}$ can be written as follows:

$$\mathbf{T}_{\text{micro}}^{\text{recons}} = \mathbf{T}_{\text{micro}}^{\text{em}}\,\mathbf{T}_{\text{em}}^{\text{recons}} \tag{4.21}$$

The EMTS allows to directly obtain $\mathbf{T}_{\text{micro}}^{\text{em}}$ by providing sensor position and orientation, but $\mathbf{T}_{\text{em}}^{\text{recons}}$ needs further steps to be computed, following a dedicated calibration procedure (Figure 4.24).

In the adopted calibration procedure, a checkerboard pattern is captured by the microscope cameras and reconstructed using the previously described techniques (Figure 4.25a).

The calibration procedure can be broken down into the following steps:

- Stereo acquisition and 3D reconstruction of a checkerboard pattern with known geometry.
- Automatic selection of a set of points in the reconstructed 3D camera space.
- Manual selection of the same points in the EMTS transmitter frame of reference by means of a calibrated EM pointer .

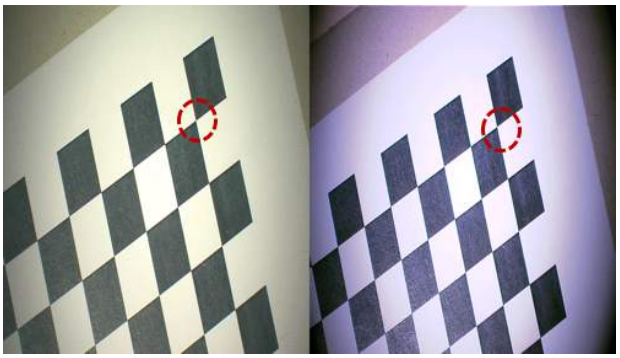

(a) Selected corner.

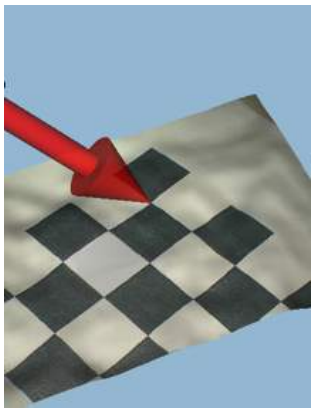

(b) Corner in the 3D reconstruction space.

(c) Corner acquisition in the EMTS frame of reference by means of an EM pointer

Figure 4.25: Main steps of the calibration procedure of the EMTS sensor position.

Once the two sets of corners are found, the current transform $\mathbf{T}_{em}^{recons}$ can be found by minimizing the distance between the pairs of corresponding points. Through the current value of $\mathbf{T}_{em}^{recons}$, $\mathbf{T}_{micro}^{recons}$ can be computed following eq. (4.21). $\mathbf{T}_{micro}^{recons}$ does not depend on microscope position, and it needs to be calculated only if the sensor attached to the surgical microscope head is relocated.

Since $\mathbf{T}_{micro}^{recons}$ is now known and $\mathbf{T}_{micro}^{em}$ is continuously computed by the EMTS, all the elements of Equation (4.20) are available during the procedure and the 3D reconstructed surface can be brought in the EMTS transmitter reference frame, thus enabling image fusion with the other datasets which are referenced in the same space.

### 4.4.3 Results

A system was developed in the scope of this work that performs real-time fusion in a virtual 3D scene of iUS and other preoperative imaging modalities together with intraoperative surgical microscope imaging data. The microscope images are transformed into 3D surfaces thanks to a stereo-reconstruction pipeline.

Microscope tracking allows for automatic localization in the intraoperative space of the reconstructed surfaces, which can then be fused with other imaging modalities in an "augmented virtuality" setting where the entire imaging set can be explored from the viewpoint of the surgeon.

In the envisioned use case of the system, whenever the surgeon wants to explore previously acquired iUS (or other preoperative data), a snapshot of the current field of view of the microscope, representing the portion of brain surface he is currently operating on, can be captured and reconstructed. iUS can then be navigated in a realistic 3D scene - which comprises the 3D reconstruction of the brain surface - of immediate comprehension for the surgeon.

In this section, a preliminary assessment of different components of the developed system will be presented.

#### 4.4.3.1 Reconstruction and Localization from the Surgical Microscope Assessment

The stereo image processing pipeline which has been described in Section 4.4.1, combined with the microscope tracking and surface localization strategy described in Section 4.4.2 have been applied to a Zeiss[13] Pentero 900 surgical microscope which was available at the Neurologic Institute C. Besta (Figure 4.26).

The described acquisition pipeline is employed in order to acquire calibration images from the Zeiss Pentero 900 surgical microscope.

[13] www.zeiss.com

Figure 4.26: Experimental setup: the brain phantom is placed under the Pentero 900 surgical microscope, which is connected to the Trenion 3D HD system.

A zoom factor of 2.5x and a fixed focal length of 375mm have been selected in the experiment, suitable for capturing a large enough view of the surgical field to be appreciated when fused with iUS (i.e. it should at least be possible to identify where the US probe was placed on the brain surface). While this field of view may be larger than the one usually employed during the surgical procedure, it should be remembered that in the envisioned system stereo image pairs are acquired only when image navigation and fusion is needed. In those cases it is reasonable to require the surgeon to temporarily reduce the zoom factor on the microscope in order to acquire a more comprehensive representation of the surgical field.

A small calibration pattern consisting of a checkerboard (each square of the checkerboard measuring 2.5 mm) has been exploited to perform a standard stereo-calibration procedure. After calibration, the reprojection error is provided as a measure of its accuracy. Additionally, the estimated square length of the checkerboard pattern is computed on the calibration images (i.e. computing the checkerboard corner 3D position from the employed image pairs via the obtained stereo calibration).

Overall, the application of the stereo calibration to the stereo microscope gives satisfying results, as shown by the low reprojection error and by the estimated square length which is close to the nominal value (details in Table 4.1).

A simple phantom composed by a plastic model resembling the shape and size of a human brain was used in order to evaluate the stereo-reconstruction pipeline after stereo calibration. Stereo

| **Pentero 900 Stereo Calibration** | |
|---|---|
| Number of images | 121 |
| Image resolution | 960 $\times$ 540 pixel |
| Stereo Reprojection Error | 0.23 pixel |
| Real square length | 2.5 mm |
| Estimated square length (average) | 2.52 mm |
| Estimated square length (standard deviation) | 0.03 mm |

Table 4.1: Stereo calibration details and results for the Pentero 900 surgical microscope.

images of the phantom have been acquired, rectified (Figure 4.27), and used to compute a disparity map.

(a) Acquired stereo pair. (b) Rectified left view. (c) Rectified right view.

Figure 4.27: Splitting and rectification of the acquired stereo pair.

Three algorithms have been compared, the SAD-based block matching, the NCC-based block matching, and the ELAS approach (see Section 4.4.1.3 for additional details).

SAD-based block matching suffered from intensities mismatch between the left and right images (an artifact introduced in the acquisition pipeline by the employed Trenion 3D HD System), resulting in a sparser disparity map after filtering. ELAS and NCC-block matching algorithms presented fewer undefined disparities, being less sensitive to intensity variations in the stereo pair.

(a) SAD-Block matching (b) NCC-Block matching (c) ELAS

Figure 4.28: Disparity maps comparison.

Accuracy of the stereo calibration and reconstruction pipeline has been further evaluated by

comparing the obtained 3D reconstructions of the phantom model with the one generated by a commercial infrared 3D scanner, namely the Sense 3D Scanner from 3D Systems[14], which has a nominal depth resolution under 1 mm at a 0.5 m scanning distance and can be considered as a Ground Truth (GT) for our application.

| | **SAD-BM** | **NCC-BM** | **ELAS** |
|---|---|---|---|
| Average distance | 0.8 mm | 1.1 mm | 1.5 mm |
| Minimum distance | 0.02 mm | 0.04 mm | 0.04 mm |
| Maximum distance | 8.2 mm | 19.4 mm | 16.1 mm |
| Standard deviation | 0.8 mm | 1.5 mm | 1.3 mm |

Table 4.2: Ground Truth and reconstructed surfaces comparison, average of 11 acquisitions from different point of views.

The two surfaces are first manually aligned to provide a rough initialization to an automatic registration algorithm, namely, the Iterative Closest Point (ICP) algorithm [BM92]. At this point, the distances between the surfaces are computed (Table 4.2).

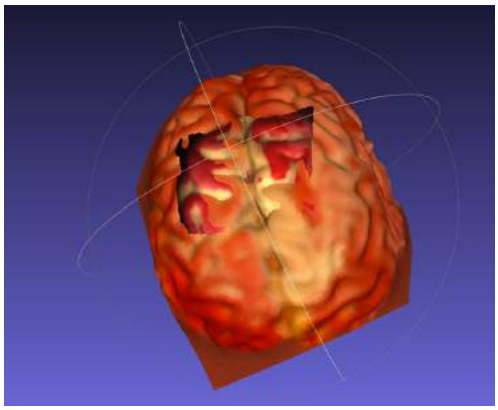

Figure 4.29: Ground Truth and reconstructed mesh, surface registration.

Accuracy of the tracking and localization pipeline that brings the reconstructed surface in the EMTS transmitter frame of reference is also quantitatively verified by exploiting the reconstruction of a known patterns of points. The positions of a checkerboard corners are acquired through a commercial EM tracked pointer (the calibration of which is known) and their position is compared to the one obtained via 3D reconstruction (Table 4.3) after the application of the transform pipeline defined in Section 4.4.2.

It should be noted that the system should provide reasonable accuracy to enable localization of the brain surface with respect to the manually positioned US probe, but its requirements in

[14] www.3dsystems.com

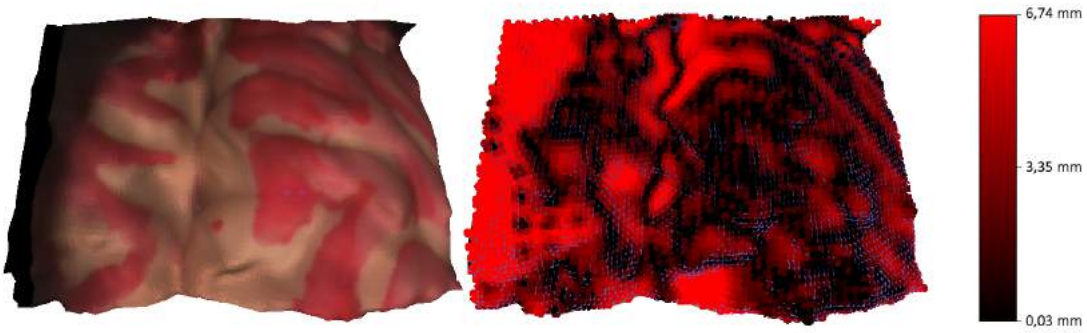


Figure 4.30: The obtained mesh (left) and a point cloud in which each vertex color is determined by its distance to the GT (right), where brighter areas correspond to further distances. Shadows and partial occlusions are the main causes of larger errors.

| Average distance | Standard deviation | Min distance | Max distance |
|---|---|---|---|
| 2.6 mm | 1.1 mm | 0.7 mm | 4.8 mm |

Table 4.3: Localization error, average of ten acquired points.

terms of reconstruction and localization accuracy aren't as strict as in other works that exploit reconstruction for quantitative measurement on brain displacement [KMP+14]. While an average error of 2.6 mm (Table 4.3) may be suitable for the current application (when compared to an average expected brain shift cortical displacement of 1 cm [Pat98]), it may be too high for future developments (e.g. precise brain shift estimation, fusion at higher magnifications) and improvements shall be foreseen in future developments.

#### 4.4.3.2 Multimodal Navigation and Fusion Assessment

Multimodal image navigation and fusion capabilities of the developed system were assessed through ex-vivo experiments on a bovine brain in a mockup setup.

In order to exploit ex-vivo tissue, which is currently not usable together with the surgical microscope located in the OR at Neurologic Institute C. Besta due to regulatory limits, a simpler stereo system has been employed in place of the surgical microscope, namely the 3D Minoru[15] camera (the acquisition setup is shown in Figure 4.31).

This simpler setup served as a proof of concept for the demonstration of the multimodal fusion capabilities of the system, while the applicability of the system to the microscope have already

[15] www.minoru3d.com

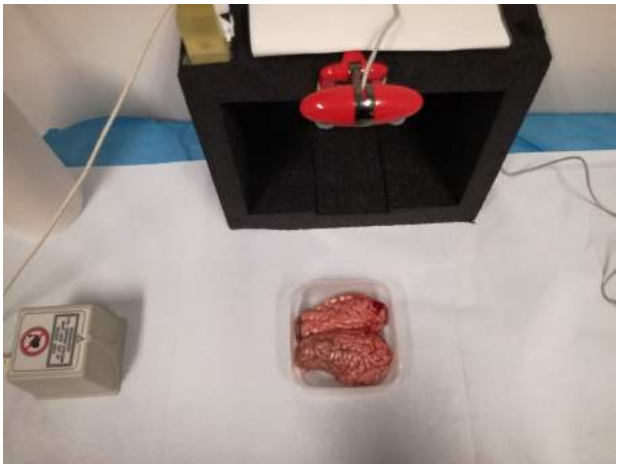

Figure 4.31: The experimental setup composed by the bovine brain phantom, the EMTS transmitter, and the 3D Minoru camera

been assessed in the previous section.

Calibration of the stereo camera involved in this experiment has been carried out with the same methods described in the previous section. Calibration details are resumed in Table 4.4.

| **3D Minoru Stereo Calibration** | |
|---|---|
| Number of images | 97 |
| Image resolution | 640 $\times$ 480 pixel |
| Stereo Reprojection Error | 0.71 pixel |
| Real square length | 10.00 mm |
| Estimated square length (average) | 9.99 mm |
| Estimated square length (standard deviation) | 0.14 mm |

Table 4.4: Stereo calibration details and results for the 3D Minoru camera.

Previously acquired MRI data (Table 4.5) of the phantom have been imported in the US machine, namely a MyLab Twice by Esaote[16]. The US machine enables intraoperative registration of MRI to iUS through manual landmark registration.

The developed navigation system communicates with the US machine thanks to a custom API that was made available by Esaote in the scope of the FP7 TheraGlio project. The API enables the software to access the available preoperative data and intraoperative US, together with the parameters related to their registration with respect to the EMTS (which is integrated in the MyLab

[16] www.esaote.com

| MRI Series | Image size | Slice Thickness | Pixel Spacing |
|---|---|---|---|
| 3D SST1 Isotropic | 512x512 | 0.430 mm | 0.429 mm / 0.429 mm |
| FSE T2 | 512x512 | 3 mm | 0.488 mm / 0.488 mm |
| GE T2 FC | 256x256 | 4 mm | 0.976 mm/ 0.976 mm |

Table 4.5: MRI acquisitions details.

Twice for US/MRI navigation purposes). This feature enable effective and efficient integration of the developed system with the commercial US machine.

In Figure 4.32 a freehand 3D US acquisition acquired by the US machine is imported and blended in a 3D scene that comprehends the surface reconstruction of the phantom. It should be noted that the black background which is visible around the US in Figure 4.32 and Figure 4.34 is an artifact generated by the freehand 3D US reconstruction process. Such an artifact could be easily filtered out in future developments, by only showing valid US voxels in the 3D scene (i.e. voxels with greater than zero intensities) .

The virtual 3D scene is interactive and allows the exploration of the fused data by changing the position and orientation of the shown US/MRI slices, along with the blending level among the different modalities in order to visualize the internal structures of the brain from arbitrary viewpoints.

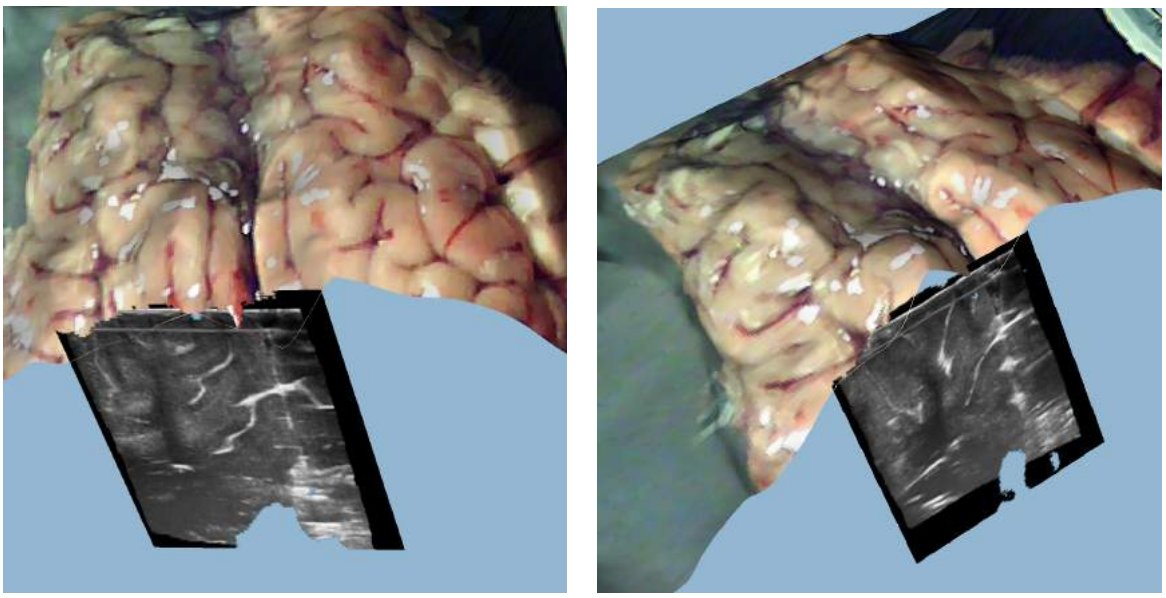

Figure 4.32: Fusion between US and phantom reconstructed surface. The black background around US is an artifact generated by the 3D US volume reconstruction process.

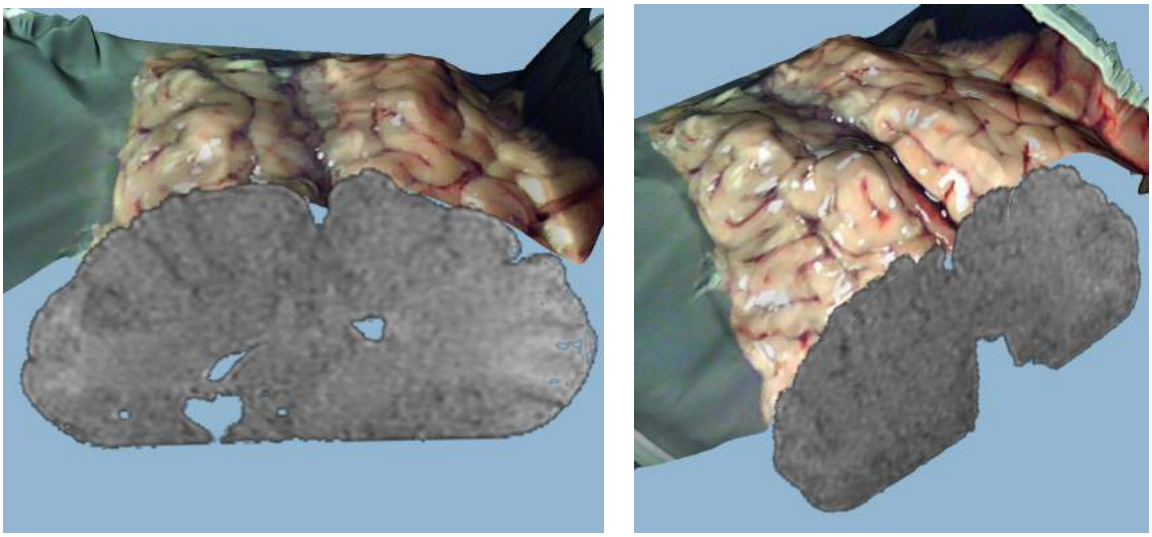

Figure 4.33: Fusion between MRI and phantom reconstructed surface. A segmentation of the MRI is employed to only show informative areas of the phantom in the 3D scene.

Figure 4.32 and Figure 4.33 show how the developed system can be applied to obtain a comprehensive representation of the different kinds of available intraoperative and preoperative data. In order to enhance the 3D visualization, a segmentation of the phantom, obtained from the available MRI volume, is also provided, and it is employed to mask the MRI in the 3D scene (transparent areas in the MRI which are visible in Figure 4.33 are due to air bubbles in the phantom which were excluded by the provided segmentation).

A mismatch between the segmented MRI and the reconstructed surface is visible in Figure 4.33. This mismatch may be due to changes in the phantom shape since the MRI acquisition and to stereo reconstruction and localization errors, which are aggravated by the employed low resolution stereo camera. For these reasons the scope of this experimental setup is limited to the assessment of the navigation and fusion capabilities of the developed system, while the accuracy of the stereo reconstruction and localization process was evaluated in the previous section.

Since the position of the microscope is known (thanks to the employed EMTS) the scene can also be shown from its point of view, in order to provide an augmented virtuality environment that exactly maps to the surgeon field of view during the procedure (Figure 4.34).

Figure 4.34: Fusion between US (left) or MRI (right) and phantom reconstructed surface. Camera point of view.

## 4.5 Discussion

Despite some clear advantages that iUS can bring to neurosurgical practice and in particular to neurosurgical glioma resection procedures [SMS00] [PAV+15] [PVF+14], adoption of this technology in the neurosurgical community is still hampered by several challenges. In particular, iUS is a technology that a) can be mastered only after a steep learning curve, b) suffers from large inter-operator variability and c) produces unconventional images compared to other imaging systems.

A novel simulation platform has been proposed in Section 4.3, which exploits offline multimodal image naviagtion and fusion in order to facilitate the learning process of trainees and surgeons with fewer experience in the intraoperative usage of US. Differently from other state of the art approach [MMH+14], the developed application is focused on a) portability, requiring minimal hardware to be used, and b) image fidelity, relying only on original iUS images acquired during surgical procedures. Validation during neurosurgical training courses showed the potential of such a system as a simple but effective training instrument.

In order to further enhance intraoperative image fusion, with the final objective of improving interpretability of iUS, an image navigation system capable of integrating surgical microscope images, iUS and preoperative data was described in Section 4.4. Differently from other approaches [PFJ05] [KMP+15], the proposed system is focused on iUS fusion, and it is integrated with a

commercial US machine. Exploiting the US machine internal EMTS, integration with current surgical routine is simplified. Such a system was preliminary tested through phantom and ex-vivo tests showing promising results.

Future developments of the proposed systems are envisioned, including:

- Further improvements and experimental validation: despite the promising preliminary results, the developed techniques for stereo images reconstruction and localization need further testing and assessment on the surgical microscope. Ex-vivo and in-vivo tests are expected to happen in the near future, and they will hopefully provide further evidence on the accuracy, usability and potential integration in the surgical routine of the system.

  While the obtained results may be adequate for visualization-only purposes, the current accuracy can be insufficient for further advanced developments of the system (e.g. integrating brain shift quantification functionalities, as in [KMP+14] [PMJ09]) and should be further improved. Switching from an EMTS to an OTS will be considered, evaluating the trade-off between higher tracking accuracy and harder integration with surgical routine.

  Moreover, usability of the currently developed navigation system can be improved by injecting registered iUS information directly into the microscope eyepieces, with the final objective of realizing augmented reality for the surgeon during the procedure in a similar approach to the ones proposed in [KEMJ+00] and [AWR+03].

- iUS simulation enhancement: after validation of the described surgical microscope stereo reconstruction and localization techniques, a foreseen step will be represented by the addition of the obtained stereo microscope reconstructions in the proposed simulation platform. Integration of this additional piece of intraoperative information will enhance the simulation environment, making it even more realistic and immersive, thus hopefully increasing its efficacy as a training instrument.

# 5 Conclusions

Drastic changes are expecting surgery in the coming years. We are assisting at a technological revolution that is spreading through multiple scientific and technological fields. The rising number of real-life robotic, computer vision and machine learning applications is changing the way we see autonomous machines, making them gradually more accepted into our daily routine. As this innovation process proceeds forward, surgery will be just one of the many aspects of life that will be revolutionized.

A multitude of approaches are being developed by the scientific community in most of the surgical fields and especially in the ones that can exploit imaging systems to guide complex procedures. Research is focusing on a broad range of topics related to IGS, including more accurate intraoperative imaging systems and tools, novel approaches for carrying out minimally invasive procedures and advanced algorithms and techniques to enhance the existing systems capabilities in guiding surgeons during critical tasks.

It is safe to state that the innovations that have been applied so far to the surgical field are just a drop in the ocean with respect to what recent scientific and technological advancements will enable in the very next future.

Any new application in surgery has to face issues that should not be overlooked, since they often cause clinical practice to resist to innovations, thus lagging behind with respect to the most advanced approaches already experimented and validated in research centers.

- Novel procedures may require levels of dexterity, speed and precision that are beyond the reach of average surgeons. Moreover, they may be suitable for treating just a limited number of clinical cases.
- Novel instruments and techniques may be hard to master for surgeons. Steep learning curves may hamper the adoption of promising approaches, due to the limited amount of time that surgeon can spend by training and to the difficulties in integrating them into existing procedures.

These issues require different but interconnected approaches:

- When surgeon skills do not suffice for performing complex procedures, IGS applications should come in help. Robotic and artificial intelligence solutions should be researched and developed to eventually reach the point in which human intervention will not be needed anymore during surgery;

- Instruments should be put in place in order to help surgeons in the process of understanding and learning to use techniques that have been proven effective but are still uncommon in clinical practice. This comprehends the development of methods for enhancing the available imaging data in order to make them more comprehensible and informative during surgery, or the realization of better simulation environments for trainees and less experienced surgeons.

Both approaches actively contribute to modernization of surgery in a virtuous circle. The first one provides long term vision toward applicability of potentially disruptive technologies, while making available innovative elements developed as part of larger systems. The second one focuses on smaller but continuous and tangible improvements to daily clinical routine, a necessary step to increase clinicians' trust in high-tech solutions and prepare a fertile ground for higher impact solutions.

This thesis tried to tackle existing open problems following both of the aforementioned approaches, focusing in particular on the role and impact of intraoperative navigation systems in image guided application. Original contributions to the current state of the art have been provided by proposing novel applications in two different IGS scenarios that share the need of researching novel methods to fully exploit iUS for efficient and effective surgical guidance.

The first part of this work focused on the surgical scenario of minimally invasive thermal ablation through USgHIFU. A novel robotic platform for HIFU therapy was presented, which exploits US probes mounted on robotic arms to provide a flexible solution which may be applicable to a number of tumor ablation scenarios.

A novel strategy for motion compensation in USgHIFU therapy was proposed, comprehending integration of computer vision and machine learning techniques into the navigation system of the robotic platform to enable continuous therapy guidance based on iUS information. The platform capabilities and the motion compensation strategy accuracy have been validated through ex-vivo experiments on phantoms.

The second part of this work focused on the surgical setting of iUS-guided neurosurgical glioma resection. A novel application designed and developed to help surgeons understand iUS information was proposed, which exploits registered iUS and MRI patient data in an image navigation system that enables offline simulation and rehearsal of iUS exams. Such an application has been validated during neurosurgery training courses, showing how it could be used as an effective and portable solution for training of neurosurgeons which are not familiar with iUS imaging.

Additionally, an approach for enabling fusion between iUS and stereo microscopy in image navigation systems was proposed and implemented exploiting computer vision techniques. Preliminary evaluation of the accuracy of the proposed approach has been assessed and its applicability as a tool for aiding iUS comprehension, both during surgery or in simulated environments, has been confirmed through in-vitro and ex-vivo experiments on phantoms.

## 5.1 Future Work

The foreseen natural developments of the presented research work have been described in detail in the previous chapters. They can be summarized by identifying two main directions of work, which are:

- Validation of the presented applications to extend, enable or bring closer their clinical usage. In-vivo experimental tests should be performed, in order to validate the usability of the developed image navigation systems and evaluate their natural place into surgical routine.
- Addition of advanced feature to the developed image navigation systems in order to increase the informative content they can provide, their accuracy and their reliability. State of the art image processing, machine learning and computer vision techniques can be exploited to reach this objective.

The first direction serves the purpose of providing real life solutions to the medical community, proceeding further into the process of making available in practice what have been demonstrated as effective in theory. This short-to-mid term objective is a fundamental step, which should help to rethink and finalize the developed systems focusing on their flawless integration with existing procedures and tools.

The second direction should aim not only at refining and enhancing the existing system, improving their overall performance, but also at enabling new innovative surgical paths, now precluded due to the still missing information pieces which are necessary for providing surgical guidance to humans or robotic platforms. This mid-to-long term objective should be the real driver of innovation, contributing to the unstoppable technological revolution of the surgical field.

All of the possible directions of future work in this field converge to a common objective: bridging the gap between advanced solutions and clinical practice, and finally improving safety, efficiency and overall outcome of surgical procedures.

Thanks to this relentless innovation process, the days in which intraoperative image navigation systems will guide fully autonomous surgical procedures may be closer than we think.

# Bibliography


[ADB+15] Dan E Azagury, Monica M Dua, James C Barrese, Jaimie M Henderson, Nicolas C Buchs, Frederic Ris, Jordan M Cloyd, John B Martinie, Sharif Razzaque, Stéphane Nicolau, et al. Image-guided surgery. *Current problems in surgery*, 52(12):476–520, 2015. [Cited on pages 7, 8, 9, 19, and 20.]

[Adl93] John R Adler. Apparatus for and method of performing stereotaxic surgery, May 4 1993. US Patent 5,207,223. [Cited on page 8.]

[AHH+09] Paul Aljabar, Rolf A Heckemann, Alexander Hammers, Joseph V Hajnal, and Daniel Rueckert. Multi-atlas based segmentation of brain images: atlas selection and its effect on accuracy. *Neuroimage*, 46(3):726–738, 2009. [Cited on page 24.]

[APV+12] V. Auboiroux, L. Petrusca, M. Viallon, T. Goget, C.D. Becker, and R. Salomir. Ultrasonography-based 2d motion-compensated hifu sonication integrated with reference-free mr temperature monitoring: a feasibility study ex vivo. *Physics in medicine and biology*, 57(10):N159, 2012. [Cited on page 43.]

[ASB04] B Albayrak, AF Samdani, and PM Black. Intra-operative magnetic resonance imaging in neurosurgery. *Acta neurochirurgica*, 146(6):543–557, 2004. [Cited on page 14.]

[AT16] Jean-François Aubry and Mickael Tanter. Mr-guided transcranial focused ultrasound. In *Therapeutic Ultrasound*, pages 97–111. Springer, 2016. [Cited on page 36.]

[AvSSC08] Adrian Andronache, Martin von Siebenthal, Gábor Székely, and Ph Cattin. Non-rigid registration of multi-modal images using both mutual information and cross-correlation. *Medical image analysis*, 12(1):3–15, 2008. [Cited on page 23.]

[AWR+03] M Aschke, CR Wirtz, J Raczkowsky, H Worn, and S Kunze. Augmented reality in operating microscopes for neurosurgical interventions. In *Neural engineering, 2003. Conference Proceedings. First international IEEE EMBS conference on*, pages 652–655. IEEE, 2003. [Cited on page 113.]

[BBB04] Sofiane Brahim-Belhouari and Amine Bermak. Gaussian process for nonstationary time series prediction. *Computational Statistics & Data Analysis*, 47(4):705–712, 2004. [Cited on page 53.]

[BBdB+16] PTS Borman, C Bos, T de Boorder, BW Raaymakers, CTW Moonen, and SPM Crijns. Towards real-time thermometry using simultaneous multislice mri. *Physics in medicine and biology*, 61(17):N461, 2016. [Cited on page 33.]

[BBH03] Myron Z Brown, Darius Burschka, and Gregory D Hager. Advances in computational stereo. *IEEE transactions on pattern analysis and machine intelligence*, 25(8):993–1008, 2003. [Cited on page 93.]

[BCE+08] Dean C Barratt, Carolyn SK Chan, Philip J Edwards, Graeme P Penney, Mike Slomczykowski, Timothy J Carter, and David J Hawkes. Instantiation and registration of statistical shape models of the femur and pelvis using 3d ultrasound imaging. *Medical image analysis*, 12(3):358–374, 2008. [Cited on page 25.]

[Ben00] Yoshua Bengio. Gradient-based optimization of hyperparameters. *Neural computation*, 12(8):1889–1900, 2000. [Cited on page 54.]

[BK00] Gary Bradski and Adrian Kaehler. Opencv. *Dr. Dobb's journal of software tools*, 3, 2000. [Cited on pages 92 and 94.]

[BK08] Gary Bradski and Adrian Kaehler. *Learning OpenCV: Computer vision with the OpenCV library*. " O'Reilly Media, Inc.", 2008. [Cited on page 97.]

[BKK+16] Muyinatu A Lediju Bell, Shalki Kumar, Lily Kuo, H Tutkun Sen, Iulian Iordachita, and Peter Kazanzides. Toward standardized acoustic radiation force (arf)-based ultrasound elasticity measurements with robotic force control. *IEEE Transactions on Biomedical Engineering*, 63(7):1517–1524, 2016. [Cited on pages 47 and 59.]

[BKS+03] MR Bailey, VA Khokhlova, OA Sapozhnikov, SG Kargl, and LA Crum. Physical mechanisms of the therapeutic effect of ultrasound (a review). *Acoustical Physics*, 49(4):369–388, 2003. [Cited on page 29.]

[BM92] Paul J Besl and Neil D McKay. Method for registration of 3-d shapes. In *Sensor Fusion IV: Control Paradigms and Data Structures*, volume 1611, pages 586–607. International Society for Optics and Photonics, 1992. [Cited on page 107.]

[BMHL+14] Ronald Bauer, Ernst Martin, Stefan Haegele-Link, Georg Kaegi, Moritz von Specht, and Beat Werner. Noninvasive functional neurosurgery using transcranial mr imaging-guided focused ultrasound. *Parkinsonism & related disorders*, 20:S197–S199, 2014. [Cited on page 29.]

[Bra02] William G Bradley. Achieving gross total resection of brain tumors: intraoperative mr imaging can make a big difference. *American Journal of Neuroradiology*, 23(3):348–349, 2002. [Cited on page 67.]

[Buc95] Richard D Bucholz. System for indicating the position of a surgical probe within a head on an image of the head, January 24 1995. US Patent 5,383,454. [Cited on page 8.]

[C+96] National Research Council et al. *Mathematics and physics of emerging biomedical imaging*. National Academies Press, 1996. [Cited on page 12.]

[CD14] Katrina F Chu and Damian E Dupuy. Thermal ablation of tumours: biological mechanisms and advances in therapy. *Nature Reviews Cancer*, 14(3):199–208, 2014. [Cited on page 27.]

[CFK+14] Olivier Couture, Jessica Foley, Neal F Kassell, Benoit Larrat, and Jean-Francois Aubry. Review of ultrasound mediated drug delivery for cancer treatment: updates from pre-clinical studies. *Translational Cancer Research*, 3(5):494–511, 2014. [Cited on pages 29 and 64.]

[CHCV15] Alexander Copelan, Jason Hartman, Monzer Chehab, and Aradhana M Venkatesan. High-intensity focused ultrasound: current status for image-guided therapy. In *Seminars in interventional radiology*, volume 32, pages 398–415. Thieme Medical Publishers, 2015. [Cited on page 29.]

[CHMB12] Pierrick Coupé, Pierre Hellier, Xavier Morandi, and Christian Barillot. 3d rigid registration of intraoperative ultrasound and preoperative mr brain images based on hyperechogenic structures. *Journal of Biomedical Imaging*, 2012:1, 2012. [Cited on page 25.]

[CJ01] Gary E Christensen and Hans J Johnson. Consistent image registration. *IEEE transactions on medical imaging*, 20(7):568–582, 2001. [Cited on page 23.]

[CKM+82] William F Chandler, James E Knake, John E McGillicuddy, Kevin O Lillehei, and Terry M Silver. Intraoperative use of real-time ultrasonography in neurosurgery. *Journal of neurosurgery*, 57(2):157–163, 1982. [Cited on page 68.]

[CLH11] Mao-Hsiung Chiang, Hao-Ting Lin, and Chien-Lun Hou. Development of a stereo vision measurement system for a 3d three-axial pneumatic parallel mechanism robot arm. *Sensors*, 11(2):2257–2281, 2011. [Cited on page 94.]

[CLHM93] GN Collins, SN Lloyd, M Hehir, and GB McKelvie. Multiple transrectal ultrasound-guided prostatic biopsies—true morbidity and patient acceptance. *BJU International*, 71(4):460–463, 1993. [Cited on page 19.]

[CMD+15] A Cafarelli, M Mura, Alessandro Diodato, Andrea Schiappacasse, Matteo Santoro, Gastone Ciuti, and Arianna Menciassi. A computer-assisted robotic platform for focused ultrasound surgery: Assessment of high intensity focused

ultrasound delivery. In *Engineering in Medicine and Biology Society (EMBC), 2015 37th Annual International Conference of the IEEE*, pages 1311–1314. IEEE, 2015. [Cited on pages 5 and 28.]

[CNV+15] Laure-Anaïs Chanel, Florent Nageotte, Jonathan Vappou, Jianwen Luo, Loïc Cuvillon, and Michel de Mathelin. Robotized high intensity focused ultrasound (hifu) system for treatment of mobile organs using motion tracking by ultrasound imaging: An in vitro study. In *Engineering in Medicine and Biology Society (EMBC), 2015 37th Annual International Conference of the IEEE*, pages 2571–2575. IEEE, 2015. [Cited on page 44.]

[CPS+16] Zhiqiang Cui, Longsheng Pan, Huifang Song, Xin Xu, Bainan Xu, Xinguang Yu, and Zhipei Ling. Intraoperative mri for optimizing electrode placement for deep brain stimulation of the subthalamic nucleus in parkinson disease. *Journal of neurosurgery*, 124(1):62–69, 2016. [Cited on page 16.]

[CTB+11] David B Conley, Bruce Tan, Bernard R Bendok, H Hunt Batjer, Rakesh Chandra, Douglas Sidle, Rudy J Rahme, Joseph G Adel, and Andrew J Fishman. Comparison of intraoperative portable ct scanners in skull base and endoscopic sinus surgery: single center case series. *Skull Base*, 21(4):261, 2011. [Cited on pages 13 and 16.]

[CTRG05] Christian Chaussy, Stefan Thüroff, Xavier Rebillard, and Albert Gelet. Technology insight: high-intensity focused ultrasound for urologic cancers. *Nature clinical practice urology*, 2(4):191–198, 2005. [Cited on page 28.]

[CTT+12] Luca Alessandro Carbonaro, Penampai Tannaphai, Rubina Manuela Trimboli, Nicola Verardi, Maria Paola Fedeli, and Francesco Sardanelli. Contrast enhanced breast mri: spatial displacement from prone to supine patient's position. preliminary results. *European journal of radiology*, 81(6):e771–e774, 2012. [Cited on page 32.]

[CV11] Varun Chandola and Ranga Raju Vatsavai. A gaussian process based online change detection algorithm for monitoring periodic time series. In *Proceedings of the 2011 SIAM International Conference on Data Mining*, pages 95–106. SIAM, 2011. [Cited on page 54.]

[CZX+15] Chong-Qing Cheng, Rui-Tao Zhang, Yu Xiong, Li Chen, Jian Wang, Guo-Hua Huang, Ke-Quan Li, Lian Zhang, and Jin Bai. Contrast-enhanced ultrasound for evaluation of high-intensity focused ultrasound treatment of benign uterine diseases: retrospective analysis of contrast safety. *Medicine*, 94(16), 2015. [Cited on page 63.]

[DCS+17] Alessandro Diodato, Andrea Cafarelli, Andrea Schiappacasse, Selene Tognarelli, Gastone C Ciuti, and Arianna Menciassi. Motion compensation with skin contact control for high intensity focused ultrasound surgery in moving organs. *Physics in medicine and biology*, 2017. [Cited on pages 5, 28, 35, 43, 46, 58, 59, 60, and 62.]

[DJK+15] David L Diehl, Amitpal S Johal, Harshit S Khara, Stavros N Stavropoulos, Mohammed Al-Haddad, Jayapal Ramesh, Shyam Varadarajulu, Harry Aslanian, Stuart R Gordon, Frederick K Shieh, et al. Endoscopic ultrasound-guided liver biopsy: a multicenter experience. *Endoscopy international open*, 3(03):E210–E215, 2015. [Cited on page 19.]

[DLBK+15] V De Luca, T Benz, S Kondo, L König, D Lübke, S Rothlübbers, O Somphone, S Allaire, MA Lediju Bell, DYF Chung, et al. The 2014 liver ultrasound tracking benchmark. *Physics in medicine and biology*, 60(14):5571, 2015. [Cited on pages 11, 43, and 64.]

[DMS09] F Dube, A Mahadevan, and TA Sheldon. Fusion of ct and 3d ultrasound (3dus) for prostate delineation of patients with metallic hip prostheses (mhp). *International Journal of Radiation Oncology• Biology• Physics*, 75(3):S327–S328, 2009. [Cited on page 24.]

[DNMDM+10] Dante De Nigris, Laurence Mercier, Rolando Del Maestro, D Louis Collins, and Tal Arbel. Hierarchical multimodal image registration based on adaptive local mutual information. In *International Conference on Medical Image Computing and Computer-Assisted Intervention*, pages 643–651. Springer, 2010. [Cited on page 18.]

[DSB+10] Eric Delabrousse, Rares Salomir, Alain Birer, Christian Paquet, François Mithieux, Jean-Yves Chapelon, François Cotton, and Cyril Lafon. Automatic temperature control for mr-guided interstitial ultrasound ablation in liver using a percutaneous applicator: Ex vivo and in vivo initial studies. *Magnetic resonance in medicine*, 63(3):667–679, 2010. [Cited on page 34.]

[DSC+17] Alessandro Diodato, Andrea Schiappacasse, Andrea Cafarelli, Selene Tognarelli, Gastone Ciuti, and Arianna Menciassi. Robotic-assisted platform for usgfus treatment of moving organs. In *10th Hamlyn Symposium on Medical Robotics*, 2017. [Cited on pages 5 and 28.]

[DSMM07] Baudouin Denis De Senneville, Charles Mougenot, and Chrit TW Moonen. Real-time adaptive methods for treatment of mobile organs by mri-controlled high-intensity focused ultrasound. *Magnetic Resonance in Medicine*, 57(2):319–330, 2007. [Cited on page 43.]

[Duf13] H Duffau. A new philosophy in surgery for diffuse low-grade glioma (dlgg): oncological and functional outcomes. *Neurochirurgie*, 59(1):2–8, 2013. [Cited on page 65.]

[EGEA16] Fatma El-Zahraa Ahmed El-Gamal, Mohammed Elmogy, and Ahmed Atwan. Current trends in medical image registration and fusion. *Egyptian Informatics Journal*, 17(1):99–124, 2016. [Cited on page 22.]

[ETC+12] Jan Egger, Junichi Tokuda, Laurent Chauvin, Bernd Freisleben, Christopher Nimsky, Tina Kapur, and William Wells. Integration of the openigtlink network protocol for image-guided therapy with the medical platform mevislab. *The international Journal of medical Robotics and Computer assisted Surgery*, 8(3):282–290, 2012. [Cited on page 38.]

[ETH15] Emad S Ebbini and Gail Ter Haar. Ultrasound-guided therapeutic focused ultrasound: current status and future directions. *International Journal of Hyperthermia*, 31(2):77–89, 2015. [Cited on page 30.]

[FDSJ01] OJ Fleig, Frédéric Devernay, J-M Scarabin, and Pierre Jannin. Surface reconstruction of the surgical field from stereoscopic microscope views in neurosurgery. In *International Congress Series*, volume 1230, pages 268–274. Elsevier, 2001. [Cited on pages 88 and 94.]

[FES+13] Jessica L Foley, Matt Eames, John Snell, Arik Hananel, Neal Kassell, and Jean-Francois Aubry. Image-guided focused ultrasound: state of the technology and the challenges that lie ahead. *Imaging in Medicine*, 5(4):357–370, 2013. [Cited on pages 28 and 29.]

[FGPZ16] Rudolf Fahlbusch, Alexandra Golby, Francesco Prada, and Gabriel Zada. Introduction: Utility of intraoperative imaging, 2016. [Cited on page 68.]

[FMJBF54] William J Fry, WH Mosberg Jr, JW Barnard, and FJ Fry. Production of focal destructive lesions in the central nervous system with ultrasound. *Journal of neurosurgery*, 11(5):471–478, 1954. [Cited on page 28.]

[FNN+11] Hiroyuki Fukuda, Kazushi Numata, Akito Nozaki, Masaaki Kondo, Manabu Morimoto, Katsuaki Tanaka, Ryu Ito, Masao Ohto, Yoshiharu Ishibashi, Noriyoshi Oshima, et al. Hyperecho in ultrasound images during high-intensity focused ultrasound ablation for hepatocellular carcinomas. *European journal of radiology*, 80(3):e571–e575, 2011. [Cited on page 32.]

[FPS+11] David S Finley, Frederic Pouliot, Brian Shuch, Arnold Chin, Alan Pantuck, Jean B Dekernion, and Arie S Belldegrun. Ultrasound-based combination therapy: potential in urologic cancer. *Expert review of anticancer therapy*, 11(1):107–113, 2011. [Cited on page 64.]

[FWMN14] Bernhard Fuerst, Wolfgang Wein, Markus Müller, and Nassir Navab. Automatic ultrasound–mri registration for neurosurgery using the 2d and 3d lc 2 metric. *Medical image analysis*, 18(8):1312–1319, 2014. [Cited on pages 22 and 25.]

[FZB09] Nicolas Foroglou, Amir Zamani, and Peter Black. Intra-operative mri (iop-mr) for brain tumour surgery. *British journal of neurosurgery*, 23(1):14–22, 2009. [Cited on page 14.]

[FZF+17] Ting-Yun Fang, Haichong K Zhang, Rodolfo Finocchi, Russell H Taylor, and Emad M Boctor. Force-assisted ultrasound imaging system through dual force sensing and admittance robot control. *International journal of computer assisted radiology and surgery*, 12(6):983–991, 2017. [Cited on page 47.]

[GCM+93] A Gelet, JY Chapelon, J Margonari, Y Theillere, F Gorry, D Cathignol, and E Blanc. Prostatic tissue destruction by high-intensity focused ultrasound: Experimentation on canine prostate1. *Journal of endourology*, 7(3):249–253, 1993. [Cited on page 44.]

[Ged00] WMW Gedroyc. Interventional magnetic resonance imaging. *BJU international*, 86(s1):174–180, 2000. [Cited on page 14.]

[GMF+09] Jasmine Grewal, Sunil Mankad, William K Freeman, Roger L Click, Rakesh M Suri, Martin D Abel, Jae K Oh, Patricia A Pellikka, Gillian C Nesbitt, Imran Syed, et al. Real-time three-dimensional transesophageal echocardiography in the intraoperative assessment of mitral valve disease. *Journal of the American Society of Echocardiography*, 22(1):34–41, 2009. [Cited on page 19.]

[Gol07] Lee W Goldman. Principles of ct and ct technology. *Journal of nuclear medicine technology*, 35(3):115–128, 2007. [Cited on page 12.]

[GRU10] Andreas Geiger, Martin Roser, and Raquel Urtasun. Efficient large-scale stereo matching. In *Asian Conference on Computer Vision (ACCV)*, 2010. [Cited on pages 95 and 96.]

[GTC+15] Vijay PB Grover, Joshua M Tognarelli, Mary ME Crossey, I Jane Cox, Simon D Taylor-Robinson, and Mark JW McPhail. Magnetic resonance imaging: principles and techniques: lessons for clinicians. *Journal of clinical and experimental hepatology*, 5(3):246–255, 2015. [Cited on pages 13 and 14.]

[GWJ+09] S Gwynne, L Wills, G Joseph, G John, J Staffurth, C Hurt, and S Mukherjee. Respiratory movement of upper abdominal organs and its effect on radiotherapy planning in pancreatic cancer1. *Clinical Oncology*, 21(9):713–719, 2009. [Cited on page 63.]

[GWW+17] Yi Hui Gao, Lei Wu, Rui Wang, Qian Guo, Yi Ni Chen, Bing Hu, and Li Xin Jiang. Contrast-enhanced ultrasound evaluation of pancreatic cancer xenografts in nude mice after irradiation with sub-threshold focused ultrasound for tumor ablation. *Oncotarget*, 8(23):37584, 2017. [Cited on page 63.]

[GZL+16] Diana Ghinda, Nan Zhang, Junfeng Lu, Cheng-Jun Yao, Shiwen Yuan, and Jin-Song Wu. Contribution of combined intraoperative electrophysiological investigation with 3-t intraoperative mri for awake cerebral glioma surgery: comprehensive review of the clinical implications and radiological outcomes. *Neurosurgical focus*, 40(3):E14, 2016. [Cited on page 67.]

[HAT+12] Yipeng Hu, Hashim Uddin Ahmed, Zeike Taylor, Clare Allen, Mark Emberton, David Hawkes, and Dean Barratt. Mr to ultrasound registration for image-guided prostate interventions. *Medical image analysis*, 16(3):687–703, 2012. [Cited on page 25.]

[HBHH01] Derek LG Hill, Philipp G Batchelor, Mark Holden, and David J Hawkes. Medical image registration. *Physics in medicine and biology*, 46(3):R1, 2001. [Cited on pages 22 and 23.]

[HDD+94] Hugues Hoppe, Tony DeRose, Tom Duchamp, Mark Halstead, Hubert Jin, John McDonald, Jean Schweitzer, and Werner Stuetzle. Piecewise smooth surface reconstruction. In *Proceedings of the 21st annual conference on Computer graphics and interactive techniques*, pages 295–302. ACM, 1994. [Cited on page 99.]

[HDDC+11] Antoine Hakime, Frederic Deschamps, Enio Garcia Marques De Carvalho, Christophe Teriitehau, Anne Auperin, and Thierry De Baere. Clinical evaluation of spatial accuracy of a fusion imaging technique combining previously acquired computed tomography and real-time ultrasound for imaging of liver metastases. *Cardiovascular and interventional radiology*, 34(2):338–344, 2011. [Cited on page 24.]

[HGHS98] Michael Hünerbein, Bijan M Ghadimi, Wolfgang Haensch, and Peter M Schlag. Transendoscopic ultrasound of esophageal and gastric cancer using miniaturized ultrasound catheter probes. *Gastrointestinal endoscopy*, 48(4):371–375, 1998. [Cited on page 18.]

[HGS+14] Andrew B Holbrook, Pejman Ghanouni, Juan M Santos, Charles Dumoulin, Yoav Medan, and Kim Butts Pauly. Respiration based steering for high intensity focused ultrasound liver ablation. *Magnetic resonance in medicine*, 71(2):797–806, 2014. [Cited on page 43.]

[HKT+16] Yi-Hsuan Hsiao, Shou-Jen Kuo, Horng-Der Tsai, Ming-Chih Chou, and Guang-Perng Yeh. Clinical application of high-intensity focused ultrasound in cancer therapy. *Journal of Cancer*, 7(3):225, 2016. [Cited on page 29.]

[HMW+92] M Peter Heilbrun, Paul McDonald, Clay Wiker, Spencer Koehler, and William Peters. Stereotactic localization and guidance using a machine vision technique. *Stereotactic and functional neurosurgery*, 58(1-4):94–98, 1992. [Cited on page 8.]

[Hor87] Berthold KP Horn. Closed-form solution of absolute orientation using unit quaternions. *JOSA A*, 4(4):629–642, 1987. [Cited on page 77.]

[HPS+11] Sebastian P Haen, Philippe L Pereira, Helmut R Salih, Hans-Georg Rammensee, and Cécile Gouttefangeas. More than just tumor destruction: immunomodulation by thermal ablation of cancer. *Clinical and Developmental Immunology*, 2011, 2011. [Cited on page 64.]

[Huy09] Du Q Huynh. Metrics for 3d rotations: Comparison and analysis. *Journal of Mathematical Imaging and Vision*, 35(2):155–164, 2009. [Cited on page 81.]

[HWB+11] Olivia O Huston, Robert E Watson, Matt A Bernstein, Kiaran P McGee, S Matt Stead, Debb A Gorman, Kendall H Lee, and John Huston III. Intraoperative magnetic resonance imaging findings during deep brain stimulation surgery. *Journal of neurosurgery*, 115(4):852–857, 2011. [Cited on page 16.]

[HZ17] Qinghua Huang and Zhaozheng Zeng. A review on real-time 3d ultrasound imaging technology. *BioMed research international*, 2017, 2017. [Cited on pages 17 and 18.]

[IKW+05] RO Illing, JE Kennedy, F Wu, GR Ter Haar, AS Protheroe, PJ Friend, FV Gleeson, DW Cranston, RR Phillips, and MR Middleton. The safety and feasibility of extracorporeal high-intensity focused ultrasound (hifu) for the treatment of liver and kidney tumours in a western population. *British journal of cancer*, 93(8):890, 2005. [Cited on pages 29, 31, and 61.]

[IMLB03] Mir A Imran, Glen W Mclaughlin, William D Lipps, and James M Brennan. Miniaturized ultrasound apparatus and method, May 27 2003. US Patent 6,569,102. [Cited on page 18.]

[JCJH11] Seung Eun Jung, Se Hyun Cho, Jin Hee Jang, and Joon-Yeol Han. High-intensity focused ultrasound ablation in hepatic and pancreatic cancer: complications. *Abdominal imaging*, 36(2):185–195, 2011. [Cited on page 42.]

[JD14] Alex Pappachen James and Belur V Dasarathy. Medical image fusion: A survey of the state of the art. *Information Fusion*, 19:4–19, 2014. [Cited on pages 21 and 22.]

[JFRP14] Songbai Ji, Xiaoyao Fan, David W Roberts, and Keith D Paulsen. Efficient stereo image geometrical reconstruction at arbitrary camera settings from a single calibration. In *International Conference on Medical Image Computing and Computer-Assisted Intervention*, pages 440–447. Springer, 2014. [Cited on pages 26, 88, and 92.]

[JJK+06] T-Y Jung, S Jung, I-Y Kim, S-J Park, S-S Kang, S-H Kim, and S-C Lim. Application of neuronavigation system to brain tumor surgery with clinical experience of 420 cases. *min-Minimally Invasive Neurosurgery*, 49(04):210–215, 2006. [Cited on page 66.]

[JSM+80] Skip Jacques, C Hunter Shelden, Gilbert D McCann, Donald B Freshwater, and Robert Rand. Computerized three-dimensional stereotaxic removal of small central nervous system lesions in patients. *Journal of neurosurgery*, 53(6):816–820, 1980. [Cited on page 7.]

[KEMJ+00] Andrew P King, Philip J Edwards, Calvin R Maurer Jr, DA de Cunha, Ronald P Gaston, M Clarkson, Derek LG Hill, David J Hawkes, Michael R Fenlon, Anthony J Strong, et al. Stereo augmented reality in the surgical microscope. *Presence: Teleoperators & Virtual Environments*, 9(4):360–368, 2000. [Cited on page 113.]

[Ken05] James E Kennedy. High-intensity focused ultrasound in the treatment of solid tumours. *Nature reviews cancer*, 5(4):321–327, 2005. [Cited on page 31.]

[KFS+14] Norihiro Koizumi, Takakazu Funamoto, Joonho Seo, Dongjung Lee, Hiroyuki Tsukihara, Akira Nomiya, Takashi Azuma, Kiyoshi Yoshinaka, Naohiko Sugita, Yukio Homma, et al. A novel robust template matching method to track and follow body targets for niuts. In *Robotics and Automation (ICRA), 2014 IEEE International Conference on*, pages 1929–1936. IEEE, 2014. [Cited on pages 43 and 44.]

[KFS+15] Norihiro Koizumi, Takakazu Funamoto, Joonho Seo, Hiroyuki Tsukihara, Hiroyuki Fukuda, Hideyo Miyazaki, Kiyoshi Yoshinaka, Takashi Azuma, Naohiko Sugita, Yukio Homma, et al. An extremely robust us based focal lesion servo system incorporating a servo recovery algorithm for a niuts. In *Intelligent Robots and Systems (IROS), 2015 IEEE/RSJ International Conference on*, pages 2625–2632. IEEE, 2015. [Cited on page 44.]

[KK16] Deepika Kumari and Kamaljit Kaur. A survey on stereo matching techniques for 3d vision in image processing. *Int. J. Eng. Manuf*, 4:40–49, 2016. [Cited on pages 93 and 94.]

[KKKH12] Jani Petri Antton Katisko, Mikko Tapio Kauppinen, John Pertti Koivukangas, and Esa Raimo Heikkinen. Stereotactic operations using the o-arm. *Stereotactic and functional neurosurgery*, 90(6):401–409, 2012. [Cited on page 13.]

[KMG+10] Siavash Khallaghi, Parvin Mousavi, Ren Hui Gong, Sean Gill, Jonathan Boisvert, Gabor Fichtinger, David Pichora, Dan Borschneck, and Purang Abolmaesumi. Registration of a statistical shape model of the lumbar spine to 3d ultrasound images. In *International Conference on Medical Image Computing and Computer-Assisted Intervention*, pages 68–75. Springer, 2010. [Cited on page 25.]

[KMM10] Zdenek Kalal, Krystian Mikolajczyk, and Jiri Matas. Forward-backward error: Automatic detection of tracking failures. In *Pattern recognition (ICPR), 2010 20th international conference on*, pages 2756–2759. IEEE, 2010. [Cited on page 50.]

[KMM12] Zdenek Kalal, Krystian Mikolajczyk, and Jiri Matas. Tracking-learning-detection. *IEEE transactions on pattern analysis and machine intelligence*, 34(7):1409–1422, 2012. [Cited on pages 49, 51, and 52.]

[KMP+14] Ankur N Kumar, Michael I Miga, Thomas S Pheiffer, Lola B Chambless, Reid C Thompson, and Benoit M Dawant. Automatic tracking of intraoperative brain surface displacements in brain tumor surgery. In *Engineering in Medicine and Biology Society (EMBC), 2014 36th Annual International Conference of the IEEE*, pages 1509–1512. IEEE, 2014. [Cited on pages 108 and 113.]

[KMP+15] Ankur N Kumar, Michael I Miga, Thomas S Pheiffer, Lola B Chambless, Reid C Thompson, and Benoit M Dawant. Persistent and automatic intraoperative 3d digitization of surfaces under dynamic magnifications of an operating microscope. *Medical image analysis*, 19(1):30–45, 2015. [Cited on pages 26, 88, 94, and 112.]

[KMQ+09] Max O Köhler, Charles Mougenot, Bruno Quesson, Julia Enholm, Brigitte Le Bail, Christophe Laurent, Chrit TW Moonen, and Gösta J Ehnholm. Volumetric hifu ablation under 3d guidance of rapid mri thermometry. *Medical physics*, 36(8):3521–3535, 2009. [Cited on page 34.]

[KRM+10] Andrew P King, Kawal S Rhode, Y Ma, Cheng Yao, Christian Jansen, Reza Razavi, and Graeme P Penney. Registering preprocedure volumetric images with intraprocedure 3-d ultrasound using an ultrasound imaging model. *IEEE Transactions on Medical Imaging*, 29(3):924–937, 2010. [Cited on page 25.]

[KSM+10] Stefan Klein, Marius Staring, Keelin Murphy, Max A Viergever, and Josien PW Pluim. Elastix: a toolbox for intensity-based medical image registration. *IEEE transactions on medical imaging*, 29(1):196–205, 2010. [Cited on page 23.]

[KTL+08] Tong San Koh, Choon Hua Thng, Puor Sherng Lee, Septian Hartono, Helmut Rumpel, Boon Cher Goh, and Sotirios Bisdas. Hepatic metastases: in vivo assessment of perfusion parameters at dynamic contrast-enhanced mr imaging with dual-input two-compartment tracer kinetics model. *Radiology*, 249(1):307–320, 2008. [Cited on page 42.]

[KtMS+11] Pieter L Kubben, Karlien J ter Meulen, Olaf EMG Schijns, Mariël P ter Laak-Poort, Jacobus J van Overbeeke, and Henk van Santbrink. Intraoperative mri-guided resection of glioblastoma multiforme: a systematic review. *The lancet oncology*, 12(11):1062–1070, 2011. [Cited on pages 14, 26, and 69.]

[KWS+14] Tatiana D Khokhlova, Yak-Nam Wang, Julianna C Simon, Bryan W Cunitz, Frank Starr, Marla Paun, Lawrence A Crum, Michael R Bailey, and Vera A Khokhlova. Ultrasound-guided tissue fractionation by high intensity focused ultrasound in an in vivo porcine liver model. *Proceedings of the National Academy of Sciences*, 111(22):8161–8166, 2014. [Cited on page 29.]

[KZW+12] Samuel Kadoury, Lyubomir Zagorchev, Bradford J Wood, Aradhana Venkatesan, Jürgen Weese, J Jago, and Jochen Kruecker. A model-based registration approach of preoperative mri with 3d ultrasound of the liver for interventional guidance procedures. In *Biomedical Imaging (ISBI), 2012 9th IEEE International Symposium on*, pages 952–955. IEEE, 2012. [Cited on page 25.]

[LCS+17] Tiantian Liu, Minxin Chen, Yu Song, Hongliang Li, and Benzhuo Lu. Quality improvement of surface triangular mesh using a modified laplacian smoothing approach avoiding intersection. *PloS one*, 12(9):e0184206, 2017. [Cited on page 99.]

[Lew95] John P Lewis. Fast normalized cross-correlation. In *Vision interface*, pages 120–123, 1995. [Cited on page 51.]

[LGR+06] Yuan Le, Kevin Glaser, Olivier Rouviere, Richard Ehman, and Joel P Felmlee. Feasibility of simultaneous temperature and tissue stiffness detection by mre. *Magnetic resonance in medicine*, 55(3):700–705, 2006. [Cited on page 33.]

[LHR+14] Andras Lasso, Tamas Heffter, Adam Rankin, Csaba Pinter, Tamas Ungi, and Gabor Fichtinger. Plus: open-source toolkit for ultrasound-guided intervention systems. *IEEE Transactions on Biomedical Engineering*, 61(10):2527–2537, 2014. [Cited on pages 37 and 48.]

[LKO+03] Frank Lindseth, Jon Harald Kaspersen, Steinar Ommedal, Thomas Langø, Jon Bang, Jørn Hokland, Geirmund Unsgaard, and Toril A Nagelhus Hemes. Multimodal image fusion in ultrasound-based neuronavigation: improving overview

and interpretation by integrating preoperative mri with intraoperative 3d ultrasound. *Computer Aided Surgery*, 8(2):49–69, 2003. [Cited on page 32.]

[LLC+11] C-C Lee, S-T Lee, C-N Chang, P-C Pai, Y-L Chen, T-C Hsieh, and C-C Chuang. Volumetric measurement for comparison of the accuracy between intraoperative ct and postoperative mr imaging in pituitary adenoma surgery. *American Journal of Neuroradiology*, 32(8):1539–1544, 2011. [Cited on page 68.]

[LMWP10] Cristian A Linte, John Moore, Chris Wedlake, and Terry M Peters. Evaluation of model-enhanced ultrasound-assisted interventional guidance in a cardiac phantom. *IEEE Transactions on Biomedical Engineering*, 57(9):2209–2218, 2010. [Cited on page 18.]

[LPH+09] Thomas Lange, Nils Papenberg, Stefan Heldmann, Jan Modersitzki, Bernd Fischer, Hans Lamecker, and Peter M Schlag. 3d ultrasound-ct registration of the liver using combined landmark-intensity information. *International journal of computer assisted radiology and surgery*, 4(1):79–88, 2009. [Cited on page 25.]

[LS80] Der-Tsai Lee and Bruce J Schachter. Two algorithms for constructing a delaunay triangulation. *International Journal of Computer & Information Sciences*, 9(3):219–242, 1980. [Cited on page 98.]

[LSC15] Matthew A Lewis, Robert M Staruch, and Rajiv Chopra. Thermometry and ablation monitoring with ultrasound. *International Journal of Hyperthermia*, 31(2):163–181, 2015. [Cited on page 33.]

[LTK16] John C Lindon, George E Tranter, and David Koppenaal. *Encyclopedia of spectroscopy and spectrometry*. Academic Press, 2016. [Cited on page 12.]

[LTR+06] D Lindner, C Trantakis, C Renner, S Arnold, A Schmitgen, J Schneider, and J Meixensberger. Application of intraoperative 3d ultrasound during navigated tumor resection. *Minimally Invasive Neurosurgery*, 49(04):197–202, 2006. [Cited on page 18.]

[LVSOMR02] Maria Lorenzo-Valdés, Gerardo I Sanchez-Ortiz, Raad Mohiaddin, and Daniel Rueckert. Atlas-based segmentation and tracking of 3d cardiac mr images using non-rigid registration. In *International Conference on Medical Image Computing and Computer-Assisted Intervention*, pages 642–650. Springer, 2002. [Cited on page 24.]

[LW13] Sheng Li and Pei-Hong Wu. Magnetic resonance image-guided versus ultrasound-guided high-intensity focused ultrasound in the treatment of breast cancer. *Chinese journal of cancer*, 32(8):441, 2013. [Cited on pages 31, 32, and 33.]

[LWVN05] Marloes Maria Johanna Letteboer, Peter WA Willems, Max A Viergever, and Wiro J Niessen. Brain shift estimation in image-guided neurosurgery using 3-d ultrasound. *IEEE Transactions on Biomedical Engineering*, 52(2):268–276, 2005. [Cited on page 18.]

[LZCM42] John G Lynn, Raymund L Zwemer, Arthur J Chick, and August E Miller. A new method for the generation and use of focused ultrasound in experimental biology. *The Journal of general physiology*, 26(2):179, 1942. [Cited on page 28.]

[MA13] VRS Mani and S Arivazhagan. Survey of medical image registration. *Journal of Biomedical Engineering and Technology*, 1(2):8–25, 2013. [Cited on pages 22 and 23.]

[MB88] Frederick B Murphy and Michael E Bernardino. Interventional computed tomography. *Current problems in diagnostic radiology*, 17(4):125–154, 1988. [Cited on page 12.]

[MB05] Matthew Mellor and Michael Brady. Phase mutual information as a similarity measure for registration. *Medical image analysis*, 9(4):330–343, 2005. [Cited on page 25.]

[McD05] N McDannold. Quantitative mri-based temperature mapping based on the proton resonant frequency shift: review of validation studies. *International Journal of Hyperthermia*, 21(6):533–546, 2005. [Cited on page 32.]

[MCE+11] Mina Makary, E Antonio Chiocca, Natali Erminy, María Antor, Sergio D Bergese, Mahmoud Abdel-Rasoul, Soledad Fernandez, and Roger Dzwonczyk. Clinical and economic outcomes of low-field intraoperative mri-guided tumor resection neurosurgery. *Journal of Magnetic Resonance Imaging*, 34(5):1022–1030, 2011. [Cited on page 67.]

[MFH+12] Laurence Mercier, Vladimir Fonov, Claire Haegelen, Rolando F Del Maestro, Kevin Petrecca, and D Louis Collins. Comparing two approaches to rigid registration of three-dimensional ultrasound and magnetic resonance images for neurosurgery. *International journal of computer assisted radiology and surgery*, 7(1):125–136, 2012. [Cited on page 25.]

[MGE10] Yogesh K Mariappan, Kevin J Glaser, and Richard L Ehman. Magnetic resonance elastography: a review. *Clinical anatomy*, 23(5):497–511, 2010. [Cited on page 33.]

[MJB13] Uli Mezger, Claudia Jendrewski, and Michael Bartels. Navigation in surgery. *Langenbeck's archives of surgery*, 398(4):501–514, 2013. [Cited on pages 6, 10, 65, and 67.]

[MJM+09] Ernst Martin, Daniel Jeanmonod, Anne Morel, Eyal Zadicario, and Beat Werner. High-intensity focused ultrasound for noninvasive functional neurosurgery. *Annals of neurology*, 66(6):858–861, 2009. [Cited on page 29.]

[ML09] Marius Muja and David G. Lowe. Fast approximate nearest neighbors with automatic algorithm configuration. In *International Conference on Computer Vision Theory and Application VISSAPP'09)*, pages 331–340. INSTICC Press, 2009. [Cited on page 81.]

[MMH+14] Andrea Müns, Constanze Mühl, Robert Haase, Hendrik Möckel, Claire Chalopin, Jürgen Meixensberger, and Dirk Lindner. A neurosurgical phantom-based training system with ultrasound simulation. *Acta neurochirurgica*, 156(6):1237–1243, 2014. [Cited on pages 71 and 112.]

[Moi14] Aliasgar V Moiyadi. Objective assessment of intraoperative ultrasound in brain tumors. *Acta neurochirurgica*, 156(4):703, 2014. [Cited on page 68.]

[MPA+13] A Muller, Lorena Petrusca, Vincent Auboiroux, PJ Valette, R Salomir, and F Cotton. Management of respiratory motion in extracorporeal high-intensity focused ultrasound treatment in upper abdominal organs: current status and perspectives. *Cardiovascular and interventional radiology*, 36(6):1464–1476, 2013. [Cited on page 42.]

[MTLP12] Primoz Markelj, Dejan Tomaževič, Bostjan Likar, and Franjo Pernuš. A review of 3d/2d registration methods for image-guided interventions. *Medical image analysis*, 16(3):642–661, 2012. [Cited on page 22.]

[Mur04] Martin J Murphy. Tracking moving organs in real time. In *Seminars in radiation oncology*, volume 14, pages 91–100. Elsevier, 2004. [Cited on page 42.]

[MV98] JB Antoine Maintz and Max A Viergever. A survey of medical image registration. *Medical image analysis*, 2(1):1–36, 1998. [Cited on pages 22 and 24.]

[MYN13] Leonard Marks, Shelena Young, and Shyam Natarajan. Mri–ultrasound fusion for guidance of targeted prostate biopsy. *Current opinion in urology*, 23(1):43, 2013. [Cited on pages 21, 24, and 25.]

[ND14] Daniel B Nissman and Brian M Dale. Magnetic resonance imaging principles and techniques. *Text-Atlas of Skeletal Age Determination: MRI of the Hand and Wrist in Children*, pages 149–154, 2014. [Cited on page 14.]

[Neb12] G. Nebehay. Robust object tracking based on Tracking-Learning-detection. Master's thesis, Faculty of Informatics, TU Vienna, 2012. [Cited on page 53.]

[NGF06] Christopher Nimsky, Oliver Ganslandt, and Rudolf Fahlbusch. Implementation of fiber tract navigation. *Operative Neurosurgery*, 58(suppl_4):ONS–292, 2006. [Cited on page 67.]

[NKT+02] Anuja Nair, Barry D Kuban, E Murat Tuzcu, Paul Schoenhagen, Steven E Nissen, and D Geoffrey Vince. Coronary plaque classification with intravascular ultrasound radiofrequency data analysis. *Circulation*, 106(17):2200–2206, 2002. [Cited on page 19.]

[NM14] Nayera Nahvi and Deep Mittal. Medical image fusion using discrete wavelet transform. *Int J Eng Res Appl*, 4:165–70, 2014. [Cited on page 21.]

[NNB11] J Alison Noble, Nassir Navab, and H Becher. Ultrasonic image analysis and image-guided interventions. *Interface focus*, 1(4):673–685, 2011. [Cited on pages 18, 25, and 69.]

[OCLF10] Mustafa Ozuysal, Michael Calonder, Vincent Lepetit, and Pascal Fua. Fast keypoint recognition using random ferns. *IEEE transactions on pattern analysis and machine intelligence*, 32(3):448–461, 2010. [Cited on page 51.]

[OCP+91] Jonathan Ophir, Ignacio Cespedes, Hm Ponnekanti, Youseph Yazdi, and Xin Li. Elastography: a quantitative method for imaging the elasticity of biological tissues. *Ultrasonic imaging*, 13(2):111–134, 1991. [Cited on page 33.]

[OPS12] Joshua Owen, Quentin Pankhurst, and Eleanor Stride. Magnetic targeting and ultrasound mediated drug delivery: benefits, limitations and combination. *International Journal of Hyperthermia*, 28(4):362–373, 2012. [Cited on page 42.]

[OZG+16] Jill L Ostrem, Nathan Ziman, Nicholas B Galifianakis, Philip A Starr, Marta San Luciano, Maya Katz, Caroline A Racine, Alastair J Martin, Leslie C Markun, and Paul S Larson. Clinical outcomes using clearpoint interventional mri for deep brain stimulation lead placement in parkinson's disease. *Journal of neurosurgery*, 124(4):908–916, 2016. [Cited on page 14.]

[Pat98] J Kelly Patrick. Intraoperative brain shift and deformation: a quantitative analysis of cortical displacement in 28 cases. *Neurosurgery*, 43(4):759–759, 1998. [Cited on page 108.]

[PAV+15] Athanasios K Petridis, Maxim Anokhin, Jan Vavruska, Mehran Mahvash, and Martin Scholz. The value of intraoperative sonography in low grade glioma surgery. *Clinical neurology and neurosurgery*, 131:64–68, 2015. [Cited on pages 68 and 112.]

[PBH+04] Graeme P Penney, Jane M Blackall, MS Hamady, T Sabharwal, A Adam, and David J Hawkes. Registration of freehand 3d ultrasound and magnetic resonance liver images. *Medical image analysis*, 8(1):81–91, 2004. [Cited on page 25.]

[PC08] Terry Peters and Kevin Cleary. *Image-guided interventions: technology and applications*. Springer Science & Business Media, 2008. [Cited on page 21.]

[PCS+89] Charles A Pelizzari, George TY Chen, Danny R Spelbring, Ralph R Weichselbaum, and Chin-Tu Chen. Accurate three-dimensional registration of ct, pet, and/or mr images of the brain. *Journal of computer assisted tomography*, 13(1):20–26, 1989. [Cited on page 23.]

[PDBM+14] Francesco Prada, Massimiliano Del Bene, Luca Mattei, Cecilia Casali, Assunta Filippini, Federico Legnani, Antonella Mangraviti, Andrea Saladino, Alessandro Perin, Carla Richetta, et al. Fusion imaging for intra-operative ultrasound-based navigation in neurosurgery. *Journal of ultrasound*, 17(3):243–251, 2014. [Cited on page 68.]

[PDBM+15] F Prada, M Del Bene, L Mattei, L Lodigiani, S DeBeni, V Kolev, I Vetrano, L Solbiati, G Sakas, and F DiMeco. Preoperative magnetic resonance and intraoperative ultrasound fusion imaging for real-time neuronavigation in brain tumor surgery. *Ultraschall in der Medizin-European Journal of Ultrasound*, 36(02):174–186, 2015. [Cited on page 68.]

[PDBS+15] Francesco Prada, Massimiliano Del Bene, Marco Saini, Paolo Ferroli, and Francesco DiMeco. Intraoperative cerebral angiosonography with ultrasound contrast agents: how i do it. *Acta neurochirurgica*, 157(6):1025–1029, 2015. [Cited on page 69.]

[PFJ05] Perrine Paul, Oliver Fleig, and Pierre Jannin. Augmented virtuality based on stereoscopic reconstruction in multimodal image-guided neurosurgery: Methods and performance evaluation. *IEEE transactions on medical imaging*, 24(11):1500–1511, 2005. [Cited on pages 25, 26, 87, 88, and 112.]

[PMDB+14] Francesco Prada, Luca Mattei, Massimiliano Del Bene, Luca Aiani, Marco Saini, Cecilia Casali, Assunta Filippini, Federico Giuseppe Legnani, Alessandro Perin, Andrea Saladino, et al. Intraoperative cerebral glioma characterization with contrast enhanced ultrasound. *BioMed research international*, 2014, 2014. [Cited on page 69.]

[PMJ09] Perrine Paul, Xavier Morandi, and Pierre Jannin. A surface registration method for quantification of intraoperative brain deformations in image-guided neurosurgery. *IEEE Transactions on Information Technology in Biomedicine*, 13(6):976–983, 2009. [Cited on page 113.]

[PPM+14] Francesco Prada, Alessandro Perin, Alberto Martegani, Luca Aiani, Luigi Solbiati, Massimo Lamperti, Cecilia Casali, Federico Legnani, Luca Mattei, Andrea Saladino, et al. Intraoperative contrast-enhanced ultrasound for brain tumor surgery. *Neurosurgery*, 74(5):542–552, 2014. [Cited on page 68.]

[PPM+17] Alessandro Perin, Francesco Ugo Prada, Michela Moraldo, Andrea Schiappacasse, Tommaso Francesco Galbiati, Enrico Gambatesa, Piergiorgio d'Orio, Nicole Irene Riker, Curzio Basso, Matteo Santoro, et al. Usim: A new device and app for case-specific, intraoperative ultrasound simulation and rehearsal in neurosurgery. a preliminary study. *Operative Neurosurgery*, 2017. [Cited on pages 5, 65, 71, 72, 79, 83, and 86.]

[PRS+01] Brian C Porter, Deborah J Rubens, John G Strang, Jason Smith, Saara Totterman, and Kevin J Parker. Three-dimensional registration and fusion of ultrasound and mri using major vessels as fiducial markers. *IEEE Transactions on Medical Imaging*, 20(4):354–359, 2001. [Cited on page 25.]

[PSK16] I Jonathan Pomeraniec, Robert Spekman, and Neal Kassell. Focused ultrasound and metrics of diffusion of disruptive medical innovation. *BMJ Innovations*, pages bmjinnov–2015, 2016. [Cited on page 30.]

[PVF+14] Francesco Prada, Ignazio G Vetrano, Assunta Filippini, Massimiliano Del Bene, Alessandro Perin, Cecilia Casali, Federico Legnani, Marco Saini, and Francesco DiMeco. Intraoperative ultrasound in spinal tumor surgery. *Journal of ultrasound*, 17(3):195–202, 2014. [Cited on pages 26, 68, and 112.]

[PVG+11] Fabian Pedregosa, Gaël Varoquaux, Alexandre Gramfort, Vincent Michel, Bertrand Thirion, Olivier Grisel, Mathieu Blondel, Peter Prettenhofer, Ron Weiss, Vincent Dubourg, et al. Scikit-learn: Machine learning in python. *Journal of Machine Learning Research*, 12(Oct):2825–2830, 2011. [Cited on page 54.]

[PWKT00] Theophilos S Paleologos, John P Wadley, Neil D Kitchen, and David GT Thomas. Clinical utility and cost-effectiveness of interactive image-guided craniotomy: clinical comparison between conventional and image-guided meningioma surgery. *Neurosurgery*, 47(1):40–48, 2000. [Cited on page 66.]

[QCG+09] Morgan Quigley, Ken Conley, Brian Gerkey, Josh Faust, Tully Foote, Jeremy Leibs, Rob Wheeler, and Andrew Y Ng. Ros: an open-source robot operating system. In *ICRA workshop on open source software*, page 5. Kobe, 2009. [Cited on page 36.]

[RBE+14] Constantin Roder, Sotirios Bisdas, Florian Heinrich Ebner, Jürgen Honegger, Thomas Nägele, Ulrike Ernemann, and M Tatagiba. Maximizing the extent of resection and survival benefit of patients in glioblastoma surgery: high-field imri

versus conventional and 5-ala-assisted surgery. *European Journal of Surgical Oncology (EJSO)*, 40(3):297–304, 2014. [Cited on page 67.]

[RC11] Radu Bogdan Rusu and Steve Cousins. 3d is here: Point cloud library (pcl). In *Robotics and automation (ICRA), 2011 IEEE International Conference on*, pages 1–4. IEEE, 2011. [Cited on page 98.]

[RDSC07] Ingerid Reinertsen, Maxime Descoteaux, Kaleem Siddiqi, and D Louis Collins. Validation of vessel-based registration for correction of brain shift. *Medical image analysis*, 11(4):374–388, 2007. [Cited on pages 18 and 25.]

[RGW11] Petter Risholm, Alexandra J Golby, and William Wells. Multimodal image registration for preoperative planning and image-guided neurosurgical procedures. *Neurosurgery Clinics*, 22(2):197–206, 2011. [Cited on pages 68 and 87.]

[RHI+06] William W Roberts, Timothy L Hall, Kimberly Ives, J Stuart Wolf, J Brian Fowlkes, and Charles A Cain. Pulsed cavitational ultrasound: a noninvasive technology for controlled tissue ablation (histotripsy) in the rabbit kidney. *The Journal of urology*, 175(2):734–738, 2006. [Cited on page 29.]

[RLP+10] Robert W Ritchie, Tom Leslie, Rachel Phillips, Feng Wu, Rowland Illing, Gail Ter Haar, Andrew Protheroe, and David Cranston. Extracorporeal high intensity focused ultrasound for renal tumours: a 3-year follow-up. *BJU international*, 106(7):1004–1009, 2010. [Cited on page 42.]

[RLR+07] I-A Rasmussen, F Lindseth, OM Rygh, EM Berntsen, T Selbekk, J Xu, TA Nagelhus Hernes, E Harg, A Håberg, and G Unsgaard. Functional neuronavigation combined with intra-operative 3d ultrasound: initial experiences during surgical resections close to eloquent brain areas and future directions in automatic brain shift compensation of preoperative data. *Acta neurochirurgica*, 149(4):365–378, 2007. [Cited on page 11.]

[RMB+08] Radu Bogdan Rusu, Zoltan Csaba Marton, Nico Blodow, Mihai Dolha, and Michael Beetz. Towards 3d point cloud based object maps for household environments. *Robotics and Autonomous Systems*, 56(11):927–941, 2008. [Cited on page 98.]

[ROC+99] Nicola Ritter, Robyn Owens, James Cooper, Robert H Eikelboom, and Paul P Van Saarloos. Registration of stereo and temporal images of the retina. *IEEE Transactions on medical imaging*, 18(5):404–418, 1999. [Cited on page 23.]

[ROE+13] Stephen Roberts, Michael Osborne, Mark Ebden, Steven Reece, Neale Gibson, and Suzanne Aigrain. Gaussian processes for time-series modelling. *Phil. Trans. R. Soc. A*, 371(1984):20110550, 2013. [Cited on page 53.]

[RPBJH+11] Jon Ramm-Pettersen, Jon Berg-Johnsen, Per Kristian Hol, Sumit Roy, Jens Bollerslev, Thomas Schreiner, and Eirik Helseth. Intra-operative mri facilitates tumour resection during trans-sphenoidal surgery for pituitary adenomas. *Acta neurochirurgica*, 153(7):1367, 2011. [Cited on page 15.]

[RS10] Daniel Rueckert and Julia A Schnabel. Medical image registration. In *Biomedical Image Processing*, pages 131–154. Springer, 2010. [Cited on page 23.]

[RSH+86] David W Roberts, John W Strohbehn, John F Hatch, William Murray, and Hans Kettenberger. A frameless stereotaxic integration of computerized tomographic imaging and the operating microscope. *Journal of neurosurgery*, 65(4):545–549, 1986. [Cited on page 7.]

[RW06] Carl Edward Rasmussen and Christopher KI Williams. *Gaussian processes for machine learning*, volume 1. MIT press Cambridge, 2006. [Cited on page 54.]

[RWAS+00] William S Rainer Wirtz, Friedrich K Albert, Martin Schwaderer, Carsten Heuer, Andreas Staubert, Volker M Tronnier, Michael Knauth, and Stefan Kunze. The benefit of neuronavigation for neurosurgery analyzed by its impact on glioblastoma surgery. *Neurological research*, 22(4):354–360, 2000. [Cited on page 65.]

[SBD+13] David Schlesinger, Stanley Benedict, Chris Diederich, Wladyslaw Gedroyc, Alexander Klibanov, and James Larner. Mr-guided focused ultrasound surgery, present and future. *Medical physics*, 40(8), 2013. [Cited on page 30.]

[SBI+13] H Tutkun Sen, Muyinatu A Lediju Bell, Iulian Iordachita, John Wong, and Peter Kazanzides. A cooperatively controlled robot for ultrasound monitoring of radiation therapy. In *Intelligent Robots and Systems (IROS), 2013 IEEE/RSJ International Conference on*, pages 3071–3076. IEEE, 2013. [Cited on page 47.]

[SCC+04] Ralf Seip, Roy F Carlson, Wohsing Chen, Narendra T Sanghvi, and KA Dines. Automated hifu treatment planning and execution based on 3d modeling of the prostate, urethra, and rectal wall. In *Ultrasonics Symposium, 2004 IEEE*, volume 3, pages 1781–1784. IEEE, 2004. [Cited on page 34.]

[SFED11] Kai-Michael Scheufler, Joerg Franke, Anke Eckardt, and Hildegard Dohmen. Accuracy of image-guided pedicle screw placement using intraoperative computed tomography-based navigation with automated referencing, part i: cervicothoracic spine. *Neurosurgery*, 69(4):782–795, 2011. [Cited on page 68.]

[Sil16] Ronald H Silverman. Focused ultrasound in ophthalmology. *Clinical ophthalmology (Auckland, NZ)*, 10:1865, 2016. [Cited on page 29.]

[SKMS17] Joonho Seo, Norihiro Koizumi, Mamoru Mitsuishi, and Naohiko Sugita. Ultrasound image based visual servoing for moving target ablation by high intensity focused ultrasound. *The International Journal of Medical Robotics and Computer Assisted Surgery*, 13(4), 2017. [Cited on pages 44, 57, and 63.]

[SLM04] Will J Schroeder, Bill Lorensen, and Ken Martin. *The visualization toolkit: an object-oriented approach to 3D graphics*. Kitware, 2004. [Cited on pages 98 and 99.]

[SMS00] Martin Strowitzki, Jean Richard Moringlane, and Wolf-Ingo Steudel. Ultrasound-based navigation during intracranial burr hole procedures: experience in a series of 100 cases. *Surgical neurology*, 54(2):134–144, 2000. [Cited on pages 68 and 112.]

[SPLG05] CW Song, HJ Park, CK Lee, and R Griffin. Implications of increased tumor blood flow and oxygenation caused by mild temperature hyperthermia in tumor treatment. *International Journal of Hyperthermia*, 21(8):761–767, 2005. [Cited on page 64.]

[SPM84] I Suramo, M Päivänsalo, and V Myllylä. Cranio-caudal movements of the liver, pancreas and kidneys in respiration. *Acta radiologica. Diagnosis*, 25(2):129–131, 1984. [Cited on pages 57 and 63.]

[SRB+05] Christine Scholten, Raphael Rosenhek, Thomas Binder, Manfred Zehetgruber, Gerald Maurer, and Helmut Baumgartner. Hand-held miniaturized cardiac ultrasound instruments for rapid and effective bedside diagnosis and patient screening. *Journal of Evaluation in Clinical Practice*, 11(1):67–72, 2005. [Cited on page 18.]

[SRG+10] Cezary Szmigielski, Kashif Rajpoot, Vicente Grau, Saul G Myerson, Cameron Holloway, J Alison Noble, Richard Kerber, and Harald Becher. Real-time 3d fusion echocardiography. *JACC: Cardiovascular Imaging*, 3(7):682–690, 2010. [Cited on page 24.]

[SSA04] Achim Schweikard, Hiroya Shiomi, and John Adler. Respiration tracking in radiosurgery. *Medical physics*, 31(10):2738–2741, 2004. [Cited on page 34.]

[SSMN14] Andreas M Stark, Felix Schwartz, Maximilian Mehdorn, and Arya Nabavi. Neuroendoscopy and high-field intraoperative mri: first experience. *Journal of Neurological Surgery Part A: Central European Neurosurgery*, 75(05):371–375, 2014. [Cited on page 15.]

[SSP14] Jonathan N Sembrano, Edward Rainier G Santos, and David W Polly. New generation intraoperative three-dimensional imaging (o-arm) in 100 spine surgeries: does it change the surgical procedure? *Journal of Clinical Neuroscience*, 21(2):225–231, 2014. [Cited on page 13.]

[STdS+16] Bjorn Stemkens, Rob HN Tijssen, Baudouin Denis de Senneville, Jan JW Lagendijk, and Cornelis AT van den Berg. Image-driven, model-based 3d abdominal motion estimation for mr-guided radiotherapy. *Physics in medicine and biology*, 61(14):5335, 2016. [Cited on page 43.]

[STR+05] Jens P Schneider, Christos Trantakis, Matthias Rubach, Thomas Schulz, Juergen Dietrich, Dirk Winkler, Christof Renner, Ralf Schober, Kathrin Geiger, Oana Brosteanu, et al. Intraoperative mri to guide the resection of primary supratentorial glioblastoma multiforme—a quantitative radiological analysis. *Neuroradiology*, 47(7):489–500, 2005. [Cited on page 26.]

[SWM12] Chris Schulz, Stephan Waldeck, and Uwe Max Mauer. Intraoperative image guidance in neurosurgery: development, current indications, and future trends. *Radiology research and practice*, 2012, 2012. [Cited on pages 68 and 87.]

[TATH+14] Dasha Tyshlek, Jean-Francois Aubry, Gail Ter Haar, Arik Hananel, Jessica Foley, Matthew Eames, Neal Kassell, and Heather Huff Simonin. Focused ultrasound development and clinical adoption: 2013 update on the growth of the field. *Journal of therapeutic ultrasound*, 2(1):2, 2014. [Cited on page 29.]

[TBV+12] Emeline Tabouret, Maryline Barrié, Cecile Vicier, Anthony Gonçalves, Olivier Chinot, Patrice Viens, and Anne Madroszyk. Association of carcinoid tumor and low grade glioma. *World journal of surgical oncology*, 10(1):236, 2012. [Cited on page 14.]

[TCD+17] Selene Tognarelli, Gastone Ciuti, Alessandro Diodato, Andrea Cafarelli, and Arianna Menciassi. Robotic platform for high-intensity focused ultrasound surgery under ultrasound tracking: The futura platform. *Journal of Medical Robotics Research*, page 1740010, 2017. [Cited on page 34.]

[TFP+09] Junichi Tokuda, Gregory S Fischer, Xenophon Papademetris, Ziv Yaniv, Luis Ibanez, Patrick Cheng, Haiying Liu, Jack Blevins, Jumpei Arata, Alexandra J Golby, et al. Openigtlink: an open network protocol for image-guided therapy environment. *The International Journal of Medical Robotics and Computer Assisted Surgery*, 5(4):423–434, 2009. [Cited on page 38.]

[TGO11] Arun K Thittai, Belfor Galaz, and Jonathan Ophir. Visualization of hifu-induced lesion boundaries by axial-shear strain elastography: a feasibility study. *Ultrasound in medicine & biology*, 37(3):426–433, 2011. [Cited on page 33.]

[TMBN12] Tomasz Tykocki, Radosław Michalik, Wiesław Bonicki, and Paweł Nauman. Fluorescence-guided resection of primary and recurrent malignant gliomas with 5-aminolevulinic acid. preliminary results. *Neurologia i neurochirurgia polska*, 46(1):47–51, 2012. [Cited on page 65.]

[TMHJ11] Clare MC Tempany, Nathan J McDannold, Kullervo Hynynen, and Ferenc A Jolesz. Focused ultrasound surgery in oncology: overview and principles. *Radiology*, 259(1):39–56, 2011. [Cited on page 28.]

[TV98] Emanuele Trucco and Alessandro Verri. *Introductory techniques for 3-D computer vision*, volume 201. Prentice Hall Englewood Cliffs, 1998. [Cited on page 88.]

[Vap12] Jonathan Vappou. Magnetic resonance- and ultrasound imaging- based elasticity imaging methods: A review. *Critical Reviews$^{TM}$ in Biomedical Engineering*, 40(2), 2012. [Cited on page 33.]

[VLCY13] Valentina Vitiello, Su-Lin Lee, Thomas P Cundy, and Guang-Zhong Yang. Emerging robotic platforms for minimally invasive surgery. *IEEE reviews in biomedical engineering*, 6:111–126, 2013. [Cited on page 27.]

[VMK+16] Max A Viergever, JB Antoine Maintz, Stefan Klein, Keelin Murphy, Marius Staring, and Josien PW Pluim. A survey of medical image registration–under review. *Medical image analysis*, 33:140–144, 2016. [Cited on pages 22, 23, and 24.]

[VMM99] Jörg Vollmer, Robert Mencl, and Heinrich Mueller. Improved laplacian smoothing of noisy surface meshes. In *Computer graphics forum*, volume 18, pages 131–138. Wiley Online Library, 1999. [Cited on page 99.]

[VMMB07] Marie-Aude Vitrani, Hubert Mitterhofer, Guillaume Morel, and Nicolas Bonnet. Robust ultrasound-based visual servoing for beating heart intracardiac surgery. In *Robotics and Automation, 2007 IEEE International Conference on*, pages 3021–3027. IEEE, 2007. [Cited on page 18.]

[VMO05] M-A Vitrani, Guillaume Morel, and Tobias Ortmaier. Automatic guidance of a surgical instrument with ultrasound based visual servoing. In *Robotics and Automation, 2005. ICRA 2005. Proceedings of the 2005 IEEE International Conference on*, pages 508–513. IEEE, 2005. [Cited on page 34.]

[VS08] Edward Verbree and Hang Si. Validation and storage of polyhedra through constrained delaunay tetrahedralization. In *International Conference on Geographic Information Science*, pages 354–369. Springer, 2008. [Cited on page 98.]

[VSM+01] Shahram Vaezy, Xuegong Shi, Roy W Martin, Emil Chi, Peter I Nelson, Michael R Bailey, and Lawrence A Crum. Real-time visualization of high-intensity focused ultrasound treatment using ultrasound imaging. *Ultrasound in medicine & biology*, 27(1):33–42, 2001. [Cited on page 47.]

[WBK+08] Wolfgang Wein, Shelby Brunke, Ali Khamene, Matthew R Callstrom, and Nassir Navab. Automatic ct-ultrasound registration for diagnostic imaging and image-guided intervention. *Medical image analysis*, 12(5):577–585, 2008. [Cited on pages 24, 25, and 32.]

[Weh15] Martin Wehling. *Principles of translational science in medicine: from bench to bedside*. Academic Press, 2015. [Cited on page 12.]

[WFT+07] Thomas Wendler, Marco Feuerstein, Joerg Traub, Tobias Lasser, Jakob Vogel, Farhad Daghighian, Sibylle I Ziegler, and Nassir Navab. Real-time fusion of ultrasound and gamma probe for navigated localization of liver metastases. In *International Conference on Medical Image Computing and Computer-Assisted Intervention*, pages 252–260. Springer, 2007. [Cited on page 24.]

[WNB+00] Simon K Warfield, Arya Nabavi, Torsten Butz, Kemal Tuncali, Stuart G Silverman, Peter McL Black, Ferenc A Jolesz, and Ron Kikinis. Intraoperative segmentation and nonrigid registration for image guided therapy. In *International Conference on Medical Image Computing and Computer-Assisted Intervention*, pages 176–185. Springer, 2000. [Cited on page 11.]

[WR96] Christopher KI Williams and Carl Edward Rasmussen. Gaussian processes for regression. In *Advances in neural information processing systems*, pages 514–520, 1996. [Cited on page 53.]

[WR11] Catherine Westbrook and Carolyn Kaut Roth. *MRI in Practice*. John Wiley & Sons, 2011. [Cited on pages 13 and 14.]

[WSA+99] DB Williams, AV Sahai, L Aabakken, ID Penman, A Van Velse, J Webb, M Wilson, BJ Hoffman, and RH Hawes. Endoscopic ultrasound guided fine needle aspiration biopsy: a large single centre experience. *Gut*, 44(5):720–726, 1999. [Cited on page 19.]

[WSP+11] Andrew J Walker, Bret J Spier, Scott B Perlman, Jason R Stangl, Terrence J Frick, Deepak V Gopal, Mary J Lindstrom, Tracey L Weigel, and Patrick R Pfau. Integrated pet/ct fusion imaging and endoscopic ultrasound in the pre-operative staging and evaluation of esophageal cancer. *Molecular Imaging and Biology*, 13(1):166–171, 2011. [Cited on page 24.]

[WVA+96] William M Wells, Paul Viola, Hideki Atsumi, Shin Nakajima, and Ron Kikinis. Multi-modal volume registration by maximization of mutual information. *Medical image analysis*, 1(1):35–51, 1996. [Cited on page 23.]

[WWC+03] Feng Wu, Zhi-Biao Wang, Wen-Zhi Chen, Jin Bai, Hui Zhu, and Tian-yu Qiao. Preliminary experience using high intensity focused ultrasound for the treatment

of patients with advanced stage renal malignancy. *The Journal of urology*, 170(6):2237–2240, 2003. [Cited on page 31.]

[WWC+04] Feng Wu, Zhi-Biao Wang, Wen-Zhi Chen, Jian-Zhong Zou, Jin Bai, Hui Zhu, Ke-Quan Li, Fang-Lin Xie, Cheng-Bing Jin, Hai-Bing Su, et al. Extracorporeal focused ultrasound surgery for treatment of human solid carcinomas: early chinese clinical experience. *Ultrasound in medicine & biology*, 30(2):245–260, 2004. [Cited on page 31.]

[WWM+87] Eiju Watanabe, Takashi Watanabe, Shinya Manaka, Yoshiaki Mayanagi, and Kintomo Takakura. Three-dimensional digitizer (neuronavigator): new equipment for computed tomography-guided stereotaxic surgery. *Surgical neurology*, 27(6):543–547, 1987. [Cited on page 8.]

[YNA02] Xujiong Ye, J Alison Noble, and David Atkinson. 3-d freehand echocardiography for automatic left ventricle reconstruction and analysis based on multiple acoustic windows. *IEEE transactions on medical imaging*, 21(9):1051–1058, 2002. [Cited on page 24.]

[YVPH13] Shelten G Yuen, Nikolay V Vasilyev, J Pedro, and Robert D Howe. Robotic tissue tracking for beating heart mitral valve surgery. *Medical image analysis*, 17(8):1236–1242, 2013. [Cited on page 18.]

[YX08] Tinghe Yu and Chuanshan Xu. Hyperecho as the indicator of tissue necrosis during microbubble-assisted high intensity focused ultrasound: sensitivity, specificity and predictive value. *Ultrasound in medicine & biology*, 34(8):1343–1347, 2008. [Cited on page 32.]

[ZDLRB+16] Hasan A Zaidi, Kenneth De Los Reyes, Garni Barkhoudarian, Zachary N Litvack, Wenya Linda Bi, Jordina Rincon-Torroella, Srinivasan Mukundan Jr, Ian F Dunn, and Edward R Laws Jr. The utility of high-resolution intraoperative mri in endoscopic transsphenoidal surgery for pituitary macroadenomas: early experience in the advanced multimodality image guided operating suite. *Neurosurgical focus*, 40(3):E18, 2016. [Cited on page 16.]

[Zha00] Zhengyou Zhang. A flexible new technique for camera calibration. *IEEE Transactions on pattern analysis and machine intelligence*, 22(11):1330–1334, 2000. [Cited on pages 90 and 91.]

[ZMF17] Zhongshuai Zhang, Thomas Michaelis, and Jens Frahm. Towards mri temperature mapping in real time—the proton resonance frequency method with undersampled radial mri and nonlinear inverse reconstruction. *Quantitative imaging in medicine and surgery*, 7(2):251, 2017. [Cited on page 33.]

[ZNB07] Weiwei Zhang, J Alison Noble, and J Mike Brady. Adaptive non-rigid registration of real time 3d ultrasound to cardiovascular mr images. In *Biennial International Conference on Information Processing in Medical Imaging*, pages 50–61. Springer, 2007. [Cited on page 25.]

[ZW10] Lian Zhang and Zhi-Biao Wang. High-intensity focused ultrasound tumor ablation: review of ten years of clinical experience. *Frontiers of medicine in China*, 4(3):294–302, 2010. [Cited on page 31.]